Technische Universität München

Max-Planck-Institut für extraterrestrische Physik

Garching bei München

X-ray Emission Components
of the
Starburst Galaxy NGC 253

Michael Bauer

Vollständiger Abdruck der von der Fakultät für Physik der Technischen Universität München zur Erlangung des akademischen Grades eines

Doktors der Naturwissenschaften

genehmigten Dissertation.

Vorsitzender: Univ.-Prof. Dr. A. J. Buras
Prüfer: 1.   Hon.-Prof. Dr. G. Hasinger
     2.   Univ.-Prof. Dr. F. von Feilitzsch

Die Dissertation wurde am 13.12.2007 bei der Technischen Universität München eingereicht und durch die Fakultät für Physik am 17.01.2008 angenommen.

Die verschiedenen Komponenten der Röntgenstrahlung der Starburstgalaxie NGC 253

Die Starburstgalaxie NGC 253 wurde mit XMM-Newton im Röntgenlicht beobachtet. Die Analyse der wiederkehrenden ultraleuchtkräftigen Röntgenquelle NGC 253 ULX1 kann durch einen anisotropisch abstrahlenden massearmen Röntgendoppelstern mit einem schwarzen Loch erklärt werden. Die ausgedehnte Emission in NGC 253 kann durch heißes Gas (1.1–$9.2{\times}10^6$ K) beschrieben werden. Scheibenregionen, in denen Sterne entstehen, zeigen härtere Spektren als Regionen mit niedriger Sternentstehungsrate. Die Emission im Halo zeigt räumliche und spektrale Unterschiede. Erstmalig werden hochaufgelöste Röntgenspektren für verschiedene Regionen des Kernausflußes präsentiert und Temperaturen des hauptsächlich stoßionisierten Plasmas abgeleitet. Das O VIII-Emissionslinenbild der Kernregion zeigt zum ersten Mal direkt das heiße Windfluid.

X-ray Emission Components of the Starburst Galaxy NGC 253

Different emission components of the nearby starburst galaxy NGC 253 were studied in X-rays, based on four *XMM-Newton* observations between 2000 and 2003. We find the ultraluminous X-ray source NGC 253 ULX1 as a reccurent and anisotropically emitting stellar mass black hole low mass X-ray binary. Prominent emission from hot gas is characterised by temperatures of 1.1–$9.2{\times}10^6$ K in the disc and 1.1–$3.4{\times}10^6$ K in the halo. Regions in the disc that cover star forming regions, show harder spectra than regions with lower star forming activity. The halo emission is neither spatially nor spectrally uniform. We present the first spatially resolved high-resolution X-ray spectroscopy of the nuclear outflow and derive temperatures for the predominantly collisionally ionised plasma. The O VIII emission line image of the nuclear region for the first time shows the hot wind fluid directly.

Contents

Chapter 1

Introduction

Nearby galaxies provide excellent laboratories for studying many types of astrophysical phenomena, at a relatively well-known distance. Especially in galaxies with strong star forming activity (so-called starburst galaxies), the large scale diffuse emission can be quite prominent. One of the closest starburst galaxies, NGC 253, has been observed in X-rays many times. However, only the newest X-ray observatories provide the sensitivity and resolution to separate the diffuse emission from the point source population. In this work, we characterised the X-ray emission of NGC 253, as observed with the X-ray observatory *XMM-Newton*.

After an introduction of typical X-ray sources in starburst galaxies in this chapter, we describe the X-ray observatory *XMM-Newton*, the observations and the basic data reduction. In Chapter 3, we present our analysis of one selected point source, the recurrent ultra luminous X-ray source NGC 253 ULX1 (Bauer & Pietsch 2005). The diffuse emission in the disc and halo of NGC 253 is described in Chapter 4 (Bauer et al. 2007a), followed by the study of the nuclear outflow in Chapter 5 (Bauer et al. 2007b). The conclusions and an outlook into future work are summarised at the end.

1.1 X-ray emission from starburst galaxies

Starburst galaxies show an exceptionally high rate of star formation, compared to most galaxies. These bursts of star formation are often triggered in merging and interacting pairs of galaxies. In general, to start star formation, it is necessary to have a massive cloud of molecular gas. Once the mass exceeds the Jeans mass, the gravitational pressure exceeds the thermal pressure inside the cloud and it contracts and fragments. The further collapse of the fragments leads to the formation of stars. Massive stars that are formed in this process have a lifetime of just a few million years, before they have burned their nuclear fuel and explode as supernovae. Supernovae produce shock waves, which trigger more star formation, leading

1

to a chain reaction until the available fuel is used up, and the starburst stops. The typical time-scale for such a star formation event is about 10^7 yr (see e.g. King & Rowan-Robinson 2004).

In X-rays, starburst galaxies show a multitude of sources. In general, point-like sources in nearby galaxies are only observable with luminosities above 10^{33} erg s^{-1} in the Magellanic clouds (with a distance of $\sim$50 kpc). This limit increases for larger distances, and is $\sim 10^{36}$ erg s^{-1} for NGC 253. For fainter sources, the sensitivity of present X-ray telescopes is insufficient. Especially numerous among the resolved point sources in starburst galaxies are young sources, which result from the strong star formation. These are high mass X-ray binaries (HMXBs), supernova remnants (SNRs), and possibly ultraluminous X-ray sources (ULXs). Besides point-like sources, large scale diffuse emission can be quite prominent in starburst galaxies. In the following we will describe the different types of X-ray sources.

1.1.1 Discrete sources

1.1.1.1 X-ray binaries

X-ray binaries consist of either a white dwarf (these systems then are also called Cataclysmic Variables, CVs), a neutron star, or a black hole plus a companion star. When the compact object accretes material from the companion star, gravitational energy is transformed into heat and emitted in the form of electromagnetic radiation, which we then can observe in X-rays.

X-ray binaries are divided into two main classes, depending on the mass of the companion star:

Low mass X-ray binaries (LMXB) contain late type stars of type A or later, with a mass of less than 1 M$_\odot$. The companion star fills its Roche lobe, and mass is transferred through the inner Lagrangian point (Roche lobe overflow). Due to the conservation of angular momentum, the transferred gas spirals around the compact object and forms an accretion disc. Through instabilities in the disc, angular momentum is redistributed, causing the material to spiral inwards towards the compact object. LMXB have a typical lifetime of $\sim 10^{8-9}$ yr with luminosities $\lesssim 2 \times 10^{39}$ erg s^{-1} (Fabbiano 2006).

High mass X-ray binaries (HMXB) contain young O or B star with masses $\geq$ 10 M$_\odot$. HMXB are short-lived with a lifetime of $\sim 10^{6-7}$ yr (Fabbiano 2006) and show luminosities between $\sim 3 \times 10^{33}$ erg s^{-1} and 10^{40} erg s^{-1} (Shtykovskiy & Gilfanov 2005; Grimm et al. 2003). There are two main groups of HMXBs: supergiant and the Be/X-ray binaries. In the supergiant systems, the compact object accretes mass from a radially outflowing stellar

wind. Be/X-ray binaries accrete directly from a circumstellar disc surrounding the Be star. The orbit of the Be star and the compact object, presumably a neutron star, is generally wide and excentric. X-ray outbursts are normally associated with the passage of the neutron star through the circumstellar disc, where matter is accreted onto the compact object. As a result, the supergiant systems are persistent sources of X-rays, while Be/X-ray binaries are very variable.

1.1.1.2 Supersoft sources

Supersoft sources (SSS) are X-ray point sources which show very soft spectra (typically with blackbody temperatures of $kT < 100$ eV). They have luminosities in the range of 10^{36}–10^{39} erg s^{-1}. The favoured model (van den Heuvel et al. 1992) for these sources is that they are close binary system, with one of the components being a white dwarf (CVs). The soft X-ray emission is produced by nuclear burning of hydrogen accreted onto the white dwarf. Depending on the accretion rate, we either observe a steady nuclear burning on the white dwarf surface ($\dot{M} \sim 1 - 4 \times 10^{-7}$ M$_\odot$ yr^{-1}), or we observe an irregular burning ($\dot{M} < 10^{-8}$ M$_\odot$ yr^{-1}), which results in outbursts as seen in novae or cataclysmic variables.

Up to now, several SSS have been optically identified with close binary systems (Greiner 2000). Recently, Pietsch et al. (2005, 2006) reported 21 X-ray counterparts for optical novae in M31, where most of them were identified as supersoft sources. These findings support the model described above.

1.1.1.3 Ultra luminous X-ray sources

Ultra-luminous X-ray sources (ULXs) are extra-nuclear compact X-ray sources with luminosities considerably exceeding the Eddington luminosity for stellar mass X-ray binaries of $\sim 2 \times 10^{38}$ erg s^{-1} (Makishima et al. 2000). There are currently four preferred models to explain the luminosities of these objects. The first is that ULXs are intermediate mass black holes (IMBHs: M$_{\text{BH}} \sim 10^2 - 10^5M_\odot$). However, it is unclear how IMBHs are formed. The alternatives are stellar-mass black hole X-ray binaries where either photon bubble instabilities allow super-Eddington luminosities (Begelman 2002), anisotropically emitting X-ray binaries (King et al. 2001), or that ULXs are micro-quasars that are observed down the beam of their relativistic jet (e.g. Reynolds et al. 1997).

ULXs are preferentially found in star forming galaxies (e.g. Fabbiano et al. 2001; Roberts et al. 2002; Gao et al. 2003). If they are linked to ongoing star formation, they must be relatively short-lived. King (2004) pointed out that if these ULXs were all IMBHs then the amount of accretable gas would not suffice to fuel all these IMBHs to maintain X-ray luminosities above 10^{39} erg s^{-1}. Hence the majority of ULXs in star formation regions

cannot be powered by IMBHs.

Anisotropically emitting HMXBs are good candidates to explain the ULX population in star forming regions, since these sources are relatively short-lived. Further support for HMXBs comes from the optical identification of the stellar counterparts, which tend to match the characteristics of young massive stars that are able to fuel the ULXs (e.g. Roberts et al. 2001; Liu et al. 2004; Kuntz et al. 2005).

It is important to increase the sample of ULXs to find arguments that favour or exclude the above models. One attempt was the search for ULXs in 313 nearby galaxies from *ROSAT* HRI observations by Liu & Bregman (2005, hereafter LB2005). A target of this search was the starburst galaxy NGC 253 where they found 21 X-ray sources but only one of them matched their criteria for an ULX (NGC 253 ULX1). In Chapter 3, we report on a detailed analysis of NGC 253 ULX1 including *ROSAT*, *XMM-Newton* and *Chandra* data, and specifically on the detection of a second outburst in one of the *XMM-Newton* observations.

1.1.1.4 Supernovae

A supernova (SN) is a stellar explosion. Within a few days SNe can reach luminosities of 10^9 L$_\odot$, a considerable fraction of the total luminosity of a galaxy. In the explosion, a star is disrupted and most of its matter is ejected into the interstellar medium (ISM), enriching it with metals that were produced in the star's evolution or in the SN explosion.

According to spectral properties, SNe were classified into several types. SNe of type I do not show Balmer lines of hydrogen in their spectrum in contrast to SNe of type II. A further subdivision of type I SNe is based on the emission lines from Si II ($\lambda = 6150$ Å). SNe Ia show strong Si II lines, while they are absent in the spectra of SNe Ib and Ic.

The current understanding of this phenomenon differs from this classification. SNe II and Ib,c are linked to a young stellar population, while SNe Ia occur in older stellar populations.

SN II and Ib,c are the final stages in the evolution of massive (>8 M$_\odot$) stars. Inside these stars heavy elements are created by fusion. Once all the hydrogen fuel is used up, helium is burned to carbon and oxygen, which will then burn to even heavier elements like neon, magnesium, silicon, sulphur and finally to iron. Further fusion to heavier elements than iron is not possible, since iron has the highest binding energy per nucleon. Once the last fusion step in this chain has used up its fuel, no more energy can be produced and the pressure, counteracting gravity can no longer be maintained. The core of the star collapses, compressing the innermost region to a density of about three times the density of an atomic nucleus. At this point the so-called rebounce occurs, where a shockwave travels outwards, heating up the infalling material. The neutrinos that are produced in the collapse additionally power the explosion via neutrino heating and the neutrino-driven baryonic wind (Kitaura et al. 2006). In the centre a compact object remains (a neutron star or a black hole). The

typical energy output of this explosion is a few 10^{53} erg s^{-1}. The largest fraction (about 99%) is carried away by neutrinos, the ejected shell carries about 1%, and only $\sim$0.01% is converted into photons. The explosion also enriches the ISM with heavy elements, that were produced in the nuclear burning of the star.

SNe Ia are most likely the explosions of white dwarfs. These compact stars form the final evolutionary stages of less massive stars. White dwarfs are stabilised by the degenerate electron pressure up to the Chandrasekhar mass (1.44 M$_\odot$). Once the mass of a white dwarf exceeds about 1.3$_\odot$, for example by accretion in a binary system, carbon burning ignites in its interior. This will lead to the explosion of the star. The exact mechanism that leads to the runaway reaction is still unclear (e.g. Dursi & Timmes 2006). In contrast to core-collapse SNe (SN II and Ib,c) models predict that in SNe Ia the star is disrupted completely, and no compact object is left behind.

X-ray emission is expected from the following phases of a SN explosion (see e.g. Immler & Lewin 2003). There should be a short burst of high energy X-rays from core-collapse SNe in addition to a black-body continuum of $\sim$0.02 keV as a result of the high-temperature flash associated with the break out of the shock through the stellar surface. Weeks or months later, when the expanding ejecta have become optically thin to X-rays, high-energy X-rays may be detected, produced by compton scattering of monoenergetic gamma-rays from the radioactive decay ^{56}Ni$\rightarrow^{56}$Co$\rightarrow^{56}$Fe (e.g. Sunyaev et al. 1987; Itoh et al. 1987b). Additionally, X-rays may be observed when the ejecta plow into circumstellar matter supplied by the stellar wind in previous phases of mass loss of the progenitor (e.g. Itoh et al. 1987a). The circumstellar shock that is formed in this interaction can have a very high temperature ($T > 10^9$ K).

1.1.1.5 Supernova remnants

Supernova remnants (SNRs) form after a supernova has exploded. Ejected mass from the supernova explosion expands rapidly into the surrounding medium, with velocities of $5\,000 - 10\,000$ km s^{-1}. During the expansion of this shell, gas that has been expelled during the star's life, is swept up and shock-heated to 10^7–10^8 K. Most of the observed X-ray emission is thermal emission which is produced in the forward and reverse shocks, with typical luminosities of $L_X = 10^{35-37}$ erg s^{-1}. This results in a ring-like limb brightened appearance with several hot spots in the interaction regions. Additionally, we may observe synchrotron radiation from electrons that are accelerated in the magnetic fields. As the remnant cools on a time scale of about 10^6 years and disperses into the local medium, it decreases in brightness until it blends into the surrounding ISM. Typical sizes of SNRs are $\lesssim 100$ pc before they dissolve.

1.1.2 Diffuse emission

1.1.2.1 Disc emission

Diffuse X-ray emission can originate from hot gas that is radiatively cooling. It will show a thermal bremsstrahlung spectrum, superimposed with atomic line transitions. The origin of this gas are massive stars with strong stellar winds which enrich the surrounding medium with heavy elements. Also supernovae produce hot gas in their explosion, which enriches the interstellar medium (ISM). Combined, the stellar winds and the supernovae can create a bubble around them in the ISM that expands due to the higher pressure inside (Chevalier & Clegg 1985). On the surface of this expanding shell the material is shocked and heated up to temperatures of $\sim10^8$ K. Expansion of this bubble is preferred in the direction with the least resistance, which is perpendicular to the disc. At some point the bubble breaks out of the disc, and metal enriched, hot gas is fuelled into the halo of the galaxy, forming so called galactic fountains (Shapiro & Field 1976; Bregman 1980). Depending on the kinetic energy of the outflow, the gas can either escape the galactic potential well and escape into the intergalactic medium, or it can rain down again onto the disc.

Alternatively to the truly diffuse emission from a hot interstellar gas component in the disc, also the cumulative emission of an unresolved large population of weak stellar-type X-ray sources can appear as unresolved emission. This was first discovered in the Milky Way's ridge X-ray emission (e.g. Revnivtsev et al. 2006), where evidence was found that the bulk of the Galactic ridge X-ray emission is composed of weak X-ray sources, mostly cataclysmic variables and coronally active stars in binary systems, with a luminosity of most of these sources of less than 10^{31} erg s^{-1}. Also in other galaxies, Revnivtsev et al. (2007) found evidence that the apparently diffuse emission may partly be consistent with the emission from an old stellar population.

Therefore, caution is necessary in the interpretation of an apparently diffuse emission in a galactic disc, since it can be both due to a hot interstellar gas component and/or an unresolved old stellar population.

1.1.2.2 Superwinds

An extreme case of galactic outflows can be caused by a starburst nucleus. Here the star formation is more powerful than in the spiral arms, and the combined pressure of $\sim10^6$ supernovae and stellar winds may lead to a spectacular superwind (e.g. in M82, see Fig. 1.1 and Stevens et al. 2003). The gas in superwinds is seen to have velocities between 200 and 1000 km s^{-1} (Heckman et al. 2000). Hydrodynamical simulations by Strickland & Stevens (2000) showed that the superwind can contain gas in a wide range of densities and temperatures. The majority of the superwind volume is filled with hot metal-enriched gas

Figure 1.1: A multi colour image of the starburst galaxy M82. Perpendicular to the galactic disc (in green) a hot outflow extends into the galaxy's halo (red and blue). X-ray are represented in blue (*Chandra*), Optical light in green and orange (HST), and Infrared light in red (Spitzer). Credit: X-ray: NASA/CXC/JHU/D.Strickland; Optical: NASA/ESA/STScI/AURA/The Hubble Heritage Team; IR: NASA/JPL-Caltech/Univ. of AZ/C. Engelbracht

covering temperatures between $10^{6.5}$ and $10^{7.5}$ K. Velocities of this component can range up to $\sim$3000 km s^{-1} (Chevalier & Clegg 1985). A typical superwind may inject 10^8 M$_\odot$ of metals and 10^{58} erg s^{-1} into the intergalactic medium over its estimated lifetime of 10^7 yr (Heckman et al. 1990). The superwind may also sweep up clouds of cold gas from the galactic disc and transport them out into the halo. This gas may be shock-heated to several 10^6 K and become an additional source of thermal X-ray emission. Also thermal conduction or turbulent mixing between cool dense gas and surrounding hot regions can produce X-ray emission in the interface regions (Weaver et al. 1977). The superwind itself is thought to be too thin and too hot to be observed in X-rays directly (Strickland et al. 2000). In Chapter 5 we will show that this assumption may actually not be correct.
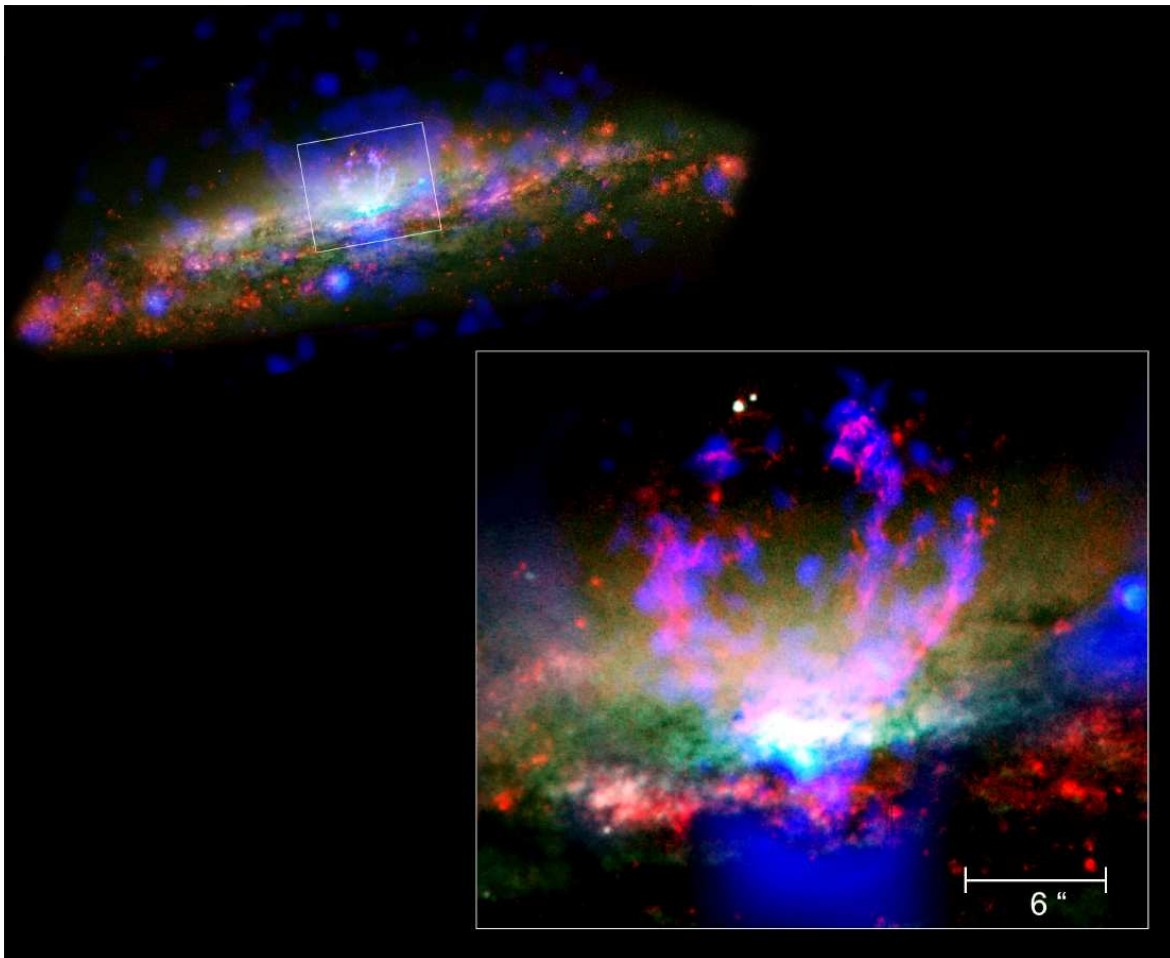
Figure 1.2: A multi colour image of the starburst galaxy NGC 3079. Material ejected from the starburst nucleus expands into the halo, enriching it with hot gas, metals and energy. X-rays are in blue (*Chandra*), and optical light in red and green (HST). Credit: NASA/CXC/STScI/U.North Carolina/G.Cecil

1.1.2.3   Halo emission

Starburst galaxies with a superwind also show spectacular halo emission in X-rays. Especially galaxies which we see edge-on, like NGC 253, M82, and NGC 3079 are suited for an analysis of the diffuse halo emission. In these cases the emission from the disc and the halo can be separated easily. An analysis of a sample of seven edge-on starburst galaxies with *ROSAT* and *ASCA* by Dahlem et al. (1998) showed that all galaxies of the sample have hot gas in their halos. Spectral fits to the *ROSAT* PSPC and *ASCA* spectra indicate the presence of two gas phases with temperatures of 0.2–0.4 keV and 0.65–0.9 keV with abundances between 10% and 40% solar. The origin of the X-ray emission in the halo can be shocked or mass-loaded superwind material, a volume filling halo medium that was swept up and shock

heated by the superwind, or halo clouds (either preexisting or dragged up from the disc) that interact with the wind.

1.1.3 Foreground and background sources in fields of galaxies

1.1.3.1 Stars

X-ray emission has been detected from many late-type, as well as from hot OB stars (see review by Schmitt 2000). Hence, X-ray observations of nearby galaxies also reveal a significant fraction of Galactic stars, seen as relatively soft X-ray sources homogeneously distributed across the field of view. With typical luminosities $L_X < 10^{31}$ erg s^{-1}, single stars in other galaxies are too faint to be detected with present instruments. Concentrations of stars can however be detected, but not resolved.

X-ray emission from late-type (spectral types F, G, K, and M) stars is interpreted as coronal activity, similar to that observed in the sun, but on a much larger scale in some stars. For example, many M-type stars show significant coronal activity and strong flares. In addition, the fraction of the observed X-ray emission in late-type stars is found to be correlated with the rotational period (Schmitt 2000). There is also a strong correlation between relatively strong X-ray and Hα emission, which is also an indicator of strong coronal activity (Fleming et al. 1989). According to the current understanding, the X-ray emission in the stellar coronae is produced by plasma heated by the interaction of the convective layers with magnetic fields in the star's outer convection zone (e.g. Haisch et al. 1991).

Relatively soft X-ray emission is also observed from hot stars (Harnden et al. 1979), which do not have an outer convection zone. It has been suggested that X-ray emission from hot OB stars is produced by heating due to hydrodynamic shocks caused by instabilities in strong stellar winds emerging from such stars (Feldmeier et al. 1997).

X-ray emission has been detected from A-type stars as well, although it is not clear which mechanism is responsible for producing it, since A-type stars do not have strong stellar winds. In some cases, X-ray emission from A stars is due to their late-type companions (e.g. Stelzer & Burwitz 2003).

1.1.3.2 Diffuse emission in the solar system

In the ROSAT all-sky survey data, Snowden et al. (1994) reported the existence of mysterious X-ray contamination episodes (long-term enhancements, LTEs). During these times the X-ray counting rate in the lower energy bands as much as doubled on a time scale of 1–2 days. However, they could not find any correlation with other observational parameters, such as the spacecraft position or look direction. New insight on LTEs was obtained from the
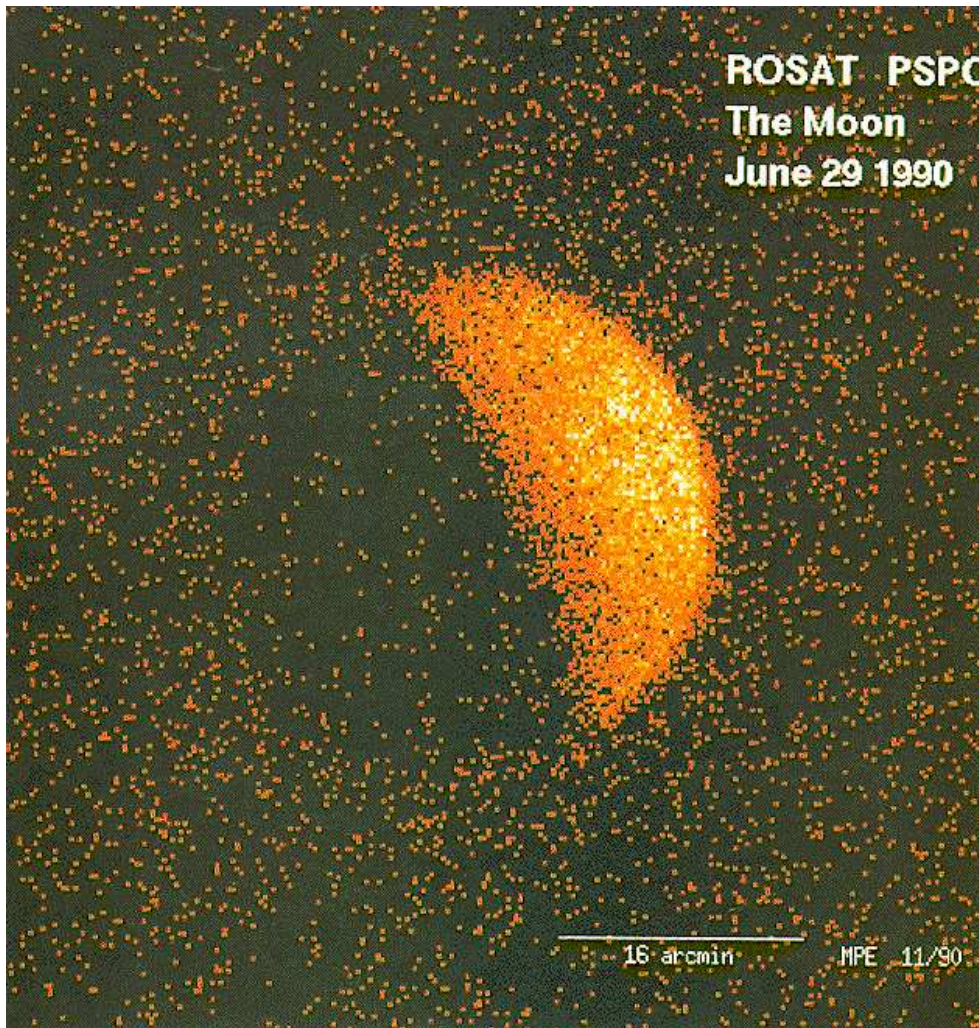
Figure 1.3: A soft X-ray image of the moon, obtained with *ROSAT*. From Schmitt et al. (1991).

discovery of X-ray emission of comet Hyakutake (Lisse et al. 1996) and many more comets (e.g. Dennerl et al. 1997; Cravens 2002). The emission mechanism is now well understood as being charge exchange of solar wind heavy ions with cometary neutrals (Cravens 1997; Bodewits et al. 2007). Then, Cox (1998) and Cravens (2000) suggested that solar wind charge exchange (SWCX) with neutrals in the geocorona and in the heliosphere accounts for a part of soft X-ray background below 1 keV (also see Fujimoto et al. 2007). Spectral information on geocoronal SWCX was first obtained during a Chandra dark moon observation (Wargelin et al. 2004, also see Fig. 1.3). The X-ray photons detected in the direction of the dark moon are most likely from this source. The emission spectrum could be described by a sum of C VI , O VII , and O VIII K lines, although the statistics and energy resolution were limited. More recently, Snowden et al. (2004) reported a time variation of the soft

X-ray intensity during the *XMM-Newton* Hubble deep field north observation. The enhancement was correlated with solar wind proton flux variations. They detected C VI , O VII , O VIII , Ne IX , and Mg XI emission lines in the enhancement and found this spectrum to be consistent with that expected from SWCX emission of the geocorona or helioshpere.

1.1.3.3   Diffuse emission in the Milky Way

Additional to the line emission from SWCX, we observe diffuse X-ray emission from hot ($\sim 10^6$ K) thin thermal plasma in the Milky Way. One component is contained within a hot bubble (Paresce 1984) in the disk of the Galaxy which surrounds the Sun (but was not created by the Sun) and extends from $\sim$50 pc to 200 pc in different directions (this region is known as the Local Hot Bubble, LHB). And second, there is an extensive distribution of this plasma in the halo of our Galaxy (Burrows & Mendenhall 1991; Snowden et al. 1991).

As can be seen in Fig. 1.4, the distribution of the diffuse X-ray emission on the sky is not homogeneous. In Appendix A, we present results from the analysis of two Suzaku observations at high galactic latitudes, where we tried to investigate the spatial distribution of the diffuse emission components.

1.1.3.4   Active Galactic Nuclei

A significant fraction of the X-ray sources detected in fields of nearby galaxies does not belong to the host galaxy, but has clear extragalactic origin. As shown by the recent deepest available surveys of the X-ray background, the majority of theses extragalactic sources belong to a class of active galactic nuclei (AGN, Mushotzky et al. 2000; Hasinger et al. 2001; Brandt & Hasinger 2005).

AGN are highly luminous sources, with their luminosities emanating from a small spatially unresolved galactic core, sometimes exceeding 10^{46} erg s^{-1}. This small emitting region is implied by the X-ray flux variability on time scales as short as several minutes (to years), observed in many AGN. Based on optical line widths (Osterbrock 1998) and absorption values, AGN are divided into two basic types: type-1 AGN (unabsorbed sources showing broad emission lines) and type-2 AGN (absorbed sources with narrow emission lines). According to the unification scheme proposed by Antonucci (1993), these two AGN types are intrinsically similar, with their observed differences being due to the different viewing directions. AGNs host supermassive black holes ($\sim 10^6 - 10^9$ M$_\odot$), in their cores which accrete galactic matter through an accretion disc. According to the standard AGN model, the disc is surrounded by an extensive dusty molecular torus and a corona populated by hot electrons. These corona electrons are believed to transfer energy via inverse compton scattering to UV photons emerging from the disc, producing the observed hard X-ray continuum in AGN.
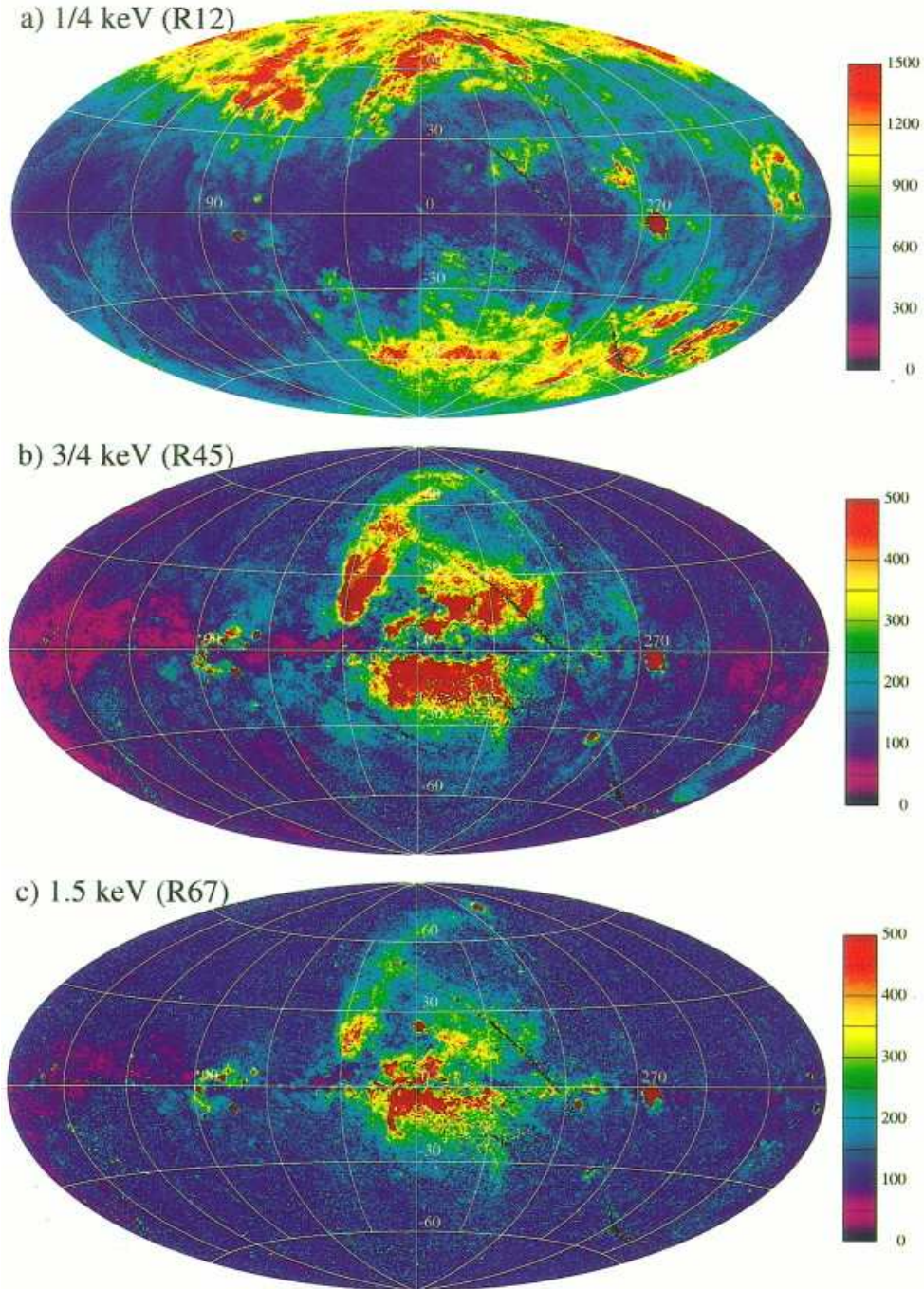
Figure 1.4: Maps of the *ROSAT* (a) R12, (b) R45, and (c) R67 band data after point sources have been removed. The projection is an Aitoff-Hammer equal area centred on the Galactic centre with Galactic longitude increasing to the left. The values next to the colour bars indicate the intensity and the units are 10^{-6} counts s^{-1} arcmin^{-2}. From Snowden et al. (1997).

AGN typically show a power law spectrum with a photon index between 1.5 and 2.0 (e.g. Mushotzky 1984). Additional spectral components like the Fe K$_\alpha$ line at $\sim$6.4–6.7 keV, soft excess, etc, are believed to be due to reflection and reprocessing of the power law emission in the optically thick accretion disc.

1.2 The starburst galaxy NGC 253

NGC 253 is a starburst galaxy in the Sculptor Group (an optical image is shown in Fig. 1.5). Its general properties are summarised in Table 1.2. The three properties that make NGC 253 special for the following analysis are the proximity (it is one of the closest starburst galaxies), the high inclination angle, which allows a clear separation of disc and halo emission, and the low foreground absorption, which enables us to observe NGC 253 almost unabsorbed also at low X-ray energies.

NGC 253 has been observed in X-rays many times. There are observations with *Einstein* (e.g. Fabbiano & Trinchieri 1984), *ROSAT* (e.g. Pietsch 1992; Read et al. 1997; Dahlem et al. 1998; Vogler & Pietsch 1999; Pietsch et al. 2000), *ASCA* (e.g. Ptak et al. 1997), *Beppo*SAX
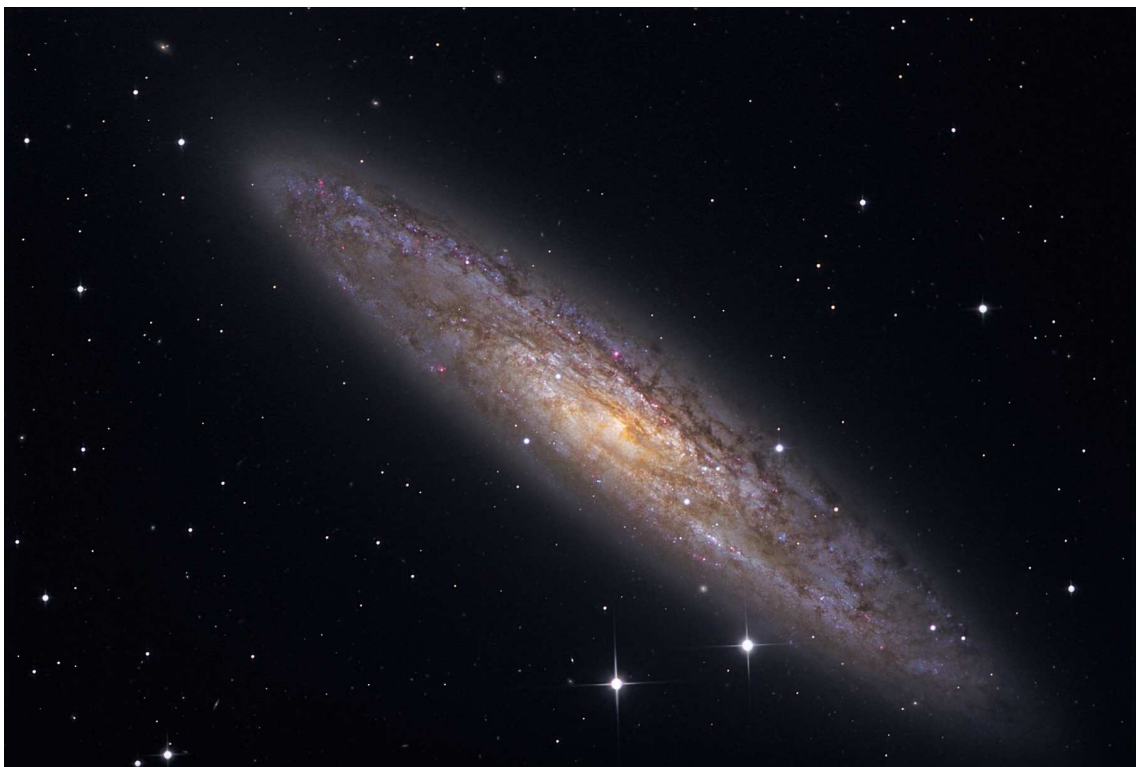
Figure 1.5: Optical image of NGC 253 showing the spiral arm structure in the disc (courtesy of www.cappella-observatory.com).

Table 1.1: Properties of NGC 253.

		Ref.
Type	Sc	Tully (1988)
Assumed distance	2.58 Mpc	Puche et al. (1991)
Systemic velocity	236 km s^{-1}	Pence (1981)
Position of centre	$\alpha_{2000} = 0^{\mathrm{h}}47^{\mathrm{m}}33\!\!.\!\!^{\mathrm{s}}3$,	Forbes et al. (2000)
	$\delta_{2000} = -25°17'18''$	
D_{25}	$25\!\!.\!\!'4$	Tully (1988)
Corrected D_{25}	$18\!\!.\!\!'8$	Tully (1988)
Axial ratio	0.23	Tully (1988)
Position angle	52°	de Vaucouleurs et al. (1991)
Inclination	78.5°	Pence (1980)
Galactic foreground N_{H}	1.3×10^{20} cm^{-2}	Dickey & Lockman (1990)

(e.g. Cappi et al. 1999), *XMM-Newton* (e.g. Pietsch et al. 2001), and *Chandra* (e.g. Weaver et al. 2002; Strickland et al. 2002, 2004a,b). The X-ray emission that we observe from NGC 253 is quite complex and shows a multitude of different components. While some instruments were not able to separate point sources from diffuse emission, other instruments, especially *ROSAT*, *XMM-Newton*, and *Chandra*, have a narrow enough point spread function to do so. In the following we will take a closer look at the individual emission components.

1.2.1   The nucleus

NGC 253 is at a relatively early stage in its starburst, at an age of about 20-30 million years (Engelbracht et al. 1998). So far, it is not clear what caused the starburst in the centre of this galaxy. Starbursts can be ignited by collisions between galaxies, but for NGC 253 no collision partner is known. From infrared observations, Rieke et al. (1988) find a supernova rate of $\sim$0.1 per year in the central 50 pc and a similar rate in the surrounding regions. A total mass of more than 10^8 M$_\odot$ is required for the starburst of this galaxy.

The interstellar medium in the nucleus is frequently enriched with energy and metals by the ejected material from supernovae and from hot stars via their stellar winds. In X-rays, the spectrum of this hot plasma shows many emission lines from N, O, Ne, Mg, Si, and Fe. Pietsch et al. (2001) were able to model the *XMM-Newton* EPIC spectrum of the nucleus with an absorbed three temperature plasma ($N_{\mathrm{H}} = 0.34, 1.78, 13.2 \times 10^{22}$ cm^{-2}, $kT = 0.56, 0.92, 6.3$ keV).

There have also been claims that NGC 253 hosts a weak AGN (e.g. Turner & Ho 1985; Mohan et al. 2002; Weaver et al. 2002). However, the signature of an AGN, a highly absorbed

non-thermal component was not required in the spectral fit by Pietsch et al. (2001). The issue whether NGC 253 does host an AGN is still under discussion.

1.2.2 The disc

The disc of NGC 253 shows a large population of point sources. Eight X-ray point sources were found by Fabbiano & Trinchieri (1984) with the *Einstein* observatory. Since then the number of detected point sources increased dramatically (e.g. Vogler & Pietsch 1999; Strickland et al. 2002; Trinchieri et al. in preparation) to several hundred sources. The sample detected with *ROSAT* and analysed by Vogler & Pietsch (1999) was explained mostly by X-ray binaries, supernovae, and supernova remnants. A detailed analysis of the source population as found with *XMM-Newton* and *Chandra* is ongoing (Trinchieri et al. in preparation).

Liu & Bregman (2005) reported a list of ULXs in 313 nearby galaxies from *ROSAT* HRI observations. One of these sources happens to be in NGC 253 and also showed up in one *XMM-Newton* observation. The analysis of NGC 253 ULX1 will be presented in Chapter 3.

Besides the point sources, Fabbiano & Trinchieri (1984) also detected diffuse emission in the disc. Pietsch et al. (2000) reported that this emission is absorbed and follows the spiral
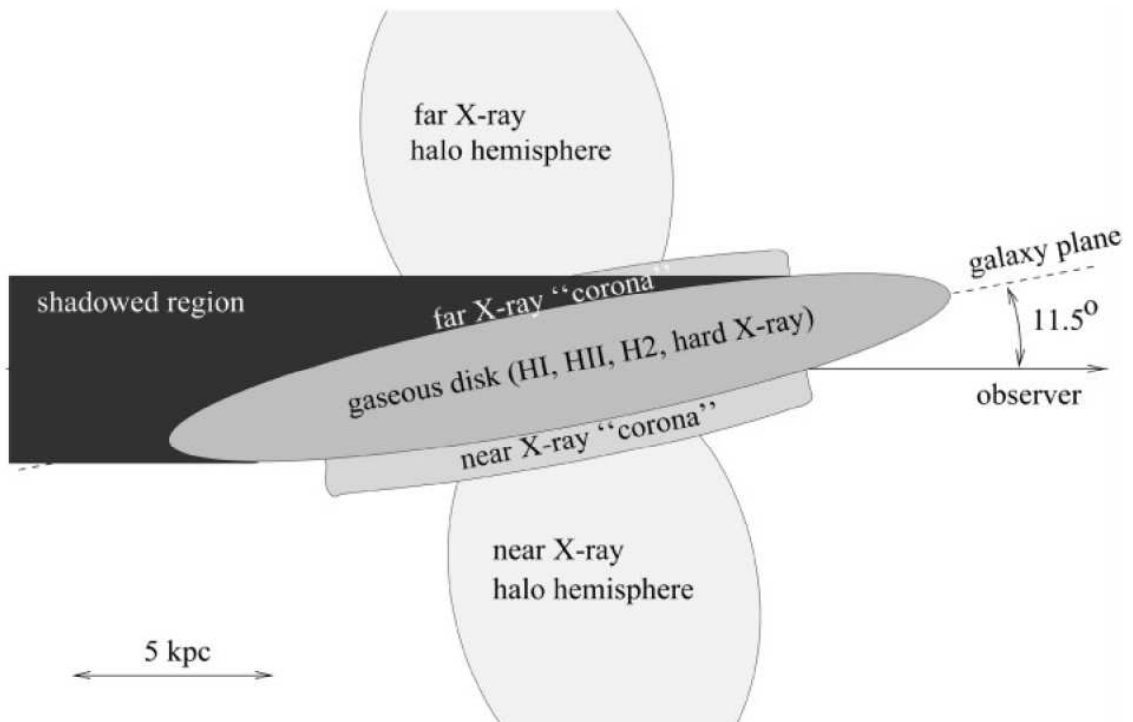
Figure 1.6: Sketch of NGC 253 observing geometry and X-ray halo components (Pietsch et al. 2000).

structure. It is thought to result from hot gas produced by supernovae and hot stars that, like in the starburst nucleus but in a smaller scale, produce superbubbles and galactic fountains which inject hot gas into the interstellar medium. Based on B-band images, Sofue et al. (1994) proposed a boiling disc model. They found dark lanes and filaments in the disc and into the halo and interpreted these as three-dimensional structures where gas is spreading out from the disc into the halo.

From an absorption band in the northwestern part of the galactic disc, the orientation of the disc in 3D space could be derived. Here emission from the northwestern halo behind the disc is absorbed, resulting in a lower surface brightness at low energies (<1 keV). Therefore, we see the side of the disc that is facing southeast, i.e. the northwestern part of the disc is closer to us than the southeastern part (see also Fig. 1.6).

Pietsch et al. (2001) presented a spectral analysis of two regions in the disc. The spectrum of the diffuse emission in these regions could be fit with an absorbed two temperature model (kT=0.13 and 0.5 keV) and solar abundances. A later analysis of a *Chandra* spectrum of the entire disc diffuse emission by Strickland et al. (2002) agrees with these results (kT=0.17 and 0.56 keV). However, in the model that was applied to the *Chandra* spectrum, highly subsolar abundances had to be assumed. This would not be in agreement with the model that the interstellar medium in the disc is enriched with metals by supernovae and stellar winds.

A more detailed analysis of the diffuse emission in the disc as observed with *XMM-Newton* will be presented in Chapter 4.

1.2.3 The superwind

Emanating from the nucleus of NGC 253 a superwind is forcing its way out of the disc into the halo. First evidence for this was found in optical observations by Demoulin & Burbidge (1970), who reported an approach velocity of up to 120 km s^{-1}, relative to the systemic velocity, and interpreted it as an outflow from the centre. Deprojected, this results in an outflow velocity of about 600 km s^{-1}. Possible maximum velocities are even higher with up to a few 10^3 km s^{-1} (Chevalier & Clegg 1985).

In X-rays, the southeastern outflow was first discovered with *Einstein* (Fabbiano & Trinchieri 1984). The northwestern counterpart was later discovered with *ROSAT* (e.g. Pietsch et al. 2000). The northwestern outflow appears harder in X-rays than the emission from the southeastern outflow. This is due to absorption of the disc, which obscures the receding northwestern outflow. Temperatures of the best-fit, thin thermal plasma models are in the range 0.15-0.94 keV from *XMM-Newton* EPIC (Pietsch et al. 2001) and 0.46-0.66 keV from *Chandra* (Strickland et al. 2000).

The southeastern outflow has the shape of a hollow cone with an opening angle of 32°
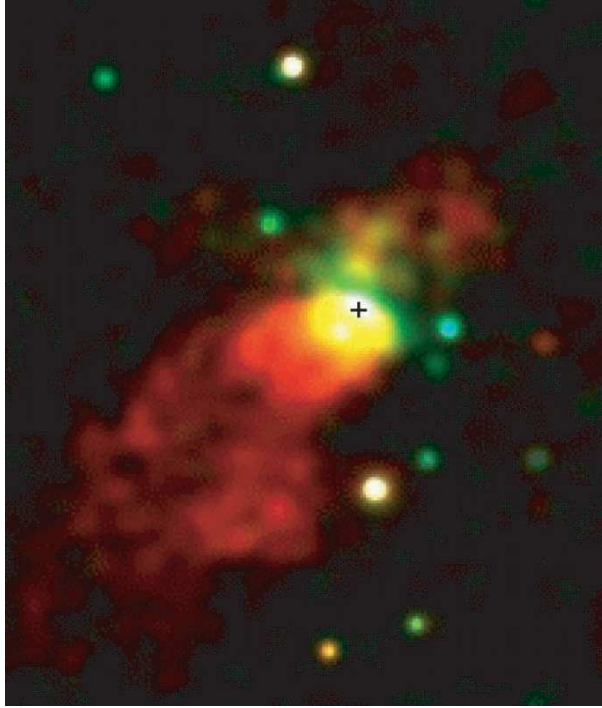
Figure 1.7: Smoothed three-colour composite *Chandra* X-ray image of the central $1.75 \times 2'$ region of NGC 253. Red, yellow, and blue indicate the X-ray 'colours' of 0.2–1.5 keV (soft), 1.5–4.5 keV (medium), and 4.5–8 keV (hard), respectively. The cross marks the position of the radio core (Turner & Ho 1985). From Weaver et al. (2002).

(Pietsch et al. 2000) and a projected extent of 1300 pc along the minor axis (Pietsch et al. 2001). A high spatial resolution *Chandra* image of the nuclear and outflow regions is shown in Fig. 1.7. The outflow showed limb brightening between 0.5 and 0.9 keV, but not at lower energies. The limb brightening confirmed the model, that X-ray emission is produced through shocks at the interface between the superwind and surrounding interstellar material. However, the hot wind fluid itself was considered to be too hot, and to have a too low density to be directly observed in X-rays (Strickland et al. 2000). This picture, however, disregards the possibility that the wind may be mass-loaded, entraining ambient interstellar medium (ISM), as well as infalling material. If turbulent mixing proceeds on a time scale that is larger than the flow time within a given region, such as the base of the outflow, we expect some clumpiness in the outflow, imprinted on an overall less dense wind. As we demonstrate in Chapter 5, this can be confirmed by our analysis, which shows that e.g. emission in the O VIII line is not limb-brightened.
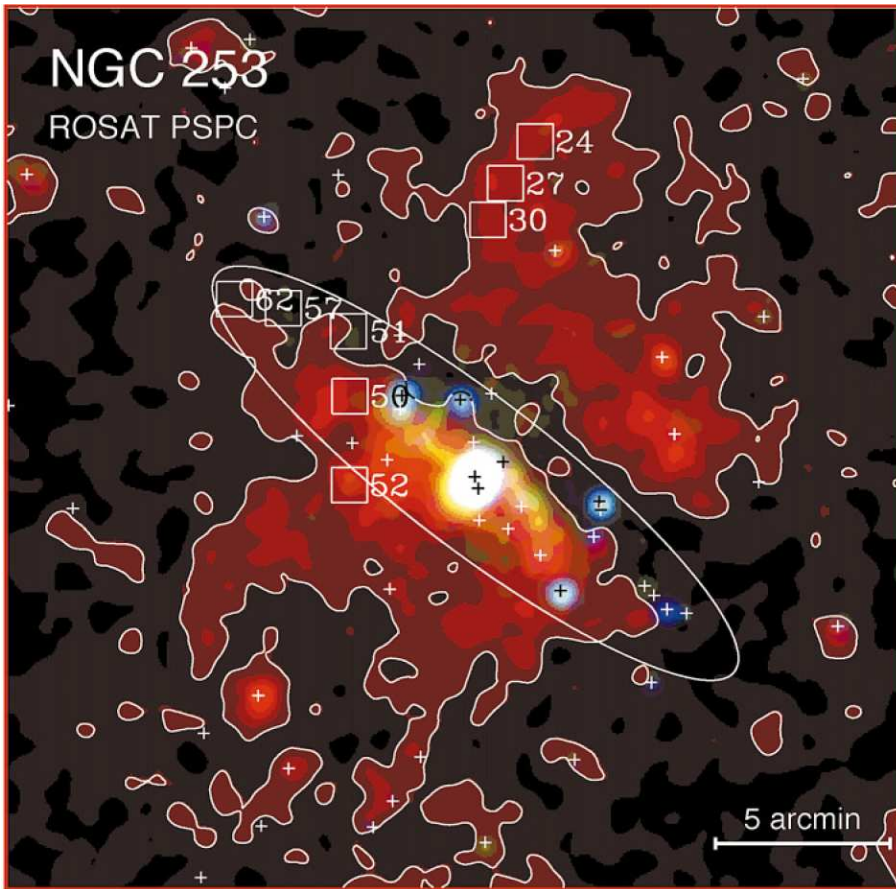
Figure 1.8: *ROSAT* PSPC three-colour composite image of NGC 253 constructed from the image of the soft band ($0.1 - 0.4$ keV) in red, hard1 band ($0.5 - 0.9$ keV) in green, and hard2 band ($1.0 - 2.0$ keV) in blue. The optical size of NGC 253 is indicated by the inclination corrected D_{25} ellipse. Sources from the point source list are given as boxes and crosses. From Pietsch et al. (2000).

1.2.4 The halo

As many other starburst galaxies, NGC 253 also shows a X-ray halo. The northwestern halo was first detected with the *Einstein* observatory by Fabbiano (1988). Its southeastern halo has a softer X-ray spectrum and was first reported with *ROSAT* (e.g. Pietsch et al. 2000). The halo can be traced to projected distances from the disc of about 9 kpc to the northwest and the southeast. A filamentary structure is suggested, that cannot be fully resolved due to the limitations of the *ROSAT* PSPC point spread function (Pietsch et al. 2000). The general shape resembles a horn-like structure, with two horns in both halo hemispheres (see Fig. 1.8).

Strickland et al. (2002) reported on the analysis of the halo X-ray emission using *Chandra* observations. They fitted the northwestern halo emission with a multi-temperature model with two temperatures of 0.24 and 0.71 keV (the latter with quite large errors) and with

a foreground absorption of 5.3×10^{20} cm^{-2}. Sub-solar abundances had to be assumed to achieve a good fit. However, one would expect that the material that is transported by the superwind is mass loaded by chemically enriched material from the starburst region. This would predict high rather than low metallicities. Pietsch et al. (2000) achieved an acceptable fit to *ROSAT* data of the northwestern halo, assuming a foreground absorbed (1.3×10^{20} cm^{-2}, fixed) two-temperature thermal model with temperatures of 0.13 and 0.62 keV and solar abundances. The question of the abundances in the halo medium is still an open question, and will be addressed in Chapter 4.

A power law (photon index $\Gamma = 3.3$) plus a thin thermal plasma (kT $= 0.24$ keV) gave a similarly good fit to the *Chandra* spectrum. Already in earlier publications, such an ambiguity has been found in the spectral fits between a pure multi-temperature thermal plasma model and a combination of thermal plasmas plus a power law component (e.g. Dahlem et al. 2000; Strickland et al. 2002). Origins of the non-thermal component could be point sources, which have not been removed completely, or synchrotron emission from cosmic ray electrons that are advected with the superwind or are accelerated locally in wind shocks. Also this issue will be addressed in Chapter 4.

Strickland et al. (2002) also compare the X-ray morphology to Hα images. They find that the X-shaped soft X-ray morphology of the superwind is matched by very similar X-shaped Hα emission, extending to at least 8 kpc above the plane of the galaxy. Also, the reported total $0.3-2.0$ keV energy band X-ray luminosity of the northern halo ($L_\mathrm{X} \sim 5 \times 10^{38}$ erg s^{-1}) was very similar to the halo Hα luminosity ($L_{\mathrm{H}\alpha} \sim 4 \times 10^{38}$ erg s^{-1}).

In Chapter 4, we will present the results of our analysis of the *XMM-Newton* data of the diffuse halo emission. Multiwavelength information, including the correlations with Hα images, will be used to obtain insights into the structure of the extraplanar gas.

Chapter 2

The XMM-Newton observatory, observations and data reduction

2.1 The X-ray observatory XMM-Newton

XMM-Newton (Jansen et al. 2001) is an European X-ray observatory onboard a satellite that was launched on Dec 10th, 1999 by the European Space Agency (ESA). In total there are 4 telescopes onboard. Three Wolter type-1 X-ray telescopes, with different X-ray detectors in their foci, and a 30 cm optical/UV telescope. The satellite is on a highly elliptical orbit around earth, with an apogee of about $115\,000$ km and a perigee of about $6\,000$ km. The excentricity of the orbit is 0.60 and one orbit takes 47.9 hours. Because of the radiation belt around earth, X-ray observations are only carried out when the satellite elevation is above $46\,000$ km. Below this elevation the radiation background is too high to carry out measurements with an acceptable signal-to-noise ratio (S/N). Often, even at higher elevations, the radiation background can be high. These times have to be screened out from the observation data (see Sec. 2.3.2).

2.1.1 X-ray telescopes

XMM-Newton carries three co-aligned X-ray telescopes. Each of the telescopes consists of 58 Wolter-type grazing-incidence mirror shells, i.e. the X-rays are reflected first on a paraboloidal and secondly on a hyperboloidal shaped mirror. The single mirror shells are nested to obtain a large collecting area. A sketch of the telescopes is shown in Fig. 2.1.
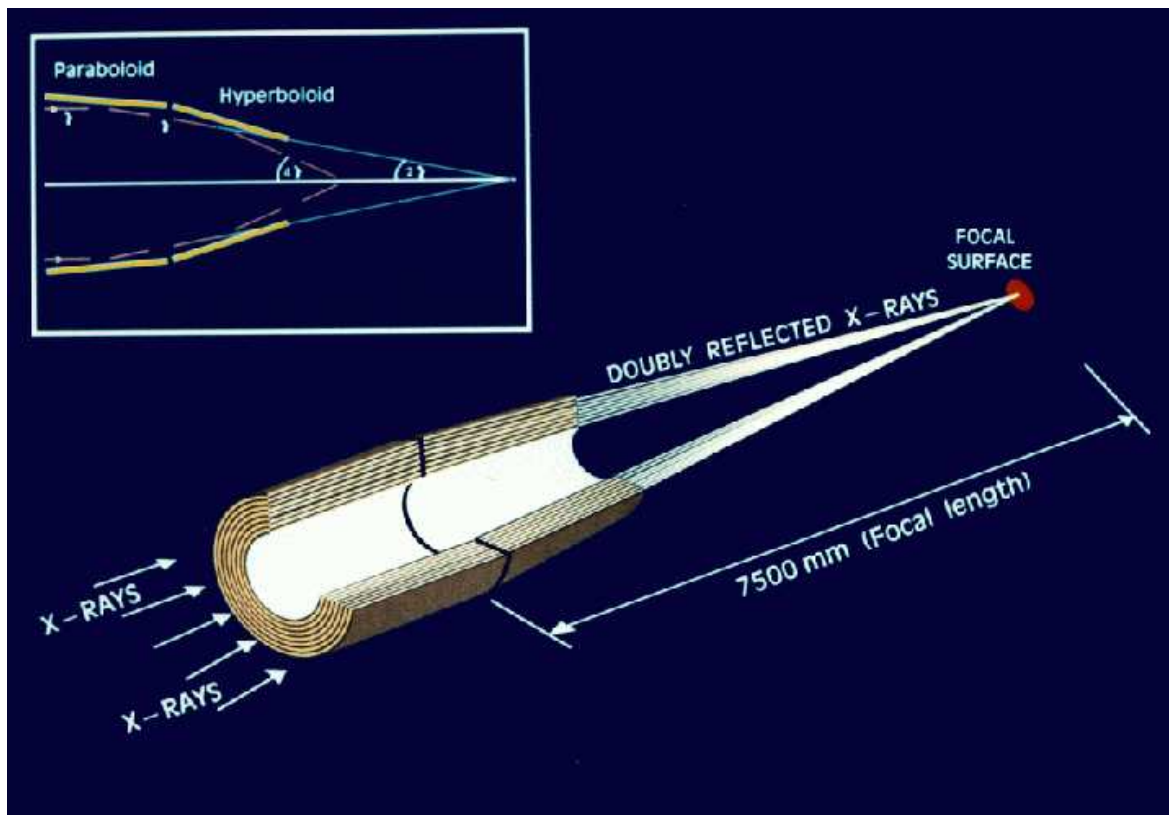
Figure 2.1: The light path through one of the three X-ray telescopes onboard *XMM-Newton* (not to scale). From Ehle et al. (2007).

2.1.2 European Photon Imaging Camera

The European Photon Imaging Camera (EPIC) consists of three CCD cameras with a field of view (FOV) of about 30 arcmin diameter.

EPIC-MOS Two of the EPIC cameras are Metal Oxide Semi-conductor (MOS) CCD arrays (Turner et al. 2001). They share two of the three X-ray telescopes with the Reflection Grating Spectrometers (RGS, see Sec. 2.1.3). The incident photons are focused by the mirrors and then pass through the grating where about half of the telescope incident flux is diverted to the RGS detectors (see Fig. 2.2). Taking the structural obscuration into account, about 40% of the incoming photons reach the MOS detectors. The MOS detectors itself are composed of 7 separate front-side illuminated CCDs, where 6 CDDs surround the CCD in the centre. Each of the 7 CCDs has 600×600 pixels and one pixel (40 micron square) covers 1.1×1.1 arcsec of the FOV. The intrinsic energy resolution of the EPIC-MOS camera is ~70 eV at 1 keV. Its maximum time resolution is 1.75 ms in Timing mode.

In Chapter 3 we will make use of the EPIC-MOS in the spectral analysis of NGC 253

ULX1. Additionally in Chapter 4, the EPIC-MOS is used to detect point sources in NGC 253.

EPIC-PN   The PN detector (Strüder et al. 2001) is in the focal plane of the third X-ray telescope. It is a back-side illuminated CCD and consists of 12 CCD chips on a single Silicon wafer that are aligned in two rows. One of the CCDs has 200×64 pixels, where each pixel (150 micron square) covers 4.1×4.1 arcsec. The intrinsic energy resolution of the EPIC-PN camera is ~ 80 eV at 1 keV. Its maximum time resolution is 7 μs in Burst mode. Compared to MOS, the PN is characterised by a higher sensitivity at energies $\lesssim 1$ keV and $\gtrsim 5$ keV.

The EPIC-PN will be used for imaging of NGC 253 in Chapters 4 and 5, and for spectral analysis in Chapters 3 and 4.

2.1.3   Reflection Grating Spectrometer

Each of the two co-aligned Reflection Grating Spectrometers (RGS, den Herder et al. 2001) consists of an array of reflection gratings located behind the X-ray telescopes which diffracts the X-rays onto an array of 9 CCD detectors. The telescopes are shared with the EPIC MOS detectors (see Fig. 2.2) and about 58% of the incident flux is intercepted by the gratings. The RGS resolving power is 150 to 800 over a range from 5 to 35 Å [0.33 to 2.5 keV] (in the first spectral order), and each CCD contains 1024×384 pixels with a pixel size of 27 micron square. The RGS does not have an entrance slit, thus the whole field of view is mapped onto the detector plane. The field of view in the cross-dispersion direction is determined by the width of the CCDs ($5'$), and the spatial resolution in this direction is largely determined by the imaging properties of the mirrors. In the dispersion direction, the aperture of RGS covers the entire FOV of the mirrors, although the effective area decreases significantly for off-axis sources.

We will make use of the RGS in the analysis of the nuclear outflow of NGC 253 in Chapter 5.

2.1.4   Optical Monitor

The Optical Monitor (OM) is an optical/UV telescope for wavelengths between 180 and 600 nm, co-aligned with the X-ray telescopes. The diameter of its Cassegrain telescope is 30 cm and it covers a field of view of $17'$ with an angular resolution of $\sim 1''$. It can detect sources down to a magnitude of 20.7 with a time resolution of 0.5 s. The OM can be used with different filters (V, B, U, UVW1, UVM2, and UVW2) for imaging or one of two grisms to obtain low-resolution optical or UV spectra. In the following analyses, the OM was not
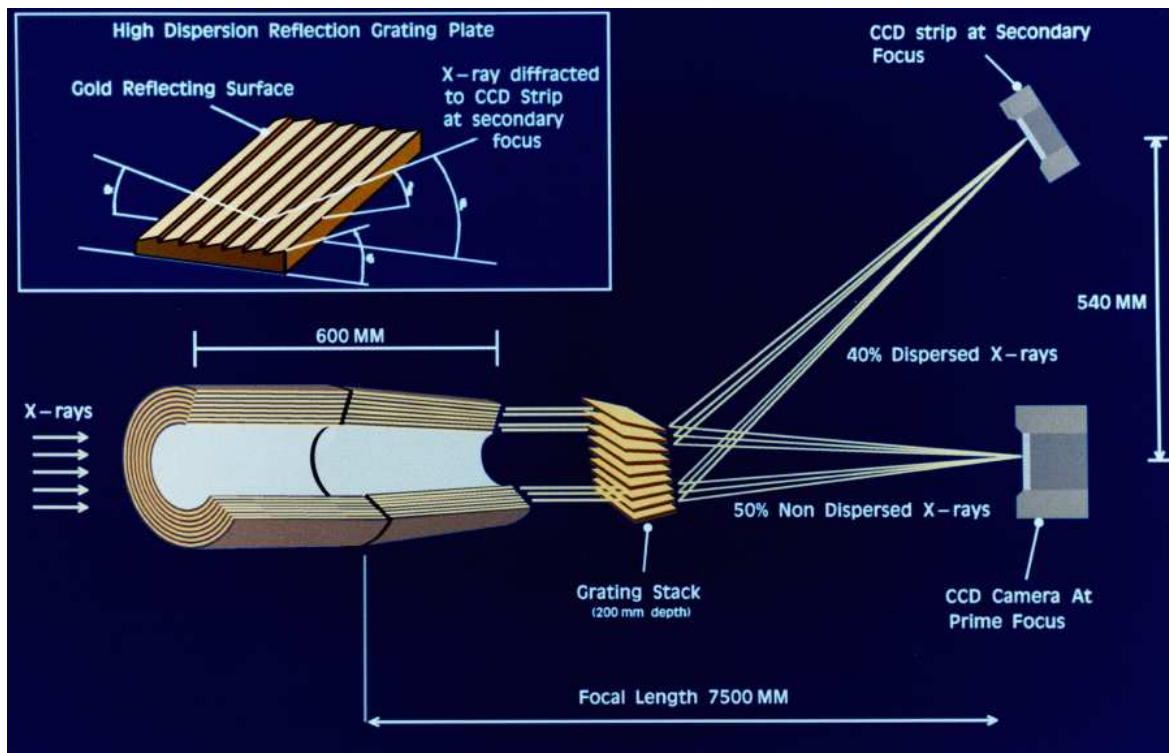
Figure 2.2: X-ray path through the X-ray mirror shells and gratings onto the EPIC MOS detector at the primary focus and the RGS camera at the secondary focus (not to scale). From Ehle et al. (2007).

used. NGC 253 ULX1 was outside of the FOV, and for detecting diffuse emission in the halo the OM images were not deep enough.

2.2 Observations

The startburst galaxy NGC 253 was observed with *XMM-Newton* during three orbits in June and December 2000 and in June 2003 using all of the EPIC instruments and the two co-aligned RGS spectrometers, RGS1 and RGS2, for a total of about 216 ks. The observation identification, revolution number, observing date, pointings and orientation of the satellite (P.A.), and the total exposure time (T_{exp}) are shown in Table 2.1.

Table 2.1: *XMM-Newton* NGC 253 observation log.

Observation number		1	2	3	4
Revolution number		89	89	186	646
Obs. id.		0125960101	0125960201	0110900101	0152020101
Obs. dates		2000-06-03	2000-06-04	2000-12-14	2003-06-19
Pointing direction (J2000)					
RA		00:47:36.74	00:47:36.57	00:47:36.57	00:47:36.89
Dec		-25:17:49.2	-25:17:48.7	-25:15:53.2	-25:17:57.3
P. A.	(deg)	56.9	57.0	233.8	53.8
Filter					
PN		Medium	Thin	Thin	Thin
MOS1		Medium	Medium	Medium	Medium
MOS2		Thin	Thin	Medium	Medium
RGS		-	-	-	-
T_{exp}	(ks)	60.8	17.5	24.4	113.0
$T_{exp, clean}$ (EPIC)[1]	(ks)	39.2	14.2	29.6	110.5
$T_{exp, clean}$ (EPIC)[2]	(ks)	24.3	3.1	4.4	47.9
$T_{exp, clean}$ (RGS)	(ks)	45.1	7.0	(not used)	75.9

2.3   Basic data reduction

The Science Analysis System (SAS)[3] was used for the analysis of the data from *XMM-Newton*. It provides software tools to extract the basic data products like event files and exposure information, and to produce more sophisticated products like images, spectra, light curves, etc. The in the following presented data was analysed using the current version of the SAS together with the most recent calibration files available at the time of the analysis. Additionally, we used existing software like ds9 (Joye & Mandel 2003), ftools[4] (Blackburn 1995), as well as perl and shell scripts, and sophisticated programs in idl and FORTRAN that were developed by ourselves.

---

[3]http://xmm.vilspa.esa.es/sas/
[4]http://heasarc.gsfc.nasa.gov/ftools/

2.3.1   Pipeline products

After downloading the Observation Data Files (ODF) from the archive, the files have to be processed with the latest version of the `SAS` tasks and calibration before they can be used to extract scientific products. This processing was carried out via the metatasks `epchain` and `emchain` for the EPIC PN and MOS data, respectively. For the RGS data we used the metatask `rgsproc`.

The products of the pipeline processing are event files, i.e. tables with entries for each detected photon. This table contains the detection time of the event, the CCD pixel where it was detected, the energy of the photon after correction for gain and charge transfer inefficiency (CTI), and several diagnostic values. Also, via the attitude information of the spacecraft, the sky position for each event is calculated. An example for the diagnostic values are the pattern of the detection, i.e. if a photon was detected only in one, two, thee, four or more pixels and the arrangement of these pixels.

2.3.2   Screening for high background

The radiation background is variable around the *XMM-Newton* operational orbit, depending on the satellite's location with respect to Earth's magnetosphere. For useful *XMM-Newton* science observations to be conducted, the minimum satellite elevation is $46\,000$ km. To remove additional times with high background due to soft proton flares, we produced light curves in the energy range above 10 keV (cf. Fig. 2.3). In this energy range no source counts are expected due to the very low effective area of the telescope. Periods with count rates above a certain threshold were excluded from the data sets.

After screening for times with high particle background, the observations showed no obvious additional times with solar wind charge exchange, which would result in times with high background at energies below 1 keV, so no further exclusion of exposure time was necessary.

The diffuse emission in the halo is a faint source of X-rays. Therefore a careful screening for periods with high background was essential (Chapter 4). In the case of the bright point source NGC 253 ULX1 (Chapter 3), a less stringent screening was necessary. The exposure times after screening for high background ($T_{exp,\ clean}$) are shown in Table 2.1.

For the RGS, we extracted light curves from the background region on CCD 9 to determine the threshold count rate, which we then used to filter the eventfiles. This chip is closest to the optical axis of the telescope, and thus most affected by background flares. The thresholds were 0.25 ct s^{-1} for observations 0125960101 and 0125960201, and 0.20 ct s^{-1} for observation 0152020101, where the count rate was more stable during the non-flaring time intervals.
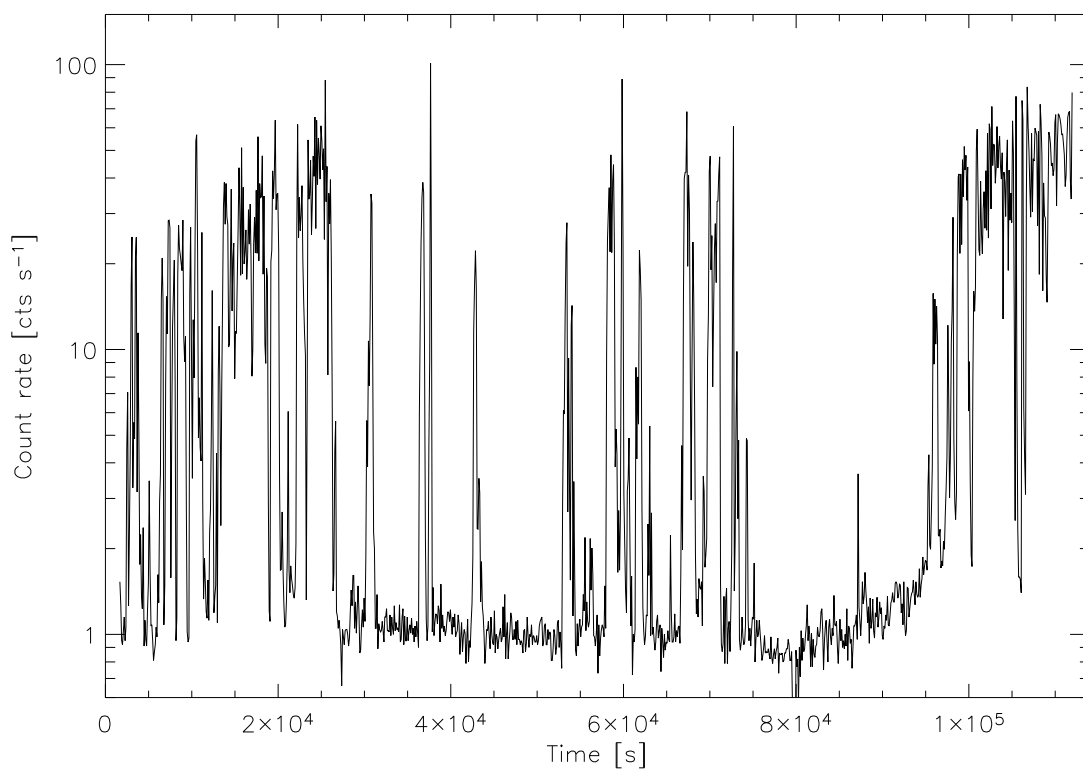
Figure 2.3: High energy (>10 keV) EPIC PN light curve of observation 4, binned to 100 s. The times with high count rates, caused by high particle background exceed the quiescent count rates by almost a factor of 100.

Chapter 3

The recurrent ultra-luminous X-ray transient NGC 253 ULX1

Liu & Bregman (2005) searched for ULXs in 313 nearby galaxies from *ROSAT* HRI observations. One target of this search was the starburst galaxy NGC 253 where they found 21 X-ray sources but only one of them matched their criteria for an ULX (NGC 253 ULX1). This source is located within, but close to the north-east boundary of the D_{25} ellipse of NGC 253.

We here report on a more detailed analysis of NGC 253 ULX1 including *ROSAT*, *XMM-Newton* and *Chandra* data, and specifically on the detection of a second outburst in one of the *XMM-Newton* observations.

3.1 Search for the source in XMM-Newton, Chandra and ROSAT archives

We searched the *ROSAT*, *Chandra* and *XMM-Newton* archive for observations of NGC 253. The results are listed in Table 3.1. Except for two *Chandra* observations the position of NGC 253 ULX1 was always in the field of view (FOV). Besides the first detection in *ROSAT* observation 601111h (Liu & Bregman 2005), NGC 253 ULX1 was only visible in *XMM-Newton* observation 0110900101. These *XMM-Newton* and *ROSAT* HRI data are further discussed in Sect. 3 and 4, respectively.

For the remaining observations we determined 3σ upper limits for the count rate. From that we obtained upper limit for fluxes and luminosities (cf Table 3.1). We used WebPIMMS (v3.6c) with the spectral model we got from the analysis of observation 0110900101 to

determine energy conversion factors. The long term light curve of NGC 253 ULX1 is shown in Fig. 3.1.

3.2 Detailed analysis of XMM-Newton observation 011090-0101

NGC 253 ULX1 was detected for the second time on 2000 December 14 with *XMM-Newton*. The position of the source was within the FOV of both of the MOS and the PN cameras.

We applied the source detection tasks `eboxdetect` and `emldetect` only on the data from the PN detector, as the source was positioned far from the optical axis and close to the edge of the FOV on the MOS detectors. The obtained position was then corrected using optical reference coordinates from the USNO B1 catalogue (Monet et al. 2003) of three AGN, identified by Vogler & Pietsch (1999, sources X4, X22, X58). The corrected position in J2000 coordinates is $\alpha = 00h48m20.11s$, $\delta = -25°10'10''4$ with an error in position of

Table 3.1: Individual observations of NGC 253 ULX1.

Date	Instrument	Observation ID	Duration	Flux^a	$L_X{}^a$
			(ks)	(erg cm^{-2} s^{-1})	(10^{39} erg s^{-1})
1991-12-08	*ROSAT*	600088h-0	3.1	$< 1.1 \times 10^{-13}$	< 0.08
1991-12-25	*ROSAT*	600087p-0	11.6	$< 2.2 \times 10^{-14}$	< 0.02
1992-06-03	*ROSAT*	600087p-1	11.2	$< 4.4 \times 10^{-14}$	< 0.03
1992-06-05	*ROSAT*	600088h-1	25.7	$< 4.4 \times 10^{-14}$	< 0.03
1995-01-03	*ROSAT*	600714h	11.0	$< 5.2 \times 10^{-14}$	< 0.04
1995-06-13	*ROSAT*	600714h-1	19.8	$< 2.0 \times 10^{-14}$	< 0.02
1997-12-20	*ROSAT*	601111h	17.5	1.8×10^{-12}	1.4
1998-07-01	*ROSAT*	601113h	2.0	$< 2.8 \times 10^{-13}$	< 0.2
1999-12-16	*Chandra*	969		not in FOV	
1999-12-27	*Chandra*	790		not in FOV	
2000-06-03	*XMM-Newton*	0125960101	39.2	$< 4.3 \times 10^{-14}$	< 0.03
2000-06-04	*XMM-Newton*	0125960201	14.2	$< 1.8 \times 10^{-14}$	< 0.01
2000-08-16	*Chandra*	383	2.16	$< 8.8 \times 10^{-15}$	< 0.007
2000-12-14	*XMM-Newton*	0110900101	29.6	6.3×10^{-13}	0.5
2003-06-19	*XMM-Newton*	0152020101	110.5	$< 3.6 \times 10^{-15}$	< 0.003
2003-09-19	*Chandra*	3931	83.6	$< 4.4 \times 10^{-15}$	< 0.003

^{a}$0.3 - 10\,$keV luminosity assuming a distance of 2.58 Mpc and a bremsstrahlung model (kT= $2.24\,$keV, $N_H = 1.74 \times 10^{20}\,$cm^{-2})
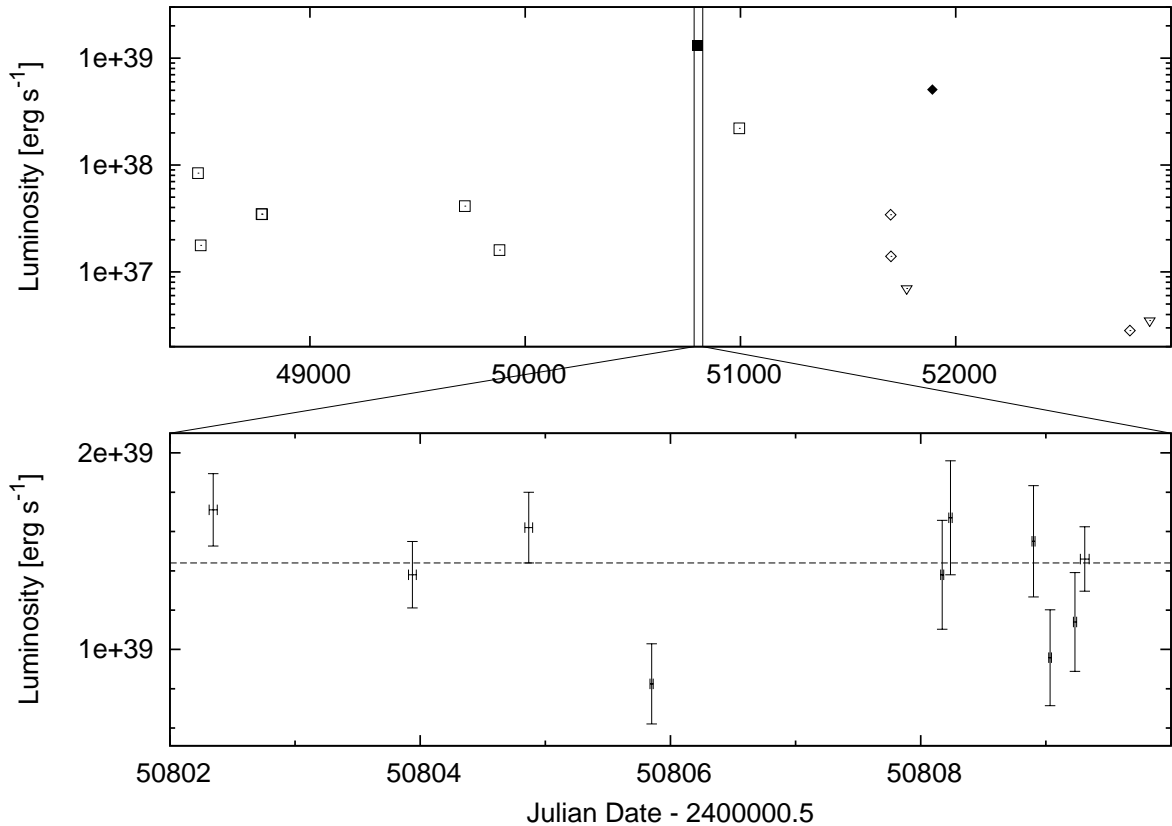
Figure 3.1: Light curve of NGC 253 ULX1. Upper panel: solid symbols represent detections, open symbols 3σ upper limits of NGC 253 ULX1. Different instruments are represented by different symbols: *ROSAT* (squares), *XMM-Newton* (diamonds) and *Chandra* (triangles). Lower panel: Single *ROSAT* HRI exposures with errorbars from observation 601111h where the source was detected. The length of each observation is indicated by the x-errorbar. In contrast to the upper panel the lower panel plot is linear in luminosity.

$0\rlap{.}''3$. The derived position is well within the positional errors given by Liu & Bregman (2005) for NGC 253 ULX1.

A foreground star with a B magnitude of ~ 13 (Monet et al. 2003) is located close ($15.5''$) to the obtained position (Fig. 3.3). We can rule out that the actual detection of NGC 253 ULX1 in observation 0110900101 was caused by this star, as its proper motion of -9.2 mas/yr in RA$\cdot\cos(\text{Dec})$ and -3.6 mas/yr in Dec (Zacharias et al. 2004) is too small to match the detected position of NGC 253 ULX1 with that of the star within the period of observations. Additionally there was no detection of the source in other *XMM-Newton* observations using the same filter.

We extracted energy spectra for NGC 253 ULX1 for all EPIC detectors. For the PN chip we included source counts from an elliptical region with major and minor axes of $27.6''$ and

31

12.3″ respectively. The background region was a circular source-free region with a radius of 48″ on the same CCD close to the source. For MOS the source extraction region was an ellipse with major (minor) axes of 28.95″ (11.3″) for MOS1 and 31.35″ (15.15″) for MOS2, respectively. The background regions were circles with radii of 68″ and 80″ for MOS1 and MOS2, respectively. After subtracting the background the spectra for each instrument were rebinned to a significance level of 3σ.

For the spectral analysis XSPEC 11.3.1 was used. The best-fit parameters from different models provided within XSPEC are listed in Table 3.2. Using the PN and MOS spectra simultaneously the source spectrum was best fitted with a bremsstrahlung model (Fig. 3.2). The fit of the multicolour disk blackbody model (diskpn) would also be acceptable. However, we favour the bremsstrahlung model since it is less complex and gives a better χ^2_{red}. Except for the bremsstrahlung model the foreground absorption (N_H) had to be fixed to the Galactic foreground absorption as a lower limit (1.30×10^{20} cm^{-2}, Dickey & Lockman 1990). If the parameter was free to adjust it converged to unreasonably low values.

From the best fitting spectral model we calculated the source flux and, assuming a distance of 2.58 Mpc (Puche et al. 1991) we derived an unabsorbed luminosity of 5.0×10^{38} erg s^{-1} in the 0.3-10.0 keV band.

In order to study the temporal behaviour of the source a background corrected light curve was created using the tasks `evselect` and `lccorr`. The source count rate was constant at
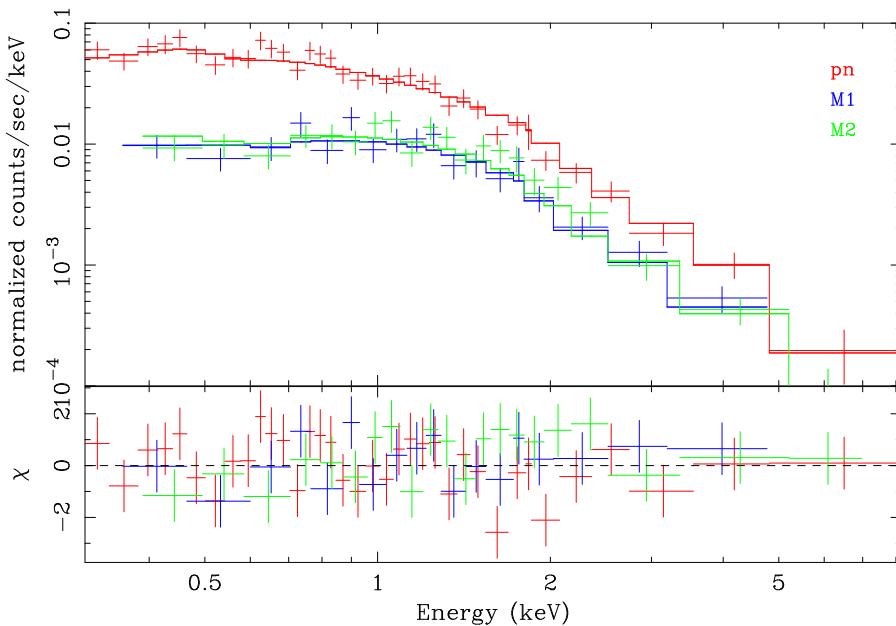
Figure 3.2: Comparison of the PN and MOS spectra of NGC 253 ULX1 with the best-fit bremsstrahlung model. In the lower panel the residuals (in units of σ) between data and model are shown.

Table 3.2: Models for the source spectrum of NGC 253 ULX1

Model[a]	N_H[b] $(10^{20}$ cm$^{-2})$	Model parameter	χ^2_{red}
po	1.30	$\Gamma = 1.94 \pm 0.05$	1.663
bremss	$1.74^{+0.02}_{-0.01}$	kT$= 2.24^{+0.38}_{-0.31}$ keV	0.961
mekal	1.30	kT$= 3.17 \pm 0.19$ keV	2.042
diskbb	1.30	kT$= 0.62 \pm 0.04$ keV	1.671
diskpn	1.30	kT$= 0.69^{+0.06}_{-0.07}$ keV	1.366
		$R = 5.34^{+9.79}_{-2.34} R_S$	

[a]po: power law, bremss: thermal bremsstrahlung, mekal: Mekal thermal plasma, diskbb: multiple black-body disk, diskpn: accretion disk around a black hole
[b]all models are modified by foreground absorption (XSPEC model `wabs`).

about 0.8 ct s^{-1} within the errors of about 15% during observation 0110900101.

3.3 Analysis of ROSAT observation 601111h

The first detection of NGC 253 ULX1 was in *ROSAT* observation 601111h (Liu & Bregman 2005). The observation (total exposure time 17.5 ks) is spread over ten observing intervals, with different exposure and waiting time for the individual observations. The source was bright enough to determine luminosities for each of these observation intervals.

We calculated count rates using the EXSAS source detection task `detect/sources`. To reduce noise we only analysed HRI channel 2-15. We used WebPIMMS (v3.6c) and the spectral model retrieved from the *XMM-Newton* observation (bremsstrahlung, kT$= 2.24$ keV, $N_H = 1.74 \times 10^{20}$ cm^{-2}) to determine energy conversion factors to obtain the corresponding fluxes and luminosities (see lower panel of Fig. 3.1). The luminosity averaged over the whole observation (1.43×10^{39} erg s^{-1}) is indicated by the dashed line.

During the observation the source showed significant variability by at least a factor of 2.

3.4 Discussion

We detected the recurrence of NGC 253 ULX1 in the *XMM-Newton* observation from 2000 December 14. This was the first detection after the outburst in 1997, reported from *ROSAT* HRI observations by Liu & Bregman (2005). In all other observations of NGC 253 the luminosity of the source was below the detection limit. This implies brightness variability
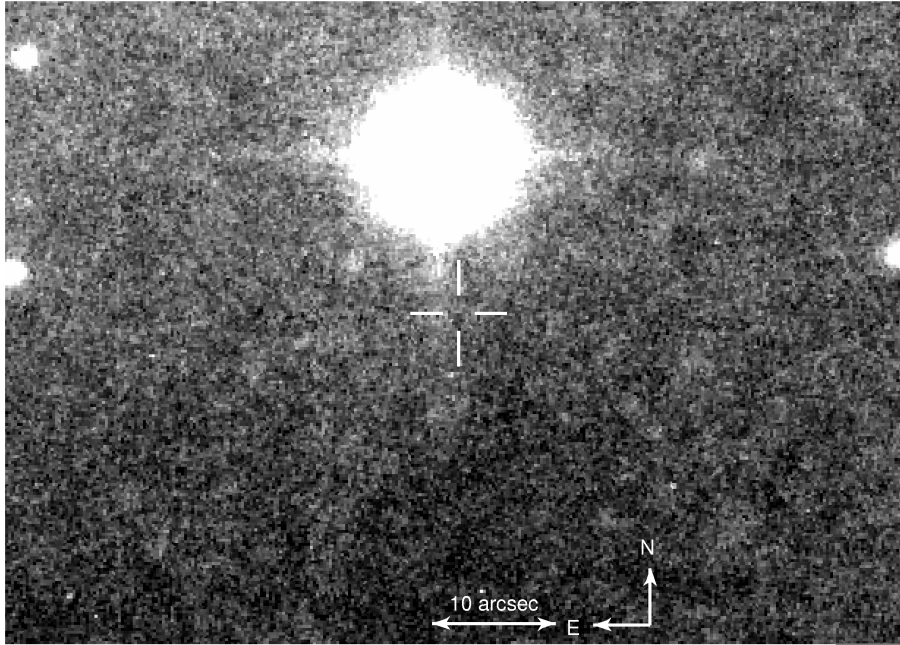
Figure 3.3: R-Band optical image taken with the Wide Field Imager on the MPG-ESO 2.2m Telescope. The source is located close to a ~ 13 mag star. The R magnitude is 24.2.
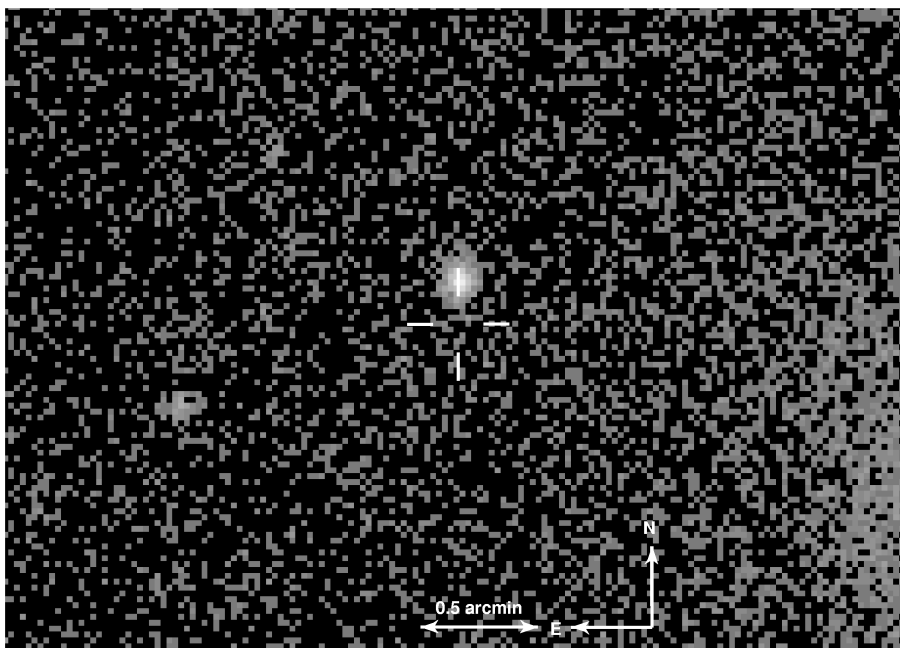
Figure 3.4: Near UV image taken with GALEX. The NUV magnitude is 22.

by at least a factor of 500. Its fastest change in luminosity (L_{max}/L_{min}) exceeds a factor of 71 in 120 days.

The improved position (errors of $0\overset{''}{.}24$ compared to $4''$- $10''$) of the source determined in Sect. 3 allowed us to search for optical counterparts. We checked images taken with the Wide Field Imager (WFI) on the MPG-ESO 2.2m Telescope at La Silla in the R- (Fig. 3.3), I- and B-band (limiting magnitudes 24.2, 22.9 and 24.3, respectively) and images taken with the Galaxy Evolution Explorer (GALEX, a space telescope from NASA observing in the ultraviolet) in the NUV (Fig. 3.4) and FUV (limiting magnitudes 22 and 23, respectively), but no counterpart could be detected.

With the data discussed in Sect. 3 and 4 we can exclude that NGC 253 ULX1 is either a foreground object or a background AGN based on three arguments: (i) We estimated the $\log(f_X/f_{opt}) = \log f_X + (m_V/2.5) + 5.37 > 3.2$ using the flux of the *ROSAT* detection and a lower limit for m_V of 24.2 (averaging the limiting magnitudes of the R- and the B-WFI images, see above). Following Maccacaro et al. (1988) this value exceeds that expected for galactic sources (-4.6 to -0.6) as well as AGNs (-1.2 to $+1.2$). (ii) The variability of NGC 253 ULX1 is by a large factor higher than the typical value observed for AGNs ($\sim 10 - 60$). (iii) NGC 253 ULX1 shows a bremsstrahlung spectrum, whereas spectra of AGNs above $2\,keV$ are typically fitted by a power law. The recurrent outbursts also exclude that the source is the luminous remnant of a recent supernova, like e.g. SN1993J in M81 (Zimmermann & Aschenbach 2003).

The X-ray spectrum may indicate that NGC 253 ULX1 is a low mass X-ray binary (LMXB). The X-ray emission in these objects is created in the optically thin boundary layer between the disk and the neutron star and comptonization may dominate the spectral emission (White et al. 1988), leading to a spectrum that can be fitted with a bremsstrahlung model. However the *ROSAT* HRI peak luminosity of 1.43×10^{39} erg s^{-1} is very high for typical LMXBs. Other systems that show bremsstrahlung spectra are black hole X-ray binaries, e.g. Cyg X-1 (Sunyaev & Truemper 1979), LMC X-3 and X1755-33 (White et al. 1988). These systems may contain a high or low mass companion.

An additional argument for a low mass companion comes from the lack of an optical counterpart (see above). High mass X-ray binaries (HMXBs) should be detectable at about 22 to 24 mag, extrapolating V magnitudes from HMXBs in the Magellanic Clouds (Liu et al. 2000). We would have detected an object of this brightness in the WFI data.

The luminosity of a compact object radiating at the Eddington limit is given as $L_{Edd} = 1.5 \times 10^{38}(M/M_{\odot})$ erg s^{-1}, when electron scattering dominates the opacity. Luminosities higher than 2×10^{38} erg s^{-1} (corresponding to a $1.4 M_{\odot}$ object, commonly assumed as the maximum mass of a neutron star) suggests that the compact object is a black hole. According to NGC 253 ULX1's maximum luminosity of 1.43×10^{39} erg s^{-1} the lower limit for the mass

of the black hole is 11 M$_\odot$. Therefore NGC 253 ULX1 is not required to be an IMBH.

Another argument against an IMBH is the temperature of NGC 253 ULX1. Miller et al. (2004a) compared intermediate mass black hole candidate ULXs and stellar mass black holes with respect to luminosity and temperature. If we assume the multicolour disk blackbody model then NGC 253 ULX1's position in the luminosity-disk temperature diagram (Fig. 2 in Miller et al. 2004a) indicates that NGC 253 ULX1 is not an IMBH, but a stellar mass black hole.

Recently another object was found that, like NGC 253 ULX1, showed also a bremsstrahlung spectrum: X-44 in the Antennae Galaxies (NGC 4038/4039) (Miller et al. 2004b). The temperature of X-44 is 3.7 ± 0.5 keV and its luminosity is $1.0^{+1.3}_{-0.2} \times 10^{40}$ erg s^{-1}. This temperature is about a factor of 1.5 higher than in NGC 253 ULX1, and the luminosity exceeds the luminosity of NGC 253 ULX1 by a factor of 15 compared to the outburst in 1997.

Another interesting ULX to compare NGC 253 ULX1 with is M101 ULX-1 (Kong et al. 2005). It was the first ULX that like NGC 253 ULX1 has been observed during more than one ultra-luminous outburst. Like many other ULXs the spectrum of M101 ULX-1 is best described with an absorbed blackbody model, but the temperature of $\sim 50 - 160$ eV is rather low. M101 ULX-1 has a peak luminosity of about 10^{41} erg s^{-1} ($0.3 - 7$ keV), and the hardness of its spectrum changed between different observations. We do not know whether the spectrum of NGC 253 ULX1 changed in the two observations, as the *XMM-Newton* data provided the very first spectrum of the source. During 12 years of observations NGC 253 ULX1 showed two outbursts with an interval of three years. In M101 ULX-1 the two outbursts are only separated by half a year. On shorter time scales NGC 253 ULX1 showed only one drop in luminosity by a factor of ~ 2 during the *ROSAT* observation, and in the *XMM-Newton* observation (exposure time 8.2 h) no variability could be detected. M101 ULX-1 on the other hand does show short-time-scale variability. Its luminosity changed by a factor of $\gtrsim 10$ on a time scale of hours. The lack of short time variability of NGC 253 ULX1 argues against the relativistic beaming model, since this would require a very stable jet (Reynolds et al. 1997).

Chapter 4

The diffuse emission in the disc and the halo of NGC 253

The diffuse X-ray emission of starburst galaxies can be quite prominent. Especially in galaxies that we see edge-on, we can find very complex emission from galactic halos. One famous example is the starburst galaxy NGC 253 in the Sculptor Group. It is close enough (2.58 Mpc, $1'$=750 pc, Puche et al. 1991) to resolve structures in the disc and halo, and to separate the detected point sources from the diffuse emission. Also, it is seen almost edge-on (78.5°, Pence 1980), so an unobscured analysis of the halo emission is possible. NGC 253 has been observed in X-rays many times. There are observations with *Einstein* (e.g. Fabbiano & Trinchieri 1984), *ROSAT* (e.g. Pietsch 1992; Read et al. 1997; Dahlem et al. 1998; Vogler & Pietsch 1999; Pietsch et al. 2000), *ASCA* (e.g. Ptak et al. 1997), *Beppo*SAX (e.g. Cappi et al. 1999), *XMM-Newton* (e.g. Pietsch et al. 2001; Bauer et al. 2007b), and *Chandra* (e.g. Weaver et al. 2002; Strickland et al. 2002, 2004a,b). While with some instruments one was not able to separate emission from point sources and diffuse emission, other instruments, especially *ROSAT*, *XMM-Newton*, and *Chandra*, do have a narrow enough point spread function to do so. We here report on the first extensive analysis of the diffuse emission in NGC 253 with *XMM-Newton*.

4.1 EPIC data reduction

Throughout the following analysis, we used the MOS data *only* to detect and remove point sources. We were especially interested in low-surface brightness diffuse emission at energies below 1 keV, where the MOS detectors have a lower sensitivity than the EPIC PN. By not utilising the MOS data for the analysis of the diffuse emission, we avoided a higher

background noise level.

After screening for times with high particle background (for the resulting exposure times see Table 2.1), the observations showed no obvious additional times with solar wind charge exchange (e.g. Snowden et al. 2004), which would result in times with high background at energies below 1 keV, so no further exclusion of exposure time was necessary. The exposure times after screening for high background ($T_{exp, clean}$) are shown in Table 2.1. Summing up over the final good time intervals, we ended up with 80 ks of exposure time in total. This means only about 37% of the original exposure time could be used for the analysis presented in this chapter. This number is quite small, compared to typical exposure time fractions of usable times after screening of 60–70%[1]. Next, we screened for bad pixels that were not detected by the pipeline. In order to be able to merge images later on, we calculated sky coordinates (*X,Y*) for the events in all observations with respect to the centre reference position α_{2000}=00^{h}47^{m}33$.\!^s$3, δ_{2000}=-25°17′18″. For the following analysis we split the data set into five energy bands: 0.2–0.5 keV, 0.5–1.0 keV, 1.0–2.0 keV, 2.0–4.5 keV and 4.5–12 keV as bands 1 to 5.

4.1.1 Point source removal

In this chapter we focus on the diffuse emission in the halo and the disc of the galaxy. To do so, we had to remove contributions from point sources. In order to run the source detection algorithm of the SAS-software package, we created images for the PN, selecting only single events (PATTERN=0) in energy band 1, and single and double events (PATTERN≤4) for the other bands. For MOS we used single to quadruple events (PATTERN≤12) in all bands. To avoid differences in the background over the PN detector, we omitted the energy range between 7.2 keV and 9.2 keV, where the detector background shows strong spatially variable fluorescence lines (Freyberg et al. 2004). We created images, background images and exposure maps, and masked them to an acceptable detector area. The binning for all images is 2″.

We searched for point sources in the field of view (FOV), simultaneously in the 5 energy bands and three detectors. First, we searched in each observation separately, to correct for inaccuracies in the pointing positions. The resulting source lists were correlated to catalogues from USNO (Monet et al. 2003), SIMBAD[2], and *Chandra* (Strickland et al. 2002). Offsets were determined and applied to each observation. With the position corrected event files, we again created images on which we executed the final point source detection. We searched

---

[1]see the *XMM-Newton* EPIC Background Working Group webpage http://www.star.le.ac.uk/~amr30/BG/BGTable.html

[2]http://simbad.u-strasbg.fr/simbad/
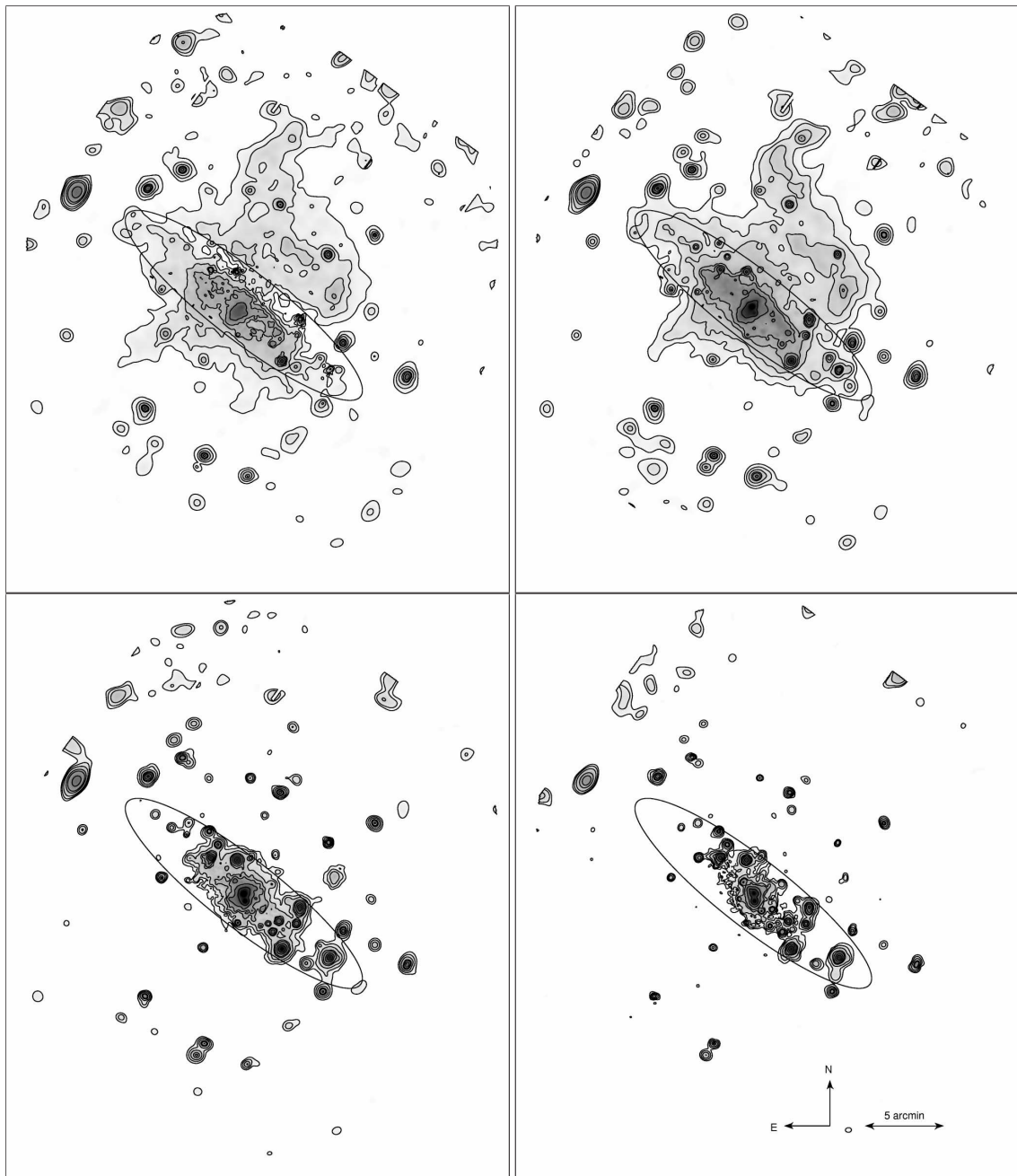
Figure 4.1: Adaptively smoothed EPIC PN images with contours in the lower 4 energy bands: (top-left) 0.2–0.5 keV, (top-right) 0.5–1.0 keV, (bottom-left) 1.0–2.0 keV, and (bottom-right) 2.0–4.5 keV. Contours are at (0.35, 0.50, 0.80, 1.6, 2.5, 6.0, 20, 100) $\times$ 10^{-5} ct s^{-1} pix^{-1}. Additionally we show the inclination corrected optical D_{25} ellipse in black.
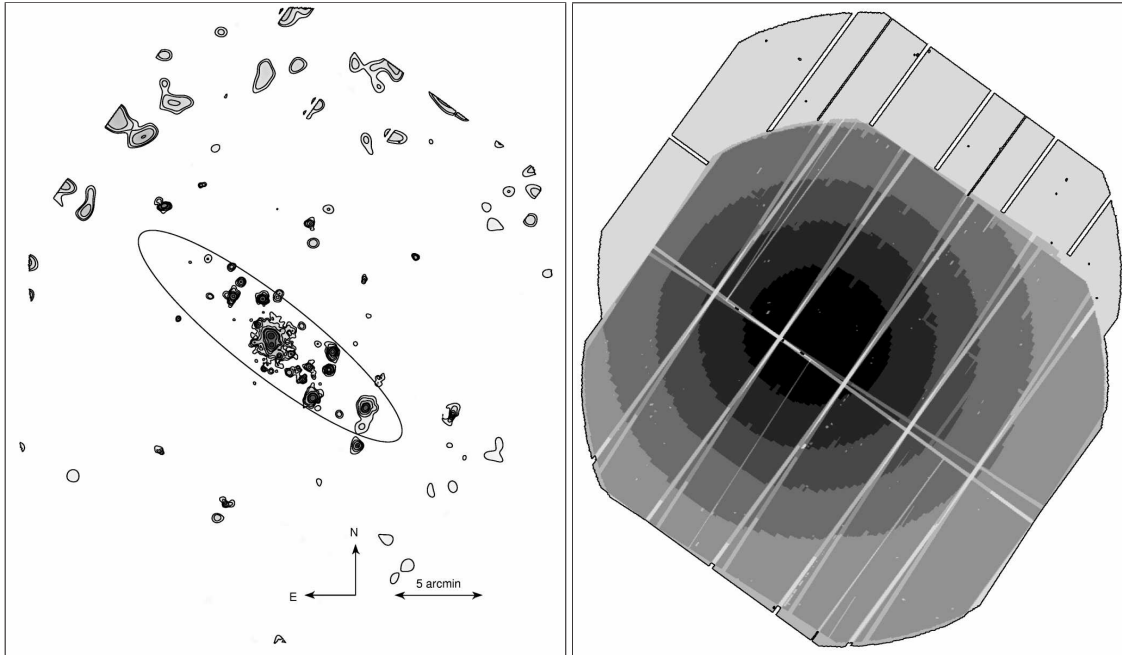
Figure 4.2: *(left):* Adaptively smoothed EPIC PN image with contours in the highest different energy band (4.5–12 keV). Contour levels are the same as in Fig. 4.1. *(right):* The vignetting corrected exposure map of the merged four observations. The outer contour indicates 0 ks and the exposure increases linearly towards the centre by one seventh of the maximum (80 ks) per gray-scale level (0–11.4 ks, 11.4–22.9 ks, 22.9–34.3 ks, 34.3–45.7 ks, 45.7–57.1 ks, 57.1–68.6 ks, 68.6–80.0 ks). Except for a few pixels, all the detector gaps are covered by at least 4.4 ks in the central region.

in the merged images from observations 1, 2, and 4, and separately in the images from observation 3. The reason for merging only observations 1, 2 and, 4 is that observation 3 has a pointing offset ($\sim 6'$) into the northwestern halo and therefore we would have different point spread functions on the same sky coordinates.

Additionally, we created a point source catalogue for the *Chandra* observations. Point sources in *Chandra* ObsID 3931 were identified using the Wavelet-Based detection Algorithm (`wavdetect` in the `ciao` software, version 3.4, Freeman et al. 2002), in the 0.5–5.0 keV energy band using scales of $1''$, $2''$, $4''$, $8''$, and $16''$. For ObsID 969 and ObsID 790 we adopted the published source list from Strickland et al. (2002). The combined *XMM-Newton* and *Chandra* source list will be published and further discussed in a forthcoming publication (Trinchieri et al. in preparation).

The combined source list was used to remove the point sources from the data sets. The `SAS`-task `region` was used to produce elliptical regions that approximate the point spread function (PSF) with an analytical model at a given detector position and flux value (0.5 times

the background flux at this position). Sources that were not detected in the *XMM-Newton* data sets, but are known from *Chandra* observations, were excluded with a circular region with a diameter of $8''$. One might argue that these sources contribute only little to the overall emission. However, we took up a conservative position and also excluded these sources to keep any unwanted interference at a minimum. An extended source, most likely a galaxy cluster candidate in the background was additionally masked with a circular region of $1.5'$ diameter.

4.1.2 Images

We used all 4 observations of NGC 253 to produce images. The observations have different pointing directions and position angles, so we obtained images where almost all the CCD gaps are filled. The single images, from the energy bands 1 to 5, were corrected for the detector background (electronic noise, high energy particles) by subtracting the surface brightness of the detector corners, that are outside of the field of view. The images were exposure and vignetting corrected, and adaptively smoothed with a Gaussian kernel, with sizes between $10''$ and $47''$ (Fig. 4.1 and 4.2). For a detailed description of this method see App. C. A false-colour image was produced by combining the three lowest energy bands 1, 2, and 3, as channels red, green, and blue, respectively (Fig. 4.3). The image, after the point source removal is shown in Fig. 4.4.

4.1.3 Hardness ratio maps and spectra

As a big advantage, compared to the observations by *ROSAT* and *Chandra*, the higher count rates in *XMM-Newton* allowed us to extract spectra with reasonable statistics from smaller regions in the disc and the halo. For the hardness ratios and spectra we again restricted ourselves to the EPIC PN data. We did not use observations 2 and 3 for hardness ratios and spectra, because after good time interval screening only little exposure was left (cf. Table 2.1).

Energy spectra of several regions (cf. Fig. 4.4) were extracted from the event files after removal of the point sources. To calculate the area of these regions, we used the task `backscale`. We produced background spectra using a region at the southwestern border of the FOV, together with observations where the filter wheel was closed. A detailed description of this procedure, which also handles the binning of the spectra, can be found in Appendix D. The final, background subtracted source spectrum for each region has a significance of at least $3\,\sigma$ in each data bin.

Since the emission is mostly confined to energies between 0.2 and 2.0 keV, we only calculated the hardness ratios HR1 and HR2, where HR1=$(B_2-B_1)/(B_2+B_1)$, and HR2= $(B_3$-

B_2)/(B_3+B_2). B_1, B_2, and B_3 are the count rates in the energy bands 1 to 3, i.e. 0.2–0.5 keV, 0.5–1.0 keV, and 1.0–2.0 keV, respectively. They were obtained by summing up the background subtracted counts in the spectra in the energy bands and observations.

In order to fit the spectra with physical models, we created the proper response and anxiliary response files for extended sources for each spectrum. In XSPEC 11.3.2, we linked the model parameters between the two observations and included a global renormalisation factor to account for differences between the observations to fit the spectra from observations 1 and 4 simultaneously.

4.2   Results

To characterise the diffuse emission in the disc and the halo, we analysed images in different energy bands, and hardness ratios and spectra from several regions. In the disc the regions were chosen in a way that they follow the spiral arm structure. In the halo, we chose plane-parallel regions above the galactic disc. The projected heights of the halo regions are 2 kpc, with exception of the region furthest to the northwest (region 1), which has a projected height of 3 kpc. The regions are overplotted on top the false-colour X-ray image in Fig. 4.4. The hardness ratios in the different regions are given in Table 4.1 and shown graphically in Fig. 4.5.

4.2.1   Disc diffuse emission

The disc shows diffuse emission in energies up to ~10 keV, where the harder emission is located close to the centre of NGC 253. The soft emission (<1 keV) shows the largest extent along the major axis. From the nucleus, it reaches ~7.0 kpc to the northwest and ~6.4 kpc to the southeast.

A prominent feature in the disc is the lack of very soft emission northwest of the major axis. This is already known from *ROSAT* observations (e.g. Pietsch et al. 2000) and can be explained by the geometry of the system: The galaxy's disc is oriented so that we see the underside of the disc. The emission from the northwestern halo behind the disc is therefore absorbed by the intervening disc material.

The spectral properties in different regions of the disc are summarised in Table 4.1. An example of a disc spectrum (region 14) is shown in Fig. 4.6. The visible lines are from O VII (~0.57 keV), O VIII (0.65 keV), Fe XVII (0.73–0.83 keV), Ne IX (~0.91 keV), Ne X (1.0 keV), Mg XI (~1.3 keV), and Si XIII (~1.9 keV).

To fit the spectra, we tried several different models, which all contain an absorption model (tbabs, Wilms et al. 2000) for the Galactic foreground N_H of 1.3×10^{20} cm^{-2} (Dickey
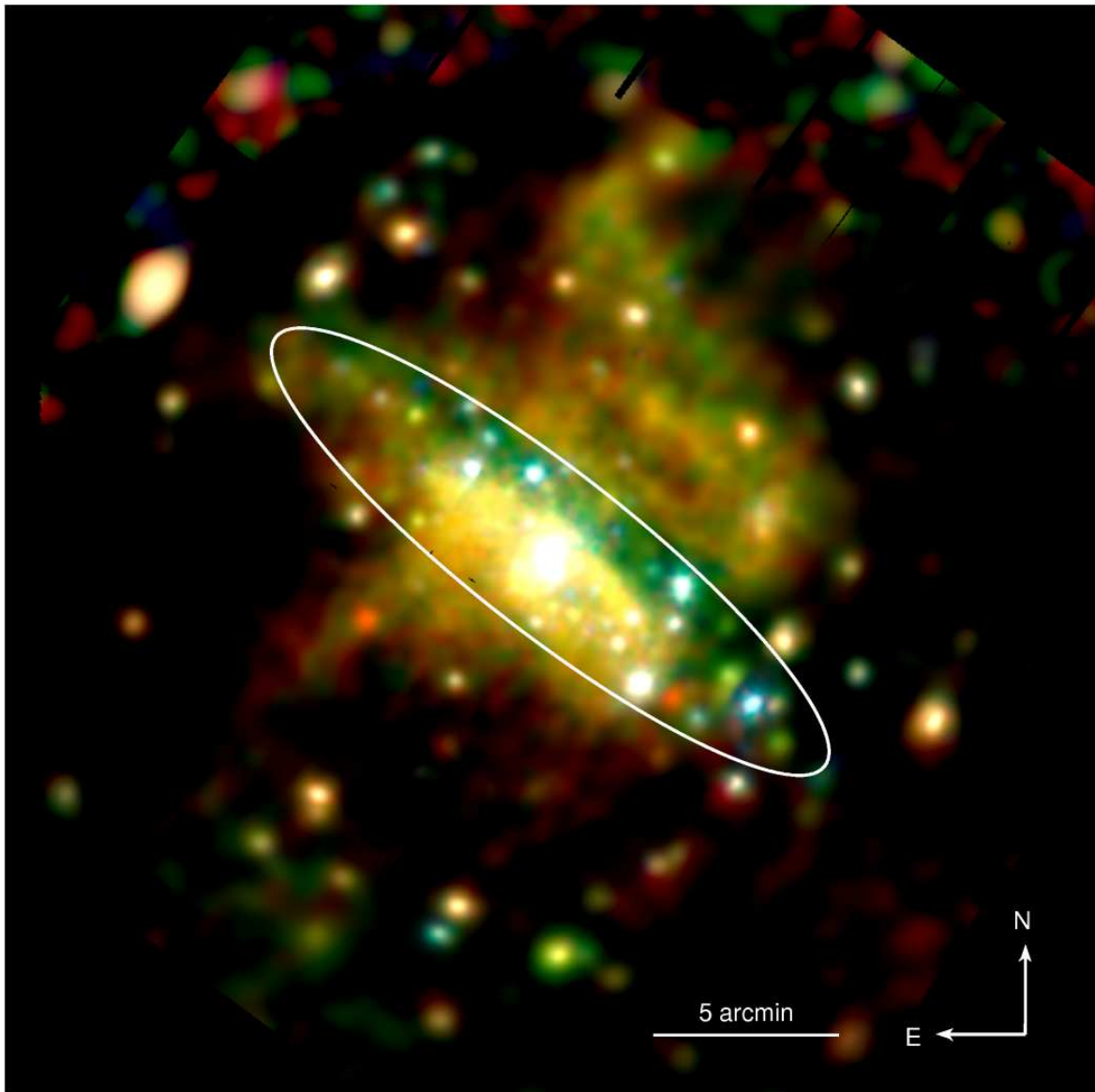
Figure 4.3: Adaptively smoothed EPIC PN image of NGC 253. The colours correspond to the energy bands (0.2–0.5 keV, red), (0.5–1.0 keV, green) , and (1.0–2.0 keV, blue). Overplotted in white is the inclination corrected optical D_{25} ellipse of NGC 253. Scale and orientation are indicated.
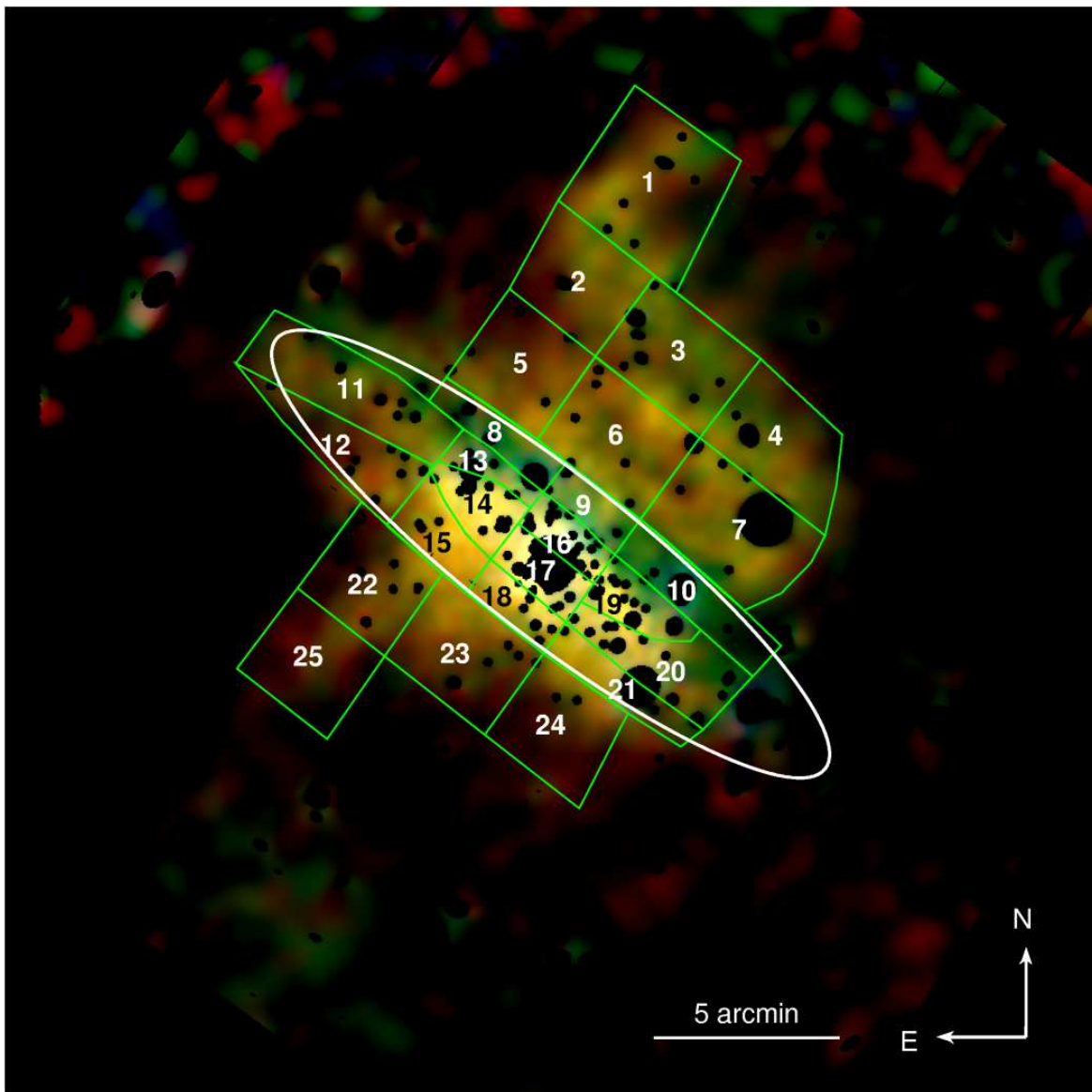
Figure 4.4: Adaptively smoothed EPIC PN image of the diffuse emission of NGC 253. Point sources have been removed. Overplotted in green are the regions that were used for extracting hardness ratios and spectra. The inclination corrected optical D_{25} ellipse is shown in white.

& Lockman 1990). Also the abundances were fixed to solar values (see also Sec. 4.3.4) from Wilms et al. (2000). A simple one-temperature thin thermal plasma model (apec, Smith et al. 2001) did not result in a good fit (i.e. $\chi^2_\nu \leq 1.4$) in any case. Similarly, a power law model did not give good fits. At least three components were necessary for most of the regions: two thin thermal plasmas plus a power law component. The power law was needed to account for the emission above $\sim$1 keV and probably results from point sources below the point source detection limit, or incomplete source removal due to too small extraction radii.

The obtained temperatures are quite uniform throughout the disc and vary from 0.1 to 0.3 keV and from 0.3 to 0.8 keV for the soft and the hard component, respectively. The intrinsic luminosity (corrected for Galactic absorption) of the diffuse emission within the inclination corrected optical D_{25} ellipse is 2.4×10^{39} erg s^{-1} (0.2–10.0 keV), or 8.5×10^{38} erg s^{-1} (2.0–10 keV). Both values were corrected for the area of cut-out point sources.

The spectra decrease in hardness from the northwest to the southeast parallel to the minor axis, which can easily be seen in the hardness ratio maps (Fig. 4.5). This is not an effect caused by different temperatures, but by the increasing strength of the soft spectral component towards the southeast (compared to the hard component), as the optical depth through the halo on the near side of the disc increases.

The regions along the northwestern outflow (regions 9 & 16) as well as the region northeast to that (region 13) allow a lower limit estimate of the absorption through the disc. Here an additional absorption component was required to achieve a good spectral fit. The required column densities range between $\sim$0.5$\times 10^{22}$ cm^{-2} and $\sim$0.9$\times 10^{22}$ cm^{-2}.

In a few cases, the two thermal plasma plus a power law component model did not give the best fit. The southern region on the northeastern end of the disc (region 12) did not require a power law component. It does not cover a spiral arm of NGC 253, thus the contribution from point sources below the detection limit may not be significant. The region furthest to the south in the disc (region 21) was well fit with one thermal plasma and a power law. A second thermal plasma was not required.

We found that spectra are harder in regions which cover spiral arms. The northeastern regions of the disc (regions 11 & 12) are the best example for this. The region which covers the spiral arm (region 11) shows temperatures of $0.18^{+0.05}_{-0.04}$ and $0.58^{+0.16}_{-0.18}$ keV, whereas the region adjacent to the spiral arm (region 12) is significantly cooler with temperatures of 0.07 ± 0.01 and $0.25^{+0.04}_{-0.03}$ keV. The latter spectrum is actually more similar to the typical halo spectrum (see next section).
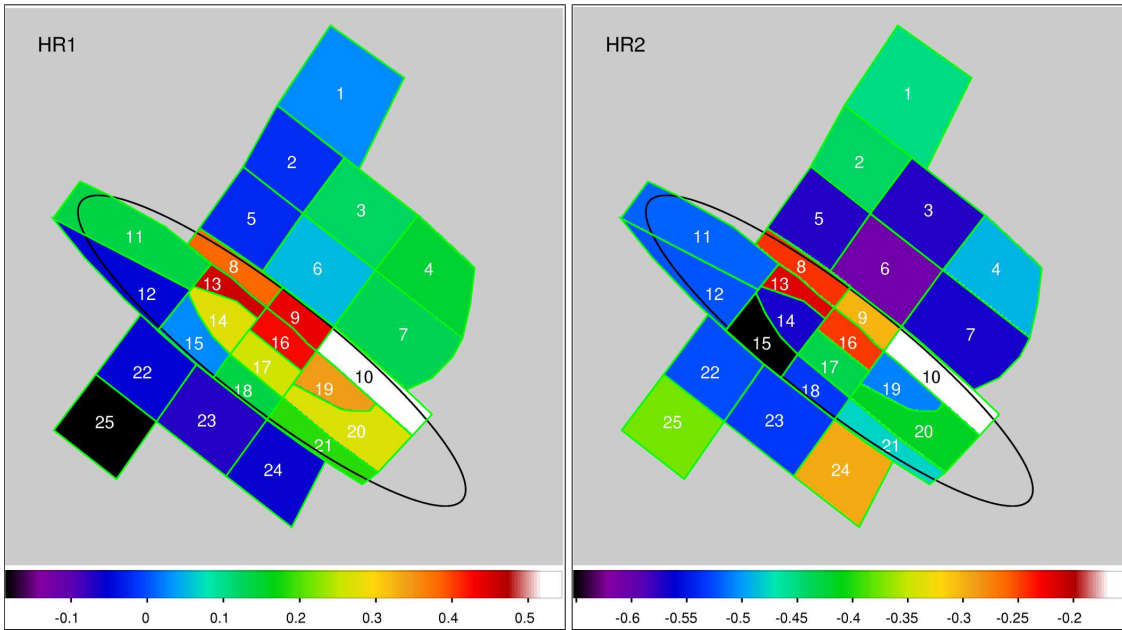
Figure 4.5: Hardness ratio maps: The map was binned to the same regions as in Fig. 4.4. The higher the index, the harder the spectrum. The background colour corresponds to an artificially set value. We also show the inclination corrected optical D_{25} ellipse. *(left):* HR1=(B$_2$-B$_1$)/(B$_2$+B$_1$), where B$_1$ and B$_2$ are the count rates in the energy bands 0.2–0.5 keV and 0.5–1.0 keV, respectively. *(right):* HR2=(B$_3$-B$_2$)/(B$_3$+B$_2$), where B$_2$ and B$_3$ are the count rates in the energy bands 0.5–1.0 keV and 1.0–2.0 keV, respectively.

4.2.2 Halo diffuse emission

The halo shows emission only below $\sim$1 keV. Its projected maximum extent is $\sim$9.0 kpc to the northwest, and $\sim$6.3 kpc to the southeast, perpendicular to the major axis. The general shape resembles a horn structure. This was already seen with *ROSAT* (e.g. Pietsch et al. 2000), and *Chandra* (e.g. Strickland et al. 2002). In the northwestern halo, the EPIC PN images only show the eastern horn. In the southeastern halo, both the eastern and the western horn are visible in the energies between 0.2 and 0.5 keV. At higher energies, the western horn is not visible.

On smaller scales the halo emission seems not to be uniformly distributed. It shows a filamentary structure, as was seen before in the *ROSAT* data. One notable feature is a brighter knot, which coincides with the nuclear outflow axis in the northwestern halo at a height of about 3.5 kpc above the disc. It is bright in energies between 0.2 and 1.0 keV and appears yellow in the false-colour image (Fig. 4.3). We checked whether any of the detected structures coincide with chip gaps of the detector, and could therefore be artificial, but no correlation was found.
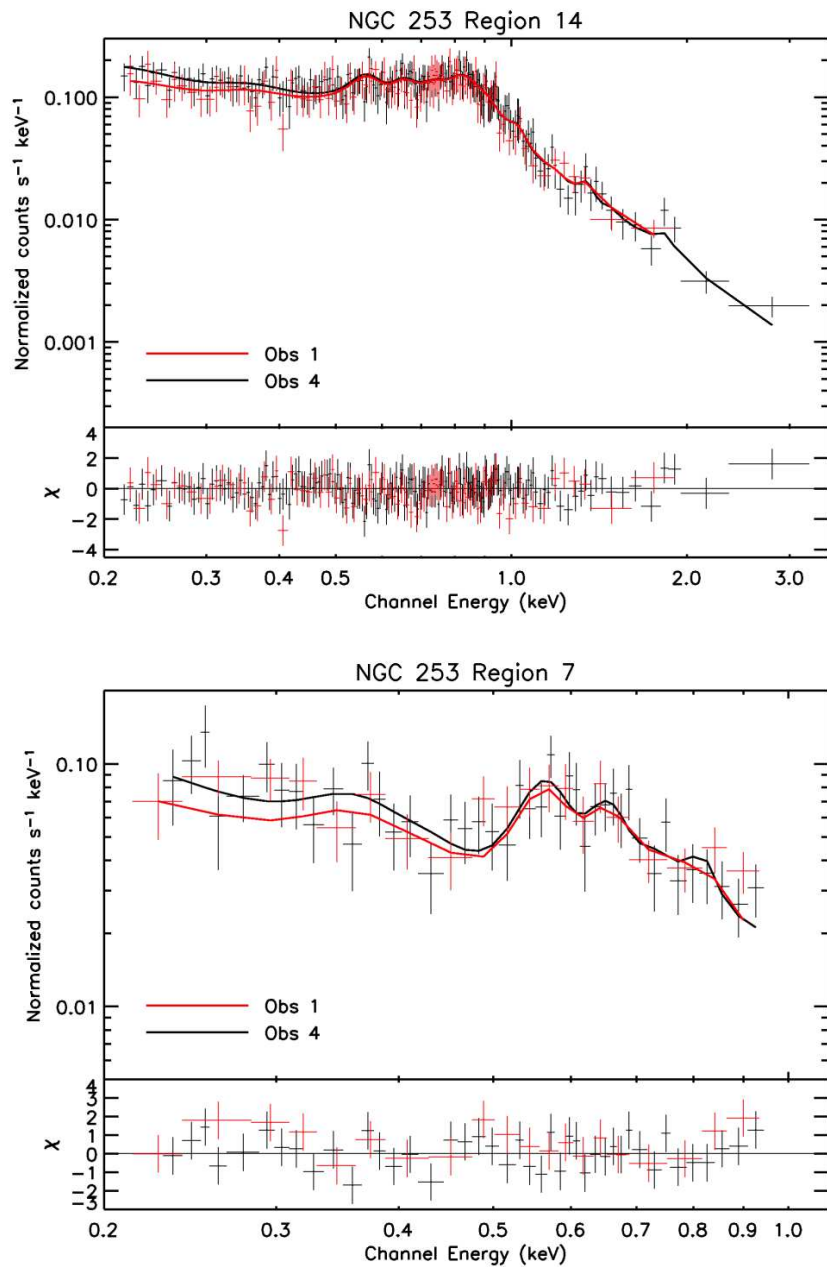
Figure 4.6: Representative spectra of a region in the disc (*top*, region 14) and of a region in the halo (*bottom*, region 7). The red and the black data points and model fits are from observations 1 and 4, respectively (see Table 2.1). The lower panel shows the residuals of the fits.

The spectral properties in different regions in the halo are summarised in Table 4.1. To fit the spectra, we applied the same approach as for the disc. Again, simple models cannot describe the spectra. A model with two thin thermal plasmas gave a good fit in all regions in the halo. Unlike in the disc, no power law component was necessary in addition to the thermal components.

The southeastern halo is softer than the northwestern halo, which results in redder colours in the southeastern halo in the EPIC PN false-colour image (Fig. 4.3), and also in lower values in HR1. A fit to the spectrum of the whole northwestern halo gave temperatures of 0.10 ± 0.01 and $0.33^{+0.02}_{-0.01}$ keV. The spectrum in the southeastern halo is similar, with temperatures of 0.09 ± 0.02 and $0.29^{+0.03}_{-0.04}$ keV. The difference in hardness is because the two plasma components contribute different amounts. Compared to the normalisation of the hotter plasma, the normalisation of the cooler plasma is about 1.5 times stronger in the southeastern halo, with respect to the northwestern halo.

The good statistics of the EPIC PN data allowed a further subdivision of the halo into smaller regions. A representative example (region 7) of one of these halo spectra is shown in Fig. 4.6. The oxygen lines at 0.57 keV (O VII) and 0.65 keV (O VIII) are prominent. Also visible is the iron line at $\sim$0.8 keV (Fe XVII).

The halo is not uniform in its spectral properties on smaller scales. The northwestern halo is softer in the east than in the west, while the southeastern halo is softer further away from the disc (see HR1 map in Fig. 4.5). Additionally the emission hardens along the direction of the northwestern outflow (regions 3 & 6). However, the significance of this difference is only 1.9 σ.

The total intrinsic luminosity for the diffuse emission, corrected for the area of the removed point sources, in the northwestern halo is 8.4×10^{38} erg s^{-1} (0.2–1.5 keV), compared to 2.1×10^{38} erg s^{-1} in the southeastern halo. To calculate electron densities, we assumed a volume for the emitting region. We modeled the northwestern halo with a cylinder with a radius of 4.3 kpc and a height of 4.2 kpc, plus a cylindrical segment with a height of 4.2 kpc, a radius of 4.3 kpc and a width in the southeast-northwest direction of 3.0 kpc (to model region 1). This gives a volume of 298 kpc^3 or 8.7×10^{66} cm^3. For the southeastern halo we assumed a cylinder with a radius of 3.5 kpc and a height of 2.0 kpc, plus a cylindrical segment with a height of 2.0 kpc, a radius of 3.5 kpc and a width in the southeast-northwest direction of 3.0 kpc (region 25), resulting in a volume of 113 kpc^3 or 3.3×10^{66} cm^3. To calculate densities and the total mass in the emission regions, we corrected the volumes for the cut-out point sources. Using the emission measure of the fit (cf. the documentation of the apec model in XSPEC), the resulting densities are $3.2\,\eta^{-0.5} \times 10^{-3}$ cm^{-3} and $4.7\,\eta^{-0.5} \times 10^{-3}$ cm^{-3} for the northwestern and southeastern halo, respectively. η is the volume filling factor ($\eta \leq 1$). With solar abundances from Wilms et al. (2000), this implies total masses of $3.3\,\eta^{-0.5} \times 10^7$ M$_\odot$

49

and $1.8\,\eta^{-0.5} \times 10^7$ M$_\odot$ for the northwestern and southeastern halo, respectively.

Table 4.1: Spectral fits (multi-temperature thermal plasma, plus power law component in the disc) and hardness ratios in the extraction regions.

Region	χ^2_ν (χ^2/ν)	kT (keV)	norm (10^{-5})	N_H (10^{22} cm^{-2})	kT (kev)	norm (10^{-5})	Γ	norm (10^{-5})	HR1	HR2
1	1.0 (21.1/21.0)	$0.10^{+0.02}_{-0.02}$	$19.4^{+8.5}_{-8.3}$	...	$0.35^{+0.06}_{-0.05}$	$5.6^{+1.6}_{-1.5}$	...	...	0.03 ± 0.04	-0.45 ± 0.03
2	0.8 (14.6/18.0)	$0.10^{+0.03}_{-0.02}$	$8.3^{+4.2}_{-3.8}$	...	$0.32^{+0.06}_{-0.05}$	$3.0^{+1.0}_{-0.9}$	...	...	-0.02 ± 0.04	-0.44 ± 0.04
3	0.9 (35.3/39.0)	$0.09^{+0.01}_{-0.02}$	$11.6^{+6.0}_{-5.0}$	...	$0.34^{+0.05}_{-0.03}$	$4.6^{+0.9}_{-0.9}$	...	...	0.12 ± 0.03	-0.57 ± 0.02
4	0.7 (16.5/25.0)	$0.11^{+0.04}_{-0.03}$	$5.7^{+3.9}_{-2.9}$	...	$0.33^{+0.07}_{-0.04}$	$3.3^{+0.9}_{-0.9}$	...	...	0.15 ± 0.04	-0.49 ± 0.03
5	0.8 (31.1/41.0)	$0.10^{+0.02}_{-0.02}$	$11.5^{+4.1}_{-2.7}$	...	$0.30^{+0.04}_{-0.04}$	$3.4^{+0.6}_{-0.9}$	...	...	-0.02 ± 0.03	-0.57 ± 0.02
6	0.9 (82.5/90.0)	$0.10^{+0.01}_{-0.01}$	$15.4^{+3.3}_{-4.1}$	...	$0.32^{+0.03}_{-0.02}$	$6.0^{+0.9}_{-0.8}$	...	...	0.05 ± 0.02	-0.61 ± 0.03
7	0.9 (52.0/59.0)	$0.11^{+0.02}_{-0.03}$	$8.2^{+3.7}_{-2.8}$	...	$0.31^{+0.03}_{-0.03}$	$5.0^{+0.9}_{-1.1}$	...	...	0.13 ± 0.03	-0.57 ± 0.02
8	...	...	...	...	...	...	...	...	0.38 ± 0.04	-0.24 ± 0.04
9	0.8 (36.4/47.0)	$0.17^{+0.08}_{-0.07}$	$1.1^{+1.2}_{-0.9}$	$0.496^{+0.391}_{-0.169}$	$0.32^{+0.08}_{-0.07}$	$9.2^{+4.7}_{-4.9}$	$1.12^{+0.54}_{-0.43}$	$0.9^{+0.4}_{-0.6}$	0.44 ± 0.04	-0.30 ± 0.03
10	...	...	...	...	...	...	...	...	0.55 ± 0.06	-0.15 ± 0.04
11	0.6 (47.0/78.0)	$0.18^{+0.05}_{-0.04}$	$3.4^{+1.4}_{-1.3}$	...	$0.58^{+0.16}_{-0.18}$	$1.9^{+0.8}_{-0.8}$	$2.54^{+0.53}_{-0.76}$	$1.2^{+0.8}_{-1.2}$	0.14 ± 0.03	-0.52 ± 0.02
12	1.4 (43.3/32.0)	$0.07^{+0.01}_{-0.01}$	$17.2^{+12.0}_{-9.6}$	...	$0.25^{+0.04}_{-0.03}$	$2.7^{+0.6}_{-0.6}$	...	...	-0.05 ± 0.04	-0.52 ± 0.03
13	0.8 (41.1/53.0)	$0.30^{+0.07}_{-0.06}$	$1.9^{+0.7}_{-1.0}$	$0.892^{+1.095}_{-0.408}$	$0.77^{+0.91}_{-0.45}$	$4.2^{+4.8}_{-3.8}$	$0.67^{+0.78}_{-0.67}$	$0.7^{+0.7}_{-0.6}$	0.46 ± 0.04	-0.22 ± 0.04
14	0.5 (149.0/275.0)	$0.20^{+0.05}_{-0.05}$	$4.3^{+1.0}_{-1.6}$	...	$0.59^{+0.06}_{-0.05}$	$5.7^{+1.1}_{-1.6}$	$2.12^{+0.23}_{-0.31}$	$2.2^{+0.6}_{-0.5}$	0.27 ± 0.02	-0.57 ± 0.02
15	0.7 (80.2/116.0)	$0.20^{+0.05}_{-0.06}$	$2.8^{+0.9}_{-1.3}$	...	$0.59^{+0.15}_{-0.15}$	$1.6^{+0.9}_{-1.4}$	$3.13^{+0.31}_{-0.32}$	$1.0^{+0.5}_{-0.4}$	0.03 ± 0.02	-0.65 ± 0.02
16 (NW outflow)	0.8 (126.1/150.0)	$0.25^{+0.08}_{-0.07}$	$1.8^{+2.1}_{-1.0}$	$0.542^{+0.239}_{-0.179}$	$0.59^{+0.11}_{-0.12}$	$9.1^{+3.7}_{-5.2}$	$1.38^{+0.19}_{-0.18}$	$2.0^{+0.4}_{-0.5}$	0.43 ± 0.02	-0.24 ± 0.02
17 (Centre)	0.8 (187.1/249.0)	$0.24^{+0.06}_{-0.04}$	$2.6^{+1.6}_{-1.4}$	...	$0.58^{+0.08}_{-0.12}$	$2.8^{+1.2}_{-1.1}$	$1.73^{+0.16}_{-0.11}$	$3.3^{+0.5}_{-0.6}$	0.26 ± 0.02	-0.43 ± 0.02
18 (SE outflow)	0.5 (82.1/152.0)	$0.24^{+0.04}_{-0.04}$	$2.9^{+1.2}_{-1.3}$	...	$0.66^{+0.19}_{-0.22}$	$1.2^{+1.0}_{-0.8}$	$2.28^{+0.27}_{-0.33}$	$1.8^{+0.5}_{-0.5}$	0.14 ± 0.02	-0.53 ± 0.02
19	0.7 (84.5/114.0)	$0.19^{+0.05}_{-0.05}$	$2.7^{+0.8}_{-1.0}$	...	$0.59^{+0.10}_{-0.11}$	$2.4^{+0.8}_{-0.9}$	$1.09^{+0.55}_{-0.32}$	$1.1^{+0.5}_{-0.8}$	0.34 ± 0.03	-0.51 ± 0.02
20	1.0 (73.7/77.0)	$0.21^{+0.05}_{-0.05}$	$3.0^{+1.1}_{-1.8}$	...	$0.57^{+0.16}_{-0.47}$	$1.7^{+0.8}_{-1.6}$	$1.51^{+0.36}_{-0.28}$	$2.2^{+0.7}_{-0.7}$	0.27 ± 0.03	-0.42 ± 0.03
21	0.8 (32.3/39.0)	$0.20^{+0.07}_{-0.07}$	$1.7^{+0.7}_{-1.1}$	...	...	...	$1.39^{+0.64}_{-0.76}$	$2.1^{+0.8}_{-0.7}$	0.19 ± 0.04	-0.48 ± 0.02
22	0.9 (45.3/48.0)	$0.10^{+0.02}_{-0.02}$	$8.9^{+2.3}_{-2.4}$	...	$0.32^{+0.06}_{-0.05}$	$1.9^{+0.5}_{-0.8}$	...	...	-0.05 ± 0.04	-0.53 ± 0.03
23	0.9 (54.0/62.0)	$0.09^{+0.02}_{-0.01}$	$13.5^{+3.4}_{-3.9}$	...	$0.30^{+0.04}_{-0.03}$	$3.1^{+0.8}_{-0.7}$	...	...	-0.07 ± 0.03	-0.53 ± 0.03
24	...	...	...	...	...	...	...	...	-0.06 ± 0.05	-0.30 ± 0.04
23+24	1.1 (82.5/75.0)	$0.07^{+0.01}_{-0.01}$	$46.7^{+20.6}_{-15.2}$	...	$0.26^{+0.03}_{-0.02}$	$6.2^{+1.0}_{-1.0}$	...	...	-0.07 ± 0.03	-0.45 ± 0.02
25	0.4 (8.5/20.0)	$0.09^{+0.03}_{-0.03}$	$8.5^{+3.3}_{-4.1}$	...	$0.24^{+0.08}_{-0.06}$	$1.3^{+1.2}_{-0.8}$	...	...	-0.19 ± 0.05	-0.37 ± 0.04
1...7 (NW halo)	0.8 (209.4/261.0)	$0.10^{+0.01}_{-0.01}$	$97.5^{+11.6}_{-12.4}$	...	$0.33^{+0.02}_{-0.01}$	$34.7^{+2.7}_{-3.6}$	...	...	0.04 ± 0.01	-0.55 ± 0.01
22...25 (SE halo)	1.1 (82.4/76.0)	$0.09^{+0.02}_{-0.02}$	$34.9^{+9.2}_{-5.8}$	...	$0.29^{+0.03}_{-0.04}$	$7.5^{+2.0}_{-1.8}$	...	...	-0.08 ± 0.02	-0.46 ± 0.02
2...4	1.0 (97.8/99.0)	$0.10^{+0.01}_{-0.01}$	$26.6^{+8.6}_{-7.8}$	...	$0.33^{+0.03}_{-0.03}$	$11.1^{+1.8}_{-1.6}$	...	...	0.09 ± 0.02	-0.51 ± 0.02
5...7	0.9 (157.8/168.0)	$0.10^{+0.01}_{-0.01}$	$36.8^{+6.1}_{-7.1}$	...	$0.32^{+0.02}_{-0.02}$	$14.8^{+1.7}_{-1.9}$	...	...	0.06 ± 0.02	-0.59 ± 0.01
22...24	1.1 (91.1/81.0)	$0.09^{+0.02}_{-0.02}$	$29.0^{+6.7}_{-7.6}$	...	$0.29^{+0.03}_{-0.03}$	$6.7^{+1.7}_{-1.4}$	...	...	-0.06 ± 0.02	-0.48 ± 0.02

NOTE: All errors are 90% confidence for a number of interesting parameters equal to the number of free parameters in the model (3, 4, 5, 6, 7, or 9 free parameters depending on the model). Thin thermal plasma models are apec, absorbtion models are tbabs. All models have a fixed foreground absorption of 1.3×10^{20} cm^{-2}. For region 8, 10 and 24 no spectral fit was attempted due to low statistics. The hardness ratios in these regions do give meaningfull values though.

Table 4.2: Spectral fits in the halo extraction regions with a thin thermal plasma plus power law component, as opposed to a multi-temperature thermal plasma model in Table 4.1.

Region	χ^2_ν (χ^2/ν)	kT (keV)	norm (10^{-5})	Γ	norm (10^{-5})
1	1.1 (22.3/21.0)	$0.19^{+0.21}_{-0.19}$	$1.3^{+2.9}_{-1.3}$	$1.90^{+0.64}_{-0.61}$	$5.6^{+1.8}_{-2.0}$
2	0.7 (12.5/18.0)	$0.24^{+0.08}_{-0.06}$	$2.0^{+1.5}_{-1.4}$	$2.48^{+0.60}_{-0.86}$	$1.5^{+0.9}_{-1.0}$
3	1.1 (41.2/39.0)	$0.32^{+0.06}_{-0.04}$	$3.8^{+1.4}_{-1.1}$	$3.09^{+0.34}_{-0.57}$	$0.9^{+0.5}_{-0.7}$
4	1.0 (24.4/25.0)	$0.29^{+0.05}_{-0.05}$	$3.1^{+1.3}_{-1.3}$	$2.87^{+0.56}_{-1.11}$	$0.7^{+0.6}_{-0.7}$
5	0.8 (32.9/41.0)	$0.21^{+0.04}_{-0.04}$	$2.5^{+1.2}_{-1.2}$	$2.60^{+0.43}_{-0.53}$	$1.5^{+0.6}_{-0.5}$
6	0.8 (74.9/90.0)	$0.25^{+0.03}_{-0.03}$	$4.2^{+1.4}_{-1.5}$	$2.41^{+0.30}_{-0.32}$	$2.6^{+0.6}_{-0.7}$
7	0.7 (41.7/59.0)	$0.22^{+0.04}_{-0.04}$	$2.9^{+1.8}_{-1.5}$	$1.74^{+0.47}_{-0.62}$	$3.5^{+1.1}_{-1.5}$
22	0.9 (44.0/48.0)	$0.16^{+0.06}_{-0.05}$	$1.8^{+1.3}_{-1.2}$	$2.40^{+0.64}_{-0.66}$	$1.4^{+0.4}_{-0.4}$
23	0.9 (52.8/62.0)	$0.24^{+0.03}_{-0.03}$	$2.7^{+1.0}_{-0.9}$	$3.25^{+0.35}_{-0.37}$	$0.8^{+0.3}_{-0.3}$
25	0.5 (10.4/20.0)	$0.18^{+0.05}_{-0.05}$	$1.9^{+2.0}_{-1.0}$	$3.80^{+0.66}_{-0.84}$	$0.3^{+0.2}_{-0.3}$
23+24	1.3 (98.6/75.0)	$0.22^{+0.07}_{-0.08}$	$0.9^{+4.7}_{-0.5}$	$2.49^{+0.28}_{-0.35}$	$3.5^{+0.3}_{-1.9}$
1…7 (NW halo)	0.8 (201.6/261.0)	$0.26^{+0.01}_{-0.01}$	$29.1^{+3.9}_{-4.4}$	$2.84^{+0.16}_{-0.16}$	$10.2^{+1.5}_{-1.3}$
22…25 (SE halo)	1.1 (81.2/76.0)	$0.21^{+0.04}_{-0.03}$	$6.2^{+2.6}_{-2.4}$	$3.03^{+0.37}_{-0.43}$	$2.7^{+0.8}_{-0.8}$
2…4	1.0 (101.6/99.0)	$0.28^{+0.04}_{-0.04}$	$7.5^{+2.9}_{-2.5}$	$2.46^{+0.29}_{-0.48}$	$4.5^{+1.4}_{-1.5}$
5…7	0.9 (151.8/168.0)	$0.25^{+0.02}_{-0.02}$	$12.4^{+2.4}_{-2.6}$	$2.65^{+0.23}_{-0.24}$	$4.8^{+1.0}_{-1.1}$
22…24	1.2 (93.9/81.0)	$0.23^{+0.03}_{-0.03}$	$5.7^{+2.0}_{-1.8}$	$3.14^{+0.33}_{-0.37}$	$1.9^{+0.6}_{-0.6}$

NOTE: All errors are 90% confidence for a number of interesting parameters equal to the number of free parameters in the model. Thin thermal plasma models are apec. All models have a fixed foreground absorption of 1.3×10^{20} cm^{-2}.

4.3   Discussion

4.3.1   The extent of the diffuse emission of NGC 253

Extended emission from the soft northwestern halo was first reported from *Einstein* observations (Fabbiano 1988). Later, observations with *ROSAT* also discovered the southeastern halo in X-rays (e.g. Pietsch et al. 2000). The *ROSAT* images in the soft band trace the emission in the outer halo to projected distances of up to 9 kpc, both in the northwest and the southeast direction. With *XMM-Newton*, the emission is detected out to 9.0 kpc to the northwest and 6.3 kpc to the southeast. This difference in the southeastern halo can be explained by the high *ROSAT* sensitivity extending down to 0.1 keV. The useful *XMM-Newton* EPIC PN range is limited to 0.2 keV. This makes a big difference as there are many strong lines from O IV, Ne VIII, Mg IX, Mg X, Si IX, and Si X in the energy band between 0.1 and 0.2 keV. For a thermal plasma at a temperature of ∼0.1 keV, these lines are even stronger than the O VII and O VIII lines, and about 60% of the total flux in the energy band from 0.1 to 2.0 keV originates from lines below 0.2 keV. The southeastern halo shows softer emission than the northwestern halo, therefore, the effect is strongest in the southeastern halo.

Also in the disc the extent of the emission is different. The *ROSAT* images trace the soft emission ∼6.8 kpc towards the northeast and ∼5.3 kpc towards the southwest. With *XMM-Newton*, the disc emission has an extent of ∼7.2 kpc and ∼6.3 kpc to the northeast and southwest, respectively. The disc spectra are harder than the halo spectra, and therefore the higher *XMM-Newton* sensitivity at energies >0.4 keV comes into play.

4.3.2   Is the diffuse emission in the disc really from hot interstellar gas?

The cumulative emission of a large population of weak stellar-type X-ray sources can mimic the characteristics of a hot interstellar gas component. This was first discovered in the Milky Way's ridge X-ray emission (e.g. Revnivtsev et al. 2006), who found evidence that the bulk of the Galactic ridge X-ray emission is composed of weak X-ray sources, mostly cataclysmic variables and coronally active stars in binary systems, with a luminosity of most of these sources of less than 10^{31} erg s^{-1}. Also in other galaxies, Revnivtsev et al. (2007) found that the apparently diffuse emission is consistent with the emission from an old stellar population like in the Milky Way.

Can this also explain the extended X-ray emission in the disc of NGC 253? Following the method by Revnivtsev et al. (2007), we used K-band observations, to infer the emissivity of the diffuse X-ray component per unit stellar mass. We derived the near-infrared luminosity and stellar mass of NGC 253, using the total K-band magnitude of 3.772 (Jarrett et al. 2003), the distance modulus of 27.06, corrected for interstellar extinction of 0.007 (Schlegel et al.
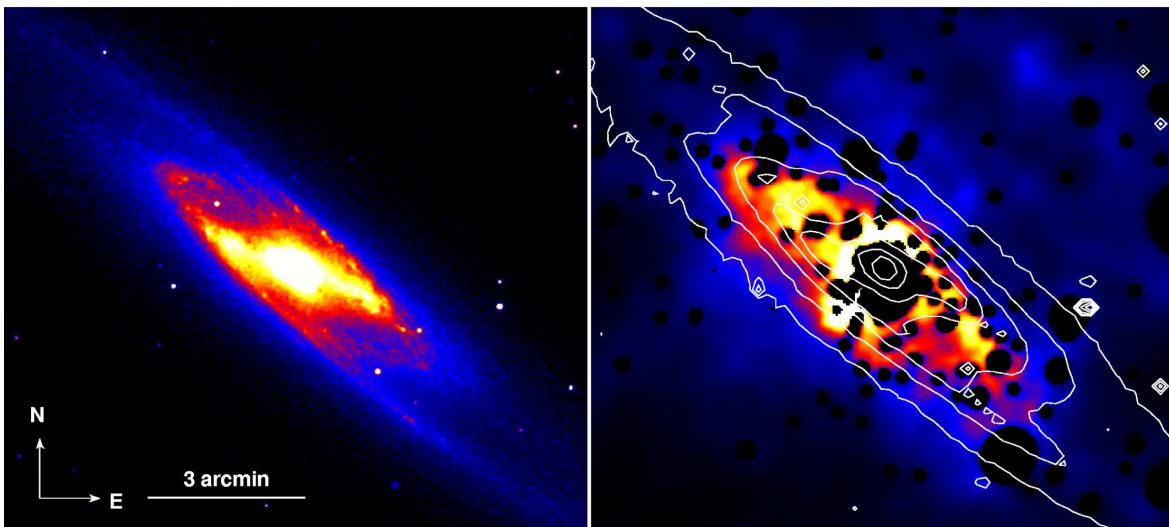
Figure 4.7: Comparison between the K-band (left, 2MASS, Jarrett et al. 2003) and X-ray (right) morphology. The white contours overplotted on the X-ray image represent the K-band brightness levels. Both images are on a linear colour scale, and on the same spatial scale as indicated in the K-band image.

1998), and the colour-dependent K-band mass-to-light ratio from (Bell & de Jong 2001, $\log(M_*/L_{\rm K}) = -0.692 + 0.652 \times (B - V)$), with $(B - V) = -0.16$ (Comerón et al. 2003). This yielded a total K-band luminosity $L_{\rm K} = 1.6 \times 10^{11}\ L_\odot$ and a total stellar mass $M_* = 2.6 \times 10^{10}\ M_\odot$. With a X-ray luminosity of NGC 253 of 2.0×10^{39} erg s^{-1} (0.5–10 keV), the emissivity of the diffuse X-ray component per unit stellar mass then resulted in

$$\frac{L_{0.5-10\ \rm keV}}{M_*} = 7.6^{+0.9}_{-0.3}\,(\pm 2.3) \times 10^{28}\ \text{erg s}^{-1}\ M_\odot^{-1}.$$

The errors are statistical errors on the measured X-ray flux. Additionally, we assumed an uncertainty of ~30% (given in parentheses), which might be associated with the $L_{\rm K}$ to M_* conversion (Bell et al. 2003). The emissivity of NGC 253 should only be considered a lower limit. We cut out a quite large region in the centre of NGC 253 and corrected for this by filling the hole with the average flux of the disc. Therefore, the obtained X-ray luminosity as well as the emissivity are probably too small.

From the luminosity and other properties of the Galactic ridge X-ray emission (e.g. Revnivtsev et al. 2006) and from direct measurements of the luminosity function of sources in the solar neighbourhood (Sazonov et al. 2006), the combined 0.5–10 keV emissivity of cataclysmic variables and coronally active stars has been estimated as $L_{\rm X}/M_* \sim 1.2 \pm 0.3 \times 10^{28}$ erg s^{-1} $M_\odot^{-1}$. The value derived for NGC 253 is larger than the value for the Milky Way, indicating the presence of a hot gaseous component.

An even stronger argument is the following: if the diffuse X-ray emission is produced by an old stellar population, then their morphologies should be similar. A comparison of the X-ray emission with the 2MASS K-band image (Jarrett et al. 2003) is shown in Fig. 4.7. We found that the X-ray morphology does not match the K-band morphology, therefore the diffuse emission is indeed not simply due to an old stellar population, but has to have a truly diffuse component.

4.3.3 Spectral fits and variations in the halo

As it was mentioned already in earlier publications, there is an ambiguity in the spectral fits between a pure multi-temperature thermal plasma model and a combination of thermal plasmas plus a power law component (e.g. Dahlem et al. 2000; Strickland et al. 2002). This ambiguity in the halo emission still exists with the *XMM-Newton* data. Fits to the halo spectra with a thermal plasma plus a power law model (see Table 4.2) resulted in similar χ^2_ν, as for a multi-temperature thermal plasma model. A power law component from point sources could be excluded, since we were careful to remove any point source contribution. Another source for non-thermal emission could be synchrotron emission from cosmic ray electrons that are advected with the superwind or are accelerated locally in internal wind shocks. A comparison of the X-ray emission to the 330 MHz and 1.4 GHz radio emission (Carilli et al. 1992) showed that the radio emission is more extended, and does not show the horn structure that we see in X-rays. Because of this inequality, we prefer the multi-temperature thermal plasma model for the X-ray halo emission at the moment. A currently ongoing analysis with non-equilibrium models (e.g. Breitschwerdt & Schmutzler 1999) might also be able to explain the observations.

The northwestern halo shows significant hardness variations in HR1, as opposed to the findings by Strickland et al. (2002). We checked if this can be caused by a different energy band selection, but the result is independent whether we use the bands from Strickland et al. (2002) (0.3–0.6 keV and 0.6–1.0 keV) or our own. These hardness variations might also be a sign of non-equilibrium ionisation (NEI) X-ray emission.

4.3.4 Temperatures, abundances and column densities

The X-ray emission from NGC 253 has been observed before with several other X-ray observatories. Especially the early observatories did not allow to separate the point sources from the diffuse emission since the point spread function was quite large. Hence, only a combined fit of the emission from the halo, the disc, and the nuclear region was possible. Temperatures of multi-temperature models ranged between 0.1 and 0.3 keV for the low, and between 0.6 and 0.7 keV for the high temperature component (Dahlem et al. 1998; Weaver

et al. 2000; Dahlem et al. 2000). Reported abundances were mostly highly subsolar and therefore unphysical for a supposedly metal enriched starburst galaxy plasma.

Only the X-ray observatories like *XMM-Newton*, *Chandra*, and to some degree *ROSAT* allow us to separate the halo from the disc emission and to remove contribution by point sources via a spatial selection. From *ROSAT* data, Pietsch et al. (2000) inferred a foreground absorbed two-temperature thermal model with temperatures of 0.13 and 0.62 keV for the northwestern halo emission. No highly subsolar abundances were required. The disc emission could be explained by a 0.7 keV thermal plasma and an additional thermal plasma (kT=0.2 keV) in front of the disc coming from a coronal component.

The first *XMM-Newton* results by Pietsch et al. (2001) required a two-component model for the disc emission with temperatures of 0.13 and 0.4 keV plus residual harder emission, possibly from unresolved point sources. For the nuclear region three temperatures were needed (0.6, 0.9, and 6 keV). Both models used solar abundances. No analysis of the halo emission was presented in their paper.

The best spatial resolution is provided by the *Chandra* observatory. Results on the diffuse disc and halo emission were first published by Strickland et al. (2002). For the halo emission they needed a multi-temperature model (apec) with at least two temperatures of 0.24 and 0.71 keV (the latter with quite large errors) and with a foreground absorption of 5.3×10^{20} cm^{-2}. A power law ($\Gamma = 3.3$) plus a thermal plasma (kT=0.24 keV) gave a similarly good fit. A combination of other thermal models (mekal) or non-equilibrium models (vnei) did not result in better fits. The diffuse emission from the disc was fitted with the same models, however, the temperatures were lower than in the halo, with 0.17 and 0.56 keV, respectively. The foreground absorption yields 4.7×10^{20} cm^{-2}. In all cases unphysically sub-solar abundances had to be assumed.

The temperature values for the halo emission, as found by our analysis, are lower than the ones from previous observations. Our soft component is about 0.10 keV, which is still compatible with the *ROSAT* results. However, the hard component is only ∼0.32 keV for the northwestern halo and ∼0.29 keV for the southeastern halo. A higher temperature was not necessary in any of our fits. A possible explanation could be the way the spectra were background subtracted. We used a sophisticated method (see App. D) that uses the local background at the border of the field of view, where no emission from NGC 253 is expected, while other authors used e.g. blank-sky observations (Strickland et al. 2002). Using a background from different times and different fields on the sky can lead to systematic effects in the background substraction. A background region with a higher contribution of the local bubble could, for example, lead to an over-correction, especially at very soft energies (<0.5 keV).

In the disc we found temperatures between 0.1 and 0.3 keV and between 0.3 and 0.8 keV,

for the soft and the hard component, respectively. This is consistent with earlier results.

We also tried to constrain the metal abundances in our fits. However the errors on the obtained values are so large, that we are not able to give well constrained abundances (north-western halo: $Z = 0.3^{+4.7}_{-0.2}\ Z_\odot$, southeastern halo: $Z = 0.4^{+4.6}_{-0.3}\ Z_\odot$, disc: $Z = 1.0^{+0.9}_{-0.7}\ Z_\odot$). Since we do not expect highly subsolar abundances in an environment which is enriched with metals from the starburst via the superwind and galactic fountains, we fixed the abundances in our analysis to solar. This is very well consistent with the above values. A reason for the low abundances, found with different instruments, could be that due to a lower spatial resolution and or/and sensitivity more point sources contribute to the final spectrum, increasing the continuum flux. The ratio of line emission to continuum flux is therefore decreased, which mimics the spectral shape of a plasma with low metal abundances. A similar effect can be achieved when a NEI spectrum is fitted with CIE models. Also, a too simplistic model could be the reason, combining regions with different temperatures.

In the disc, three of the regions required an extra absorption component in the spectral model. The additional column densities range between 0.5×10^{22} cm^{-2} and 0.9×10^{22} cm^{-2}. Direct radio measurements of the H I column density showed lower values than we derived from the X-ray data. An interpolation of the H I maps by Puche et al. (1991) and Koribalski et al. (1995) resulted in ~ 2.4, 3.9, and 3.4×10^{21} cm^{-2} for regions 9, 13, and 16, respectively. However, the H I value for the region including the nucleus of NGC 253 (region 16) is affected by H I absorption, so the resulting column density can only be considered as a lower limit. Additional absorption is expected from molecular hydrogen. Mauersberger et al. (1995) derived the H$_2$ column density in the direction of the nucleus of NGC 253 to 3.7×10^{23} cm^{-2}. Taking this value as an upper limit for the column density in the disc regions around the nucleus, the column densities derived from X-ray spectra are within the limits from radio observations.

4.3.5   X-ray versus UV morphology

Fig. 4.8 shows the X-ray contours from the energy band 0.2–0.5 keV overplotted on a two-colour UV image, taken with the GALEX observatory (Galaxy Evolution Explorer, a UV space telescope) on 2003 October 13. For the northwestern halo there is quite a good agreement between the FUV and X-ray emission regions. The FUV emission traces the western horn to a distance of ~ 7.5 kpc above the disc, as well as the broad base emission in soft X-rays quite well. In the southeastern halo, again, the UV and the soft X-ray emission show the western horn structure, where the UV horn extends to about 7 kpc away from the disc. However, the FUV horn is slightly offset by ~ 700 pc to the northeast with respect to the X-ray horn. Images obtained with the Optical Monitor onboard *XMM-Newton* are not sensitive
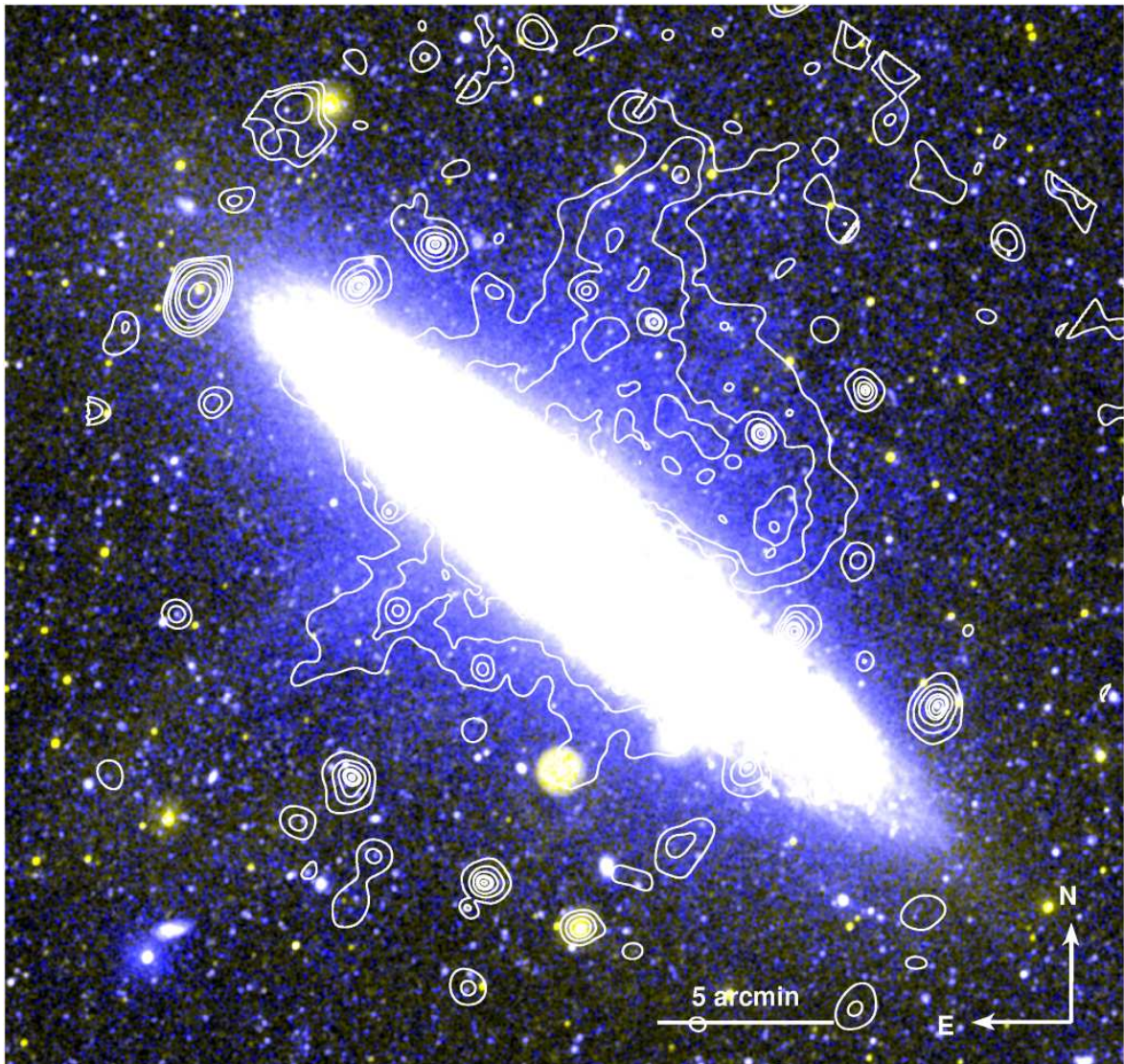
Figure 4.8: Two-colour UV image of NGC 253 with NUV (175–280 nm) in yellow and FUV (135–175 nm) in blue. The intensity was rescaled to emphasise the faint, diffuse emission. Overplotted are the 0.2–0.5 keV X-ray contours.

enough to show the extraplanar UV emission.

Hoopes et al. (2005) proposed the following model for the origin of the UV emission: Since the UV luminosities are too high to to be produced by continuum and line emission from photoionized or shock-heated gas, the UV emission could be explained by dust in the outflow that scatters the stellar continuum from the starburst into our line of sight. They also found that the UV halo emission, as seen with GALEX, correlates with the Hα emission, which could originate from gas that is photoionized by UV photons from the starburst. The UV and Hα emission would originate in the same cold regions in the halo.

How does the warm gas that is responsible for the Hα and UV emission get out into the halo? There are two possibilities: either it has already been there from the beginning in the form of a cold and maybe clumpy halo component, or it was transported by the superwind and galactic fountains from the disc out into the halo.

There are models, where it is possible to drag up clouds of cold gas into the halo (e.g. model 3 of Strickland et al. 2002). In a sheet surrounding these clouds, X-ray emission could be produced by shocks or in conductive or turbulent mixing interfaces on the cloud surface. This model would also account for the non-uniformity of the X-ray emission as seen in the *XMM-Newton* images (Fig. 4.1 and 4.3). However, the model cannot explain the displacement of the UV emission in the southeastern halo, since in the model the clouds are located within or at the inner border of the superwind.

Could the dust even survive this transport from the disc into the halo embedded in a hot plasma environment? Draine & Salpeter (1979) give the sputtering time for a spherical dust grain of radius a embedded in a plasma of hydrogen with temperatures between 10^6 and 10^9 K and the density n_H as

$$t_{\text{sput}} \sim 10^6 \left(\frac{a}{\mu m} \right) \left(\frac{n_H}{\text{cm}^{-3}} \right)^{-1} \text{yr.} \qquad (4.1)$$

For n_H between 2.5×10^{-2} cm^{-3} in the outflow close to the centre (Bauer et al. 2007b) and 3.2×10^{-3} cm^{-3} out in the northwestern halo, and a grain size of a=0.1 μm, t_{sput} varies between 4.0 and 31 Myr. So to reach a height above the disc of 7.5 kpc in less than 31 Myr, an average velocity of at least 240 km/s is required. This is well compatible with measurements of outflow velocities in different wavelengths, that range from 260 km/s (Na D absorption, Heckman et al. 2000) to about 400–600 km/s (Hα, N II, S II, and O II emission, Ulrich 1978; Demoulin & Burbidge 1970). Therefore it is quite possible that the dust survives the transport from the disc out into the halo.

Another model to explain the UV and X-ray morphology (e.g.model 5 of Strickland et al. 2002) requires a thick disc component, through which the superwind emerges into the halo. On the contact surface between the hot superwind fluid and the cold thick disc material we get a heated layer through shocks and turbulent mixing where the X-rays are

produced, surrounded on the outside by a colder layer where the UV emission originates. The thick disc component was originally created by lifting material up from the disc through the star formation activity (simulations by Rosen & Bregman 1995). This model would easily explain the UV displacement from the X-rays, however we would only get a hollow cone with X-ray emission. The latter is not what we see in the *XMM-Newton* observations. Though a mix of both models would be able to explain the observed morphology.

The magnetohydrodynamics ISM simulations of de Avillez & Breitschwerdt (2005) also shows a clumpy halo structure, characterised by turbulent mixing layers, which could explain the UV and X-ray filamentary structure. In some regions, the magnetic field forms loops surrounded by shells which may exhibit enhanced UV emission.

Chapter 5

High resolution X-ray spectroscopy and imaging of the nuclear outflow

Starburst galaxies are known to show very complex emission in X-rays. This emission originates, on the one hand, from sources that appear to be point-like sources, like X-ray binaries, supernovae, and supernova remnants. On the other hand, emission comes from the diffuse hot component of the interstellar medium, such as diffuse emission in the disc and gaseous outflows driven out of the disc by massive stellar winds and core collapse supernovae, also called superwinds. The latter phenomenon can be quite spectacular in M82 (e.g. Stevens et al. 2003) and NGC 253 (e.g. Strickland et al. 2000), for example, where these superwinds emerge from a starburst nucleus. In NGC 253, Fabbiano & Trinchieri (1984) first detected the southeastern part of this outflow in X-rays with *Einstein* and called it the "minor-axis component". With *ROSAT*, Pietsch et al. (2000) also detected the part of the outflow pointing in the opposite direction. However, the spatial resolution of *ROSAT* was not yet good enough to learn more about the morphology of this outflow. Later on, observations with *XMM-Newton* (Pietsch et al. 2001), and especially with *Chandra* (Strickland et al. 2000), showed that the outflow can be explained with a limb-brightened hollow cone structure. Temperatures of the best-fit, thin thermal plasma models are in the range 0.15-0.94 keV from *XMM-Newton* EPIC and 0.46-0.66 keV from *Chandra*. Strickland et al. (2000) conclude that the detected emission originates in the shocked region at the border of the outflow where the wind collides with interstellar medium. The wind itself, though, was thought to be too hot and too thin to be detected directly. This picture, however, disregards the possibility that the wind may be mass-loaded, entraining ambient ISM, as well as infalling material. If turbulent mixing proceeds on a time scale that is larger than the flow time within a given region, such as the base of the outflow studied here, we expect some clumpiness in the outflow, imprinted on an

overall *less dense* wind. As we show later, this is confirmed by our analysis, which shows that e.g. O VIII is not limb-brightened.

High-resolution spectra of NGC 253 and M82, taken with the *XMM-Newton* Reflection Grating Spectrometer (RGS), were first published by Pietsch et al. (2001) and Read & Stevens (2002), respectively. Both spectra show the Ly_α emission lines from Si, Mg, Ne, O, N, and their helium-like charge states. Both galaxies also show emission lines from Fe XVII and Fe XVIII, and M82 shows lines from Fe XX, Fe XXIII and Fe XXIV. In M82 the line ratios for neon, iron, and oxygen are quite different compared to NGC 253. In general the M82 spectrum appears to be hotter with temperatures in the range of $\sim$0.3–1.5 keV, with its continuum confined more to higher energies. Its X-ray flux, as well as its X-ray luminosity, in the RGS energy band (0.35–2.5 keV) is higher than for NGC 253.

However, these spectra only give a combined spectrum of the nuclear source and the outflow. Here we present an analysis where we decompose the total spectrum of NGC 253 into regions containing the nucleus and different parts of the outflow, while maintaining the high spectroscopic resolution.

The observation with Obs. id. 0110900101 could not be used for this analysis, since the pointing direction of this observation was in the northwest halo of NGC 253 with the result that the outflow was not in the field of view (FOV) of the RGS (cf. Table 2.1).

5.1 Data reduction

Before we start to describe the analysis procedures, we want to place emphasis on why it is even possible to perform the following spectroscopic analysis. First, the nuclear outflow of NGC 253 is an extended X-ray object, which can be spatially resolved by *XMM-Newton* EPIC and RGS, embedded in an even larger region of X-ray emission from point-like sources and diffuse emission in the disc and halo of the galaxy. This means the RGS data for the central regions are in principle affected by the contamination from the surrounding emission, but, as shown in Fig. 5.1, both the nucleus and the outflow in NGC 253 are significantly brighter and well above the galaxy emission, so we can only expect a minor contamination. Moreover, as we show later, we can identify and "remove" effects due to the disc emission.

Second, since the RGS is a slitless spectrometer, the spectra of all sources in the field of view are superimposed on each other on the detector. Spatial displacement of a source along the dispersion direction corresponds to a wavelength shift in the spectrum of 2.31×10^{-3} Å $arcsec^{-1}$ with respect to a not-displaced source. Since the outflow has an extent of up to $1.4'$ in the dispersion direction, the spectral resolution is limited to $\sim$0.19 Å at 15 Å. This is still considerably better than the energy resolution from CCD detectors.

Due to the superposition of all sources, other bright point sources in the FOV could

contaminate the spectrum of the outflow. However, the effective area decreases significantly for off-axis sources and even a contribution from the brightest off-axis source at the bottom of Fig. 5.2 (X21 from Pietsch et al. 2000; Tanaka et al. 2005) can be neglected. The source on the southwest edge of the outflow in region SE 1 (cf. Figs. 5.1 and 5.2), however, does affect the outflow spectrum. The spectrum of this source does not show line features (X33 in Pietsch et al. 2001), so its contribution to the RGS spectrum from this region is an increased continuum flux. This does not affect our conclusions.

5.1.1 RGS spectra

Since the dispersion direction of the RGS was approximately aligned with the major axis of the galaxy, we were able to extract spectra for different adjacent regions along the minor axis, i.e. the cross-dispersion direction, of the galaxy (see Fig. 5.2). The extent of the extraction regions are $30''$ in the cross-dispersion direction. Assuming a distance to NGC 253 of 2.58 Mpc (Puche et al. 1991) this corresponds to a width of 375 pc for the extraction regions. The events in these regions were additionally filtered with a CCD pulseheight filter to select only the $m = -1$ spectral order. The reference points for the origins of the energy scales of the spectra were set on the minor axis of the galaxy, where the outflow has its peak emission (see Fig. 5.1).

NGC 253 is an extended source and covers most of the area of the RGS detectors. To prevent contamination in the background spectra we used the task `rgsbkgmodel 1.1.5`, which computes background spectra from RGS background templates.

To increase statistics we combined the spectra of the two RGS detectors and added up the spectra from the three observations. As the position angles of *XMM-Newton* did not differ very much in these three observations, the regions from which the spectra were extracted are only slightly tilted relative to each other. A difference in position angle between observations has the effect of degrading the spatial coincidence in the extraction regions. In our case, however, position angle differences are small enough that we can neglect this error. A correction of the spectra for effective area and the combination of the spectra from different observations and instruments was done with the task `rgsfluxer`. The task's description states that the fluxed spectrum produced by `rgsfluxer` should not be used for any serious analysis of the data. If we use it in spite of this warning, we have to consider that the following effect will add to uncertainties: The task `rgsfluxer` neglects the redistribution of monochromatic response into the dispersion channels, so the intrinsic line broadening of the detector is not removed from the spectrum. As we do not determine line positions or line widths and since we integrate over the whole line including its wings to derive fluxes for individual lines, this effect does not restrict our analysis. Additionally, we are only interested
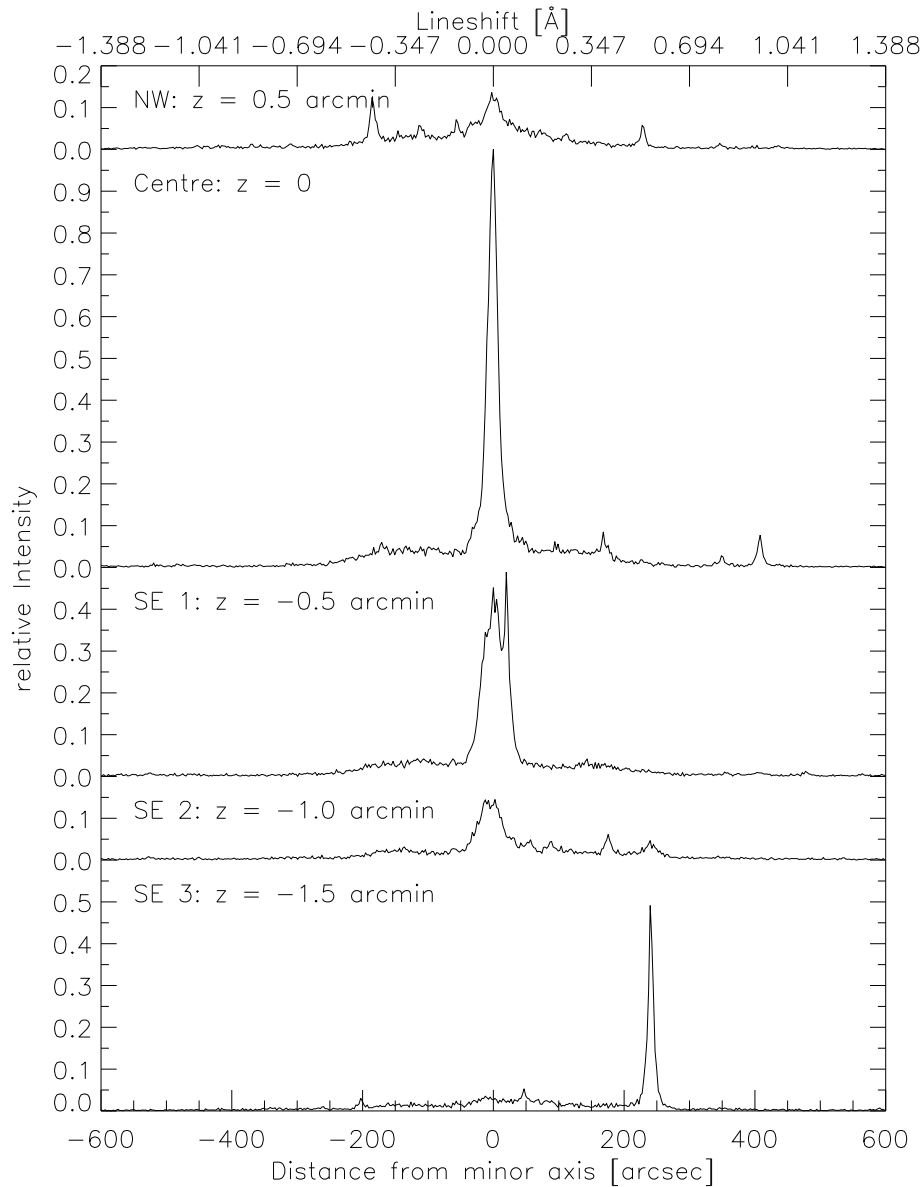
Figure 5.1: EPIC PN brightness profiles along the RGS dispersion direction of each extraction region. The strong peak at $0''$ is caused by the outflow emission. In the centre region, shown in Fig. 5.2, this is superimposed by the nuclear source of the galaxy. Point sources in the extraction regions are seen as sharp spikes in the profile. A positive distance points parallel to the major axis towards the south-west. The distance from the galactic major axis is given by the value z in the captions of the individual extraction regions.
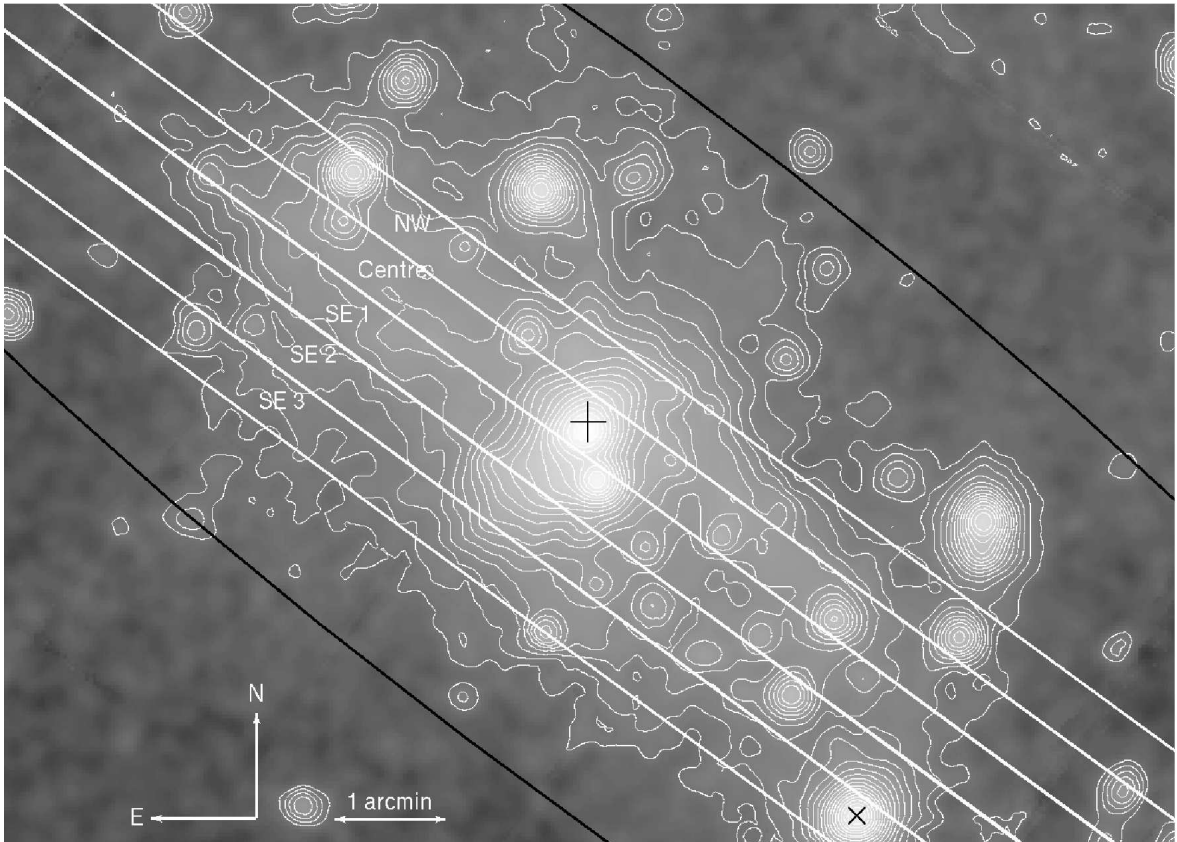
Figure 5.2: Logarithmically-scaled EPIC PN+MOS image of the central region of NGC 253 in the energy band $0.5 - 2.0$ keV. The centre of the galaxy is marked with the black cross. The D25 ellipse is overlaid in black, and brightness contours and the extraction regions for the RGS spectra are overlaid in white. The black X at the bottom of the image marks the source X21.

in relative line fluxes and not in absolute values.

To obtain acceptable statistics ($> 3\sigma$) for most of the emission lines while maintaining a high spectral resolution of $\sim$0.39 Å in the spectra we combined six channels at a time.

For the observations the dispersion direction of the spectrometers was approximately aligned along the major axis of the galaxy. Therefore the spectra for different cross-dispersion areas correspond to regions with a different distance z from the galactic plane (cf. Fig. 5.2). The spectra obtained from these regions are shown in Fig. 5.3.

5.1.2 RGS images

The RGS is a slitless spectrometer, so the whole observed target within the FOV is imaged on the detector plane, with an offset in dispersion direction for every wavelength it emits

in. This aspect can be used to extract narrow band images for various emission lines. In the cross-dispersion direction, the image in a selected emission line is directly mapped onto the detector CCD, while in the dispersion direction the observed object is compressed into a narrow region. This technique was first applied to RGS data of the supernova remnant DEM L 71 by van der Heyden et al. (2003), and with his help (private communications) we developed our own code to produce these narrow band images. The procedure is as follows. The low background eventlists are filtered for the wavelength range of the desired line and for the "banana region" in wavelength-energy-space to exclude second-order spectra and noise. By setting the wavelength range narrow enough, we made sure that no neighbouring lines would be in the extraction region. The dataset thus obtained has to be converted into spatial coordinates and to be uncompressed along the dispersion axis using the following equation as described in the SAS task `rgsangles`:

$$\Delta\beta = \frac{\sin\alpha}{\sin\beta}\Delta\phi\frac{F}{L} \tag{5.1}$$

with the change in the grating exit angle $\Delta\beta$ due to the offset in the angular component $\Delta\phi$ of an off-axis source parallel to the dispersion direction, the angle of incidence α, the grating exit angle β, the focal length F, and the distance between the Reflection Grating Assembly and the prime focus L.

The images were corrected for exposure and binned to a pixel size of $0.4''$. In the next step we included the RA-DEC coordinate system. As the reference coordinate, we chose the coordinate of the centre of NGC 253 (the position of the brightest IR source in the galaxy, $\alpha_{2000} = 0^{\mathrm{h}}47^{\mathrm{m}}33{.}^{\mathrm{s}}3$, $\delta_{2000} = -25°17'18''$, Forbes et al. 2000). In the cross-dispersion direction, the position of our reference coordinate on the CCD could be taken directly from the source list file that was produced in processing of RGS data. In the dispersion direction the position is given in the above procedure by the Doppler shift corrected line centre position. The galaxy's systemic velocity of 243 km s^{-1} (Koribalski et al. 2004) had to be accounted for. This shifts the reference coordinate in the dispersion direction by $\sim 0.35''$ Å^{-1} times the centre wavelength in which the image is calculated, e.g. $6.6''$ for the O VIII image. The effects of the velocities of the earth with respect to the sun and *XMM-Newton*'s orbital velocity can be neglected since they are only of the order of $0.7''$ and $4''\times 10^{-4}$, respectively, in the O VIII image where the effect would be greatest, and therefore much smaller than the width of the point spread function. The images for the lines were created separately for each of the three observations and were then combined into one image. In a final step the images were smoothed with a Gaussian filter.

In general the method is affected by two different effects: (i) a Doppler shift due to the radial velocity component of an emitting source changes its position in the image along the dispersion direction axis. A radial velocity of 1000 km s^{-1} would correspond to $21.6''$at a

wavelength of 15.0 Å. (ii) Assuming there is not just one but two lines in the wavelength extraction interval, we would have two images of the object in the resulting image, superimposed with an offset along the dispersion direction of 7.2′ Å^{-1}. For example the emission in the two Fe XVII lines at 16.780 Å and 17.055 Å would be superimposed with an offset of ∼2.0′. The Fe XVII at 17 Å image is the only case where we actually have to consider that we have created an image using two lines, i.e. the Fe XVII lines at 17.055 Å and at 17.100 Å. The lines are not separated in the spectra and they appear about equally strong, which is most likely an effect of the low statistics. According to theory (Mewe et al. 1985), the line strength of the latter line should be ∼52–85 % of the former one, depending on the temperature of the plasma (1.08 keV and 0.11 keV, respectively). The separation of the lines is 0.046 Å, which corresponds to a shift in the dispersion direction of 19.9″. By smoothing the image with a larger Gaussian with a FWHM of 20″, we can account for the error we make by using both lines.

Images in the Ne X, Fe XVII and O VIII lines are shown in Fig. 5.5. The number of photons that were extracted from all three observations are 806, 1077, 816, and 1231 for the images in the Ne X (11.98–12.35 Å), Fe XVII at 15 Å (14.86–15.13 Å), Fe XVII at 17 Å (16.90–17.21 Å), and O VIII (18.80–19.17 Å) lines, respectively. The FWHM of the Gaussian filter was 12″ for Ne X, Fe XVII at 15 Å, O VIII, and 20″ for Fe XVII at 17 Å.

5.1.3 RGS cross-dispersion profiles

To get additional spatial information on the line distribution, we produced emission line profiles in the cross-dispersion direction. Therefore we extracted events from the RGS eventfiles by applying the same filters in wavelength and wavelength-energy-space as for generating the RGS images, but then we binned the counts into 30″ bins to match the extraction regions that were applied to the spectra. Background counts in the respective wavelength ranges were taken from the spectra that were obtained with the RGS background model task and subtracted from the emission line profiles. Four of these profiles are shown in Fig. 5.4.

5.1.4 EPIC-PN images

To verify the results from the RGS images, we also extracted EPIC PN narrow-band images in approximately the same energy ranges. Therefore we filtered the PN eventfiles in the energy bands around Ne X (992–1052 eV), Fe XVII at 15 Å (795–844 eV), O VIII (625–690 eV), and Fe XVII at 17 Å (694–734 eV). The spectral resolution of the EPIC PN detector is ∼70 eV, so it is possible that photons with higher or lower energies contribute to the energy band of interest. There is also contamination from higher energies due to the redistribution in the detector. Photons can lose up to 60% of their energy in the CCD before they are

detected. This means that bright features in some energy range can show up to some degree in lower energy bands. The filtered eventfiles of the different observations and instruments were merged using the SAS task merge. We created images of the eventfiles and smoothed them with a Gaussian of $6''$. The resulting images are shown in Fig. 5.6.

5.1.5 EPIC-PN brightness profiles

To detect the limb brightening of the outflow, as found by Strickland et al. (2000) and Pietsch et al. (2001), we also extracted brightness profiles perpendicular to the outflowing direction from the merged PN eventfiles of all observations. Furthermore, to check for an energy dependence in the limb brightening, we subdivided them into energy bins with a width of ~150 eV starting from 400 eV up to 2000 eV. The emission lines of O VIII and the Fe XVII lines are included in the energy ranges 550–700 eV and 700–850 eV, respectively. Ne X is mostly in the 1000-1150 eV bin. The extraction regions match the regions we used for the RGS spectra. Furthermore we split the region SE 1 into the two regions 'SE 1 (1)' and 'SE 1 (2)' with a width of $15''$ in the cross-dispersion direction of the RGS. The brightness profiles, sorted by energy band, are shown in Fig. 5.7. Since we are interested in the emission neither from the nucleus nor from the bright source X33 southwest of the nucleus, the profiles are limited to a maximum of 250 counts. This still shows the main features in the central and SE 1 (1) region, while cutting off the peaks in some cases.

5.2 Results

5.2.1 RGS spectra

The RGS spectra show emission in many different lines (Fig. 5.3). Especially in the region including the major axis of NGC 253 (Centre), a large variety of lines from different elements can be identified. The spectra extend from the Si XIV line at the highest energy down to the C VI line at the low energy end ($\lambda = 6 \ldots 34$ Å). All the He-like ions in this range (Si XIII, Mg XI, Ne IX, O VII, and N VI) and their corresponding ions in the next higher ionisation state (Si XIV, Mg XII, Ne X, O VIII, and N VII) can be resolved. The iron $3d$-$2p$ transitions around 15 Å, as well as the $3s$-$2p$ lines around 17 Å, are detected, i.e. their peak heights are more than twice the error in the wavelength bin. Also the lines at ~16.0 and ~16.1 Å can be clearly detected, but it is not clear whether the line at ~16.0 Å is from Fe XVIII or from O VIII. In the range 10 Å to 11.5 Å there is an indication of iron lines from Fe XXIII and Fe XXIV.

A spectral feature that is prominent in the spectra is a broad base at the Fe XVII lines at
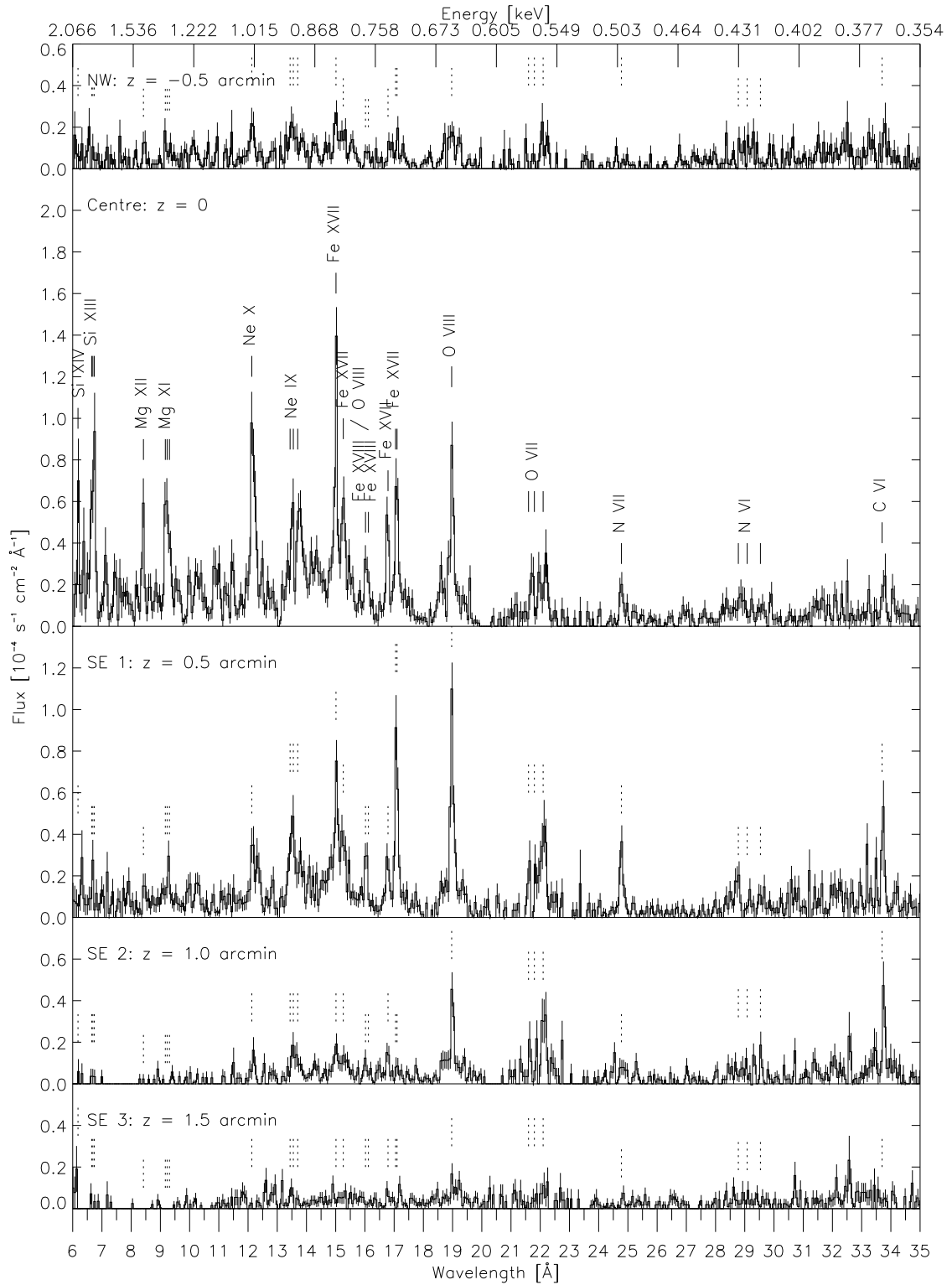
Figure 5.3: Combined RGS spectra of NGC 253 extracted from different regions along the outflow. The label gives the southeast position z of the extraction region along the minor axis relative to the centre of the galaxy in arcmin.

Table 5.1: Flux values for different emission lines in the extraction regions.

Transition	$\lambda_{\text{expected}}$[a]	Flux			
	(Å)	$(10^{-6} \text{ s}^{-1} \text{ cm}^{-2})$			
		NW	Centre	SE 1	SE 2
Si XIV	6.18		5.6 ± 4.3		
Si XIII w	6.65		5.8 ± 3.4		
Si XIII x+y	6.69		4.0 ± 2.8		
Si XIII z	6.74		9.2 ± 4.3		
Mg XII	7.11		6.5 ± 3.0	1.9 ± 1.6	
Mg XI w	7.76	1.4 ± 1.3	6.5 ± 2.7	1.3 ± 1.2	
Mg XI x+y	7.81		5.4 ± 2.4	1.7 ± 1.3	
Mg XI z	7.87		6.3 ± 2.6	2.5 ± 1.6	
Ne X	12.1	3.4 ± 2.2	16 ± 4.5	5.7 ± 2.6	2.0 ± 1.6
Ne IX w	13.5		4.3 ± 2.3	5.4 ± 2.5	
Ne IX x+y	13.6	3.0 ± 2.0	6.2 ± 2.8	6.1 ± 2.7	2.4 ± 1.8
Ne IX z	13.7	1.8 ± 1.6	7.6 ± 2.8	4.1 ± 2.2	
Fe XVII15	15.0	4.5 ± 1.9	18 ± 3.8	13 ± 3.1	3.3 ± 1.6
Fe XVII17	17.1	3.0 ± 1.7	13 ± 3.8	13 ± 3.9	
O VIII	19.0	6.7 ± 2.5	16 ± 3.8	18 ± 4.0	6.9 ± 2.5
O VII w	21.6		2.3 ± 2.2	3.0 ± 2.4	
O VII x+y	21.8		3.4 ± 2.6		
O VII z	22.1	5.1 ± 3.3	9.5 ± 4.4	13 ± 5.2	
N VII	24.8		2.2 ± 1.5	6.3 ± 2.8	1.5 ± 1.3
N VI w	28.8	1.4 ± 1.3		4.2 ± 2.4	
N VI x+y	29.1			2.4 ± 1.8	
N VI z	29.5			3.2 ± 2.0	1.8 ± 1.5
C VI	33.7	3.0 ± 2.5	4.5 ± 3.0	6.6 ± 3.3	5.7 ± 3.1

[a]The references for the expected wavelengths ($\lambda_{\text{expected}}$) are Mewe et al. (1985) and Phillips et al. (1999).
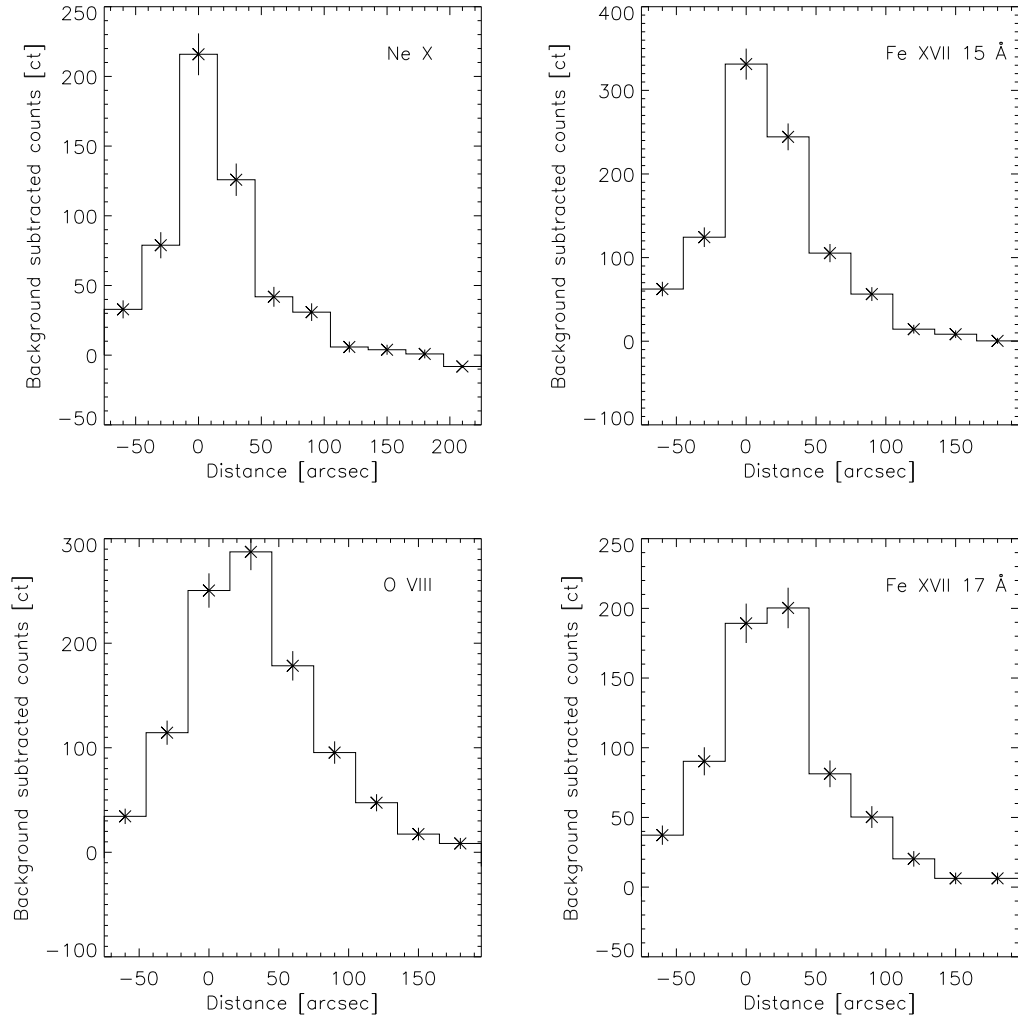
Figure 5.4: Ne X (upper left), Fe XVII at 15 Å (upper right), O VIII (lower left), and Fe XVII at 17 Å (lower right) profiles of background-subtracted counts versus cross-dispersion distance for the combined NGC 253 RGS1 and RGS2 data. The bin at distance zero corresponds to the extraction region 'Centre'. Negative distances are towards the northwest, and positive values correspond to areas to the southeast.

15 Å and 17 Å and at the O VIII and O VII line positions with a width of up to ∼0.5 Å. If this line broadening is caused by the velocity dispersion of the outflowing gas, it would imply deprojected velocities of up to ∼40000 km/s, corresponding to temperatures of ∼10^{11} K. Such high velocities disagree with outflow velocities in other galaxies. Extreme cases show values of up to ∼3600 km/s (e.g. in NGC 3079, Veilleux et al. 1994). A more plausible explanation for the broad base is contributions from the disc emission of NGC 253: In Fig. 5.1 disc emission extends about 200″ in the dispersion direction (major axis of the galaxy) in both directions from the centre. This corresponds to a ∼0.5 Å shift in wavelength and can therefore explain the observed effect.

The region northwest of the centre (NW) is strongly affected by absorption from the galactic disc that lies between the outflow and the observer. Pietsch et al. (2000) derive an additional absorbing column N_H of $1 - 2 \times 10^{21}$ cm^{-2} for this position northwest of the centre. Therefore most of the lines are only weak or not detectable at all. If we assume that the north-west and southeast outflow have a similar intrinsic spectrum, then absorption can fully account for the difference between regions NW and SE 1, at the same projected distance from the centre. The strongest lines in the NW region are from Ne X, Ne IX, Fe XVII at ∼15 Å and ∼17 Å, O VIII and from the forbidden line of the O VII triplet, but most of the emission originates in the disc and is smoothed out into the broad base, as mentioned above.

The regions southeast (SE 1 to SE 3) of the centre do not suffer from this absorption by the disc. One can easily follow how the lines increase or decrease in strength when going away from the galactic disc southeast along the minor axis. The lines at short wavelengths from silicon and magnesium are the first to disappear with distance from the centre. The Ne X line is seen to decrease considerably in strength southeast of the Centre region, whereas the line from the lower ionised Ne IX is not affected as much and is even stronger than the Ne X line in regions SE 1 and SE 2. All the lines from iron decrease in strength except for the Fe XVII lines at 17 Å, which grow by a factor of ∼1.5. Also the O VIII line increases in strength. The O VII triplet has about the same strength in region SE 1 as in the Centre region. The lines from N VII and C VI increases in strength compared to the central region. Further away from the centre, in region SE 2, the Fe XVII lines at ∼15 Å are still detectable and the O VIII line is the strongest line in the spectrum. Also the O VII triplet is still strong. The detection of all the other lines is below 2σ, even though the lines at wavelengths longer than 12 Å can still be identified. Only very weak lines from O VIII and from the Ne IX triplet remain in region SE 3.

Unfortunately the statistics in the spectra are not good enough to allow a quantitative spectral analysis with XSPEC. However, several conclusions can be drawn.

Temperature estimates can be inferred from line ratios of different elements or of the same element in different ionisation states using model calculations. Assuming collisional

ionisation equilibrium (CIE), Mewe et al. (1985) calculated line strengths for different elements and transitions depending on the temperatures of the plasma. By measuring the fluxes of two transitions in a spectrum and taking the ratio of these, the obtained value can be compared with the tables in Mewe et al. (1985) and the temperature of the plasma can be derived.

We used the line strength ratio between the Ly_α state of a given element and its helium-like charge state that matched the morphology of the Ly_α state in the RGS images best. The line strengths were derived by integrating the flux of the line over the wavelength (cf. Table 5.1). We found that the derived temperature value and its error show only a weak dependence on how much of the wings of the line we include in the flux integration. The resulting temperatures for Si, Mg, Ne, and O and their variation along the outflow direction are shown in Table 5.2. Using only the peak height of the line, however, gives temperatures that are lower, except for oxygen in the regions Centre and SE 1, compared to the values shown in Table 5.2 by up to 50%.

Table 5.2: Temperatures of the plasma for different regions of the outflow of NGC 253 derived from line ratios of different elements.

Region	Temperature in keV			
	Si	Mg	Ne	O
NW		0.61±0.08	0.51±0.08	0.21±0.01
Centre	0.79±0.06	0.66±0.04	0.43±0.02	0.22±0.01
SE 1		0.46±0.04	0.38±0.03	0.21±0.01
SE 2			0.25±0.02	0.31±0.04

Using the line flux from an emission line (cf. Table 5.1) and an estimate of the size of the emitting region, we can derive electron densities for the nuclear region of NGC 253 and the southeastern outflow. Mewe et al. (1985) give the line power P' normalised to the electron density for different temperatures and X-ray emission lines. The electron density can then be derived using the formula

$$n_e = \sqrt{\frac{F E_\gamma 4\pi d^2}{V P'}} \qquad (5.2)$$

where n_e is the electron density, F the flux (in counts s^{-1} cm^{-2}) in an emission line with E_γ from an emitting region with volume V and distance d. The emitting region is assumed to
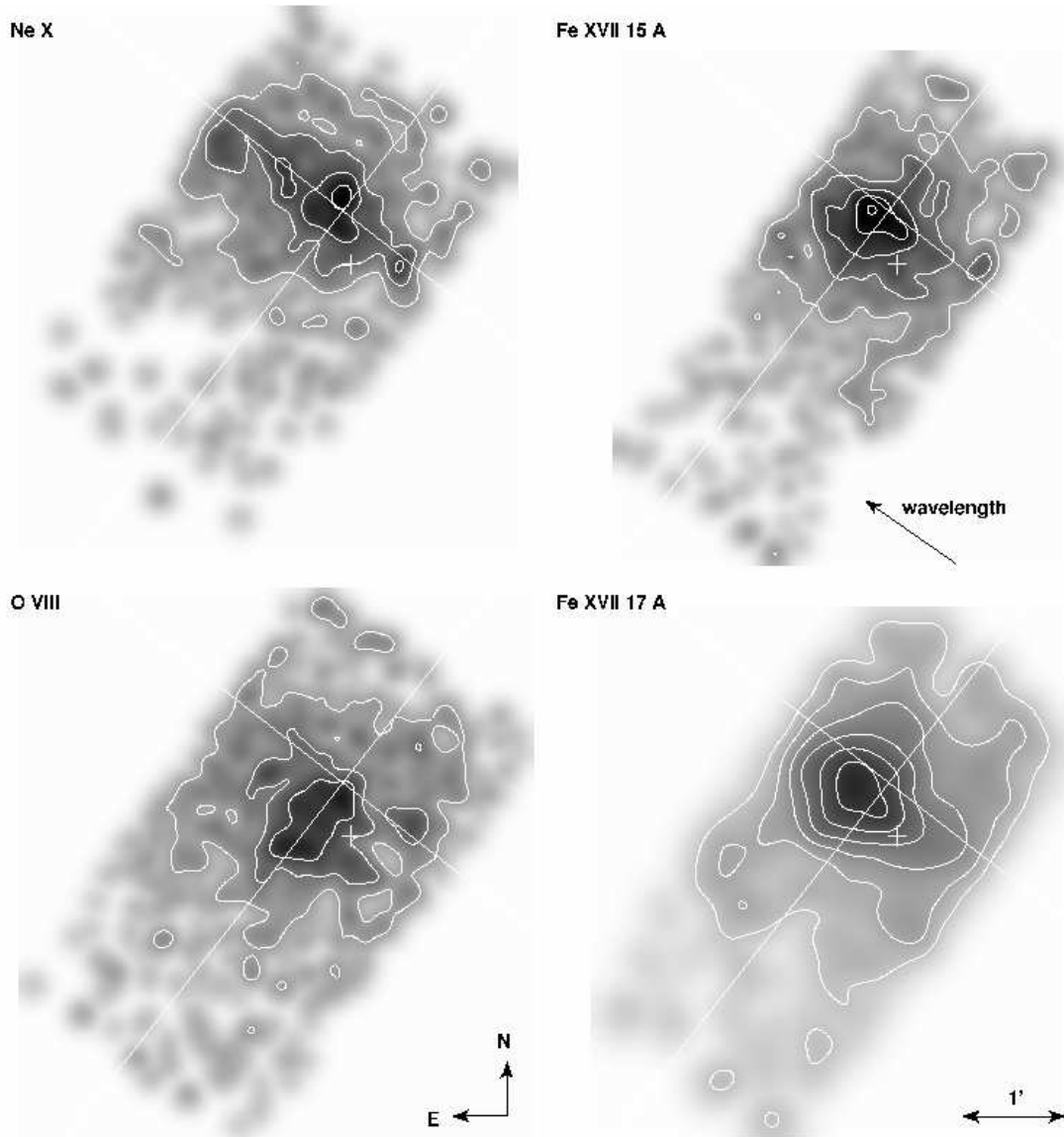
Figure 5.5: RGS images of NGC 253 in the Ne X, Fe XVII and O VIII lines. The white lines mark the major (northeast to southwest) and minor axis (northwest to southeast) of NGC 253. The image in the Fe XVII line at 17 Å was smoothed with FWHM of 20″, all others with 12″. White contours indicate 2σ, 3σ, 4σ, ... above the background. The white cross southwest of the nucleus marks the bright source X33 from Pietsch et al. (2000). The RGS dispersion direction is such that wavelength increases from southwest to northeast as indicated by the arrow.

be uniform in n_e.

For the central region we selected the Ne X line and assumed a uniform, spherical emitting region with a radius of $\sim$160 pc. The outflow in region SE 1 is represented best in the O VIII line, and we assumed a uniform, cylindrical volume with a radius of $\sim$200 pc and a height of 375 pc, the latter being confined by the extraction region. We selected these lines because they are strong in the spectra and because we can get a good estimate for the emitting volume from the RGS images. The resulting electron densities are $n_{\mathrm{e,nucleus}} = 0.106 \pm 0.018 \ \mathrm{cm}^{-3}$ and $n_{\mathrm{e,outflow}} = 0.025 \pm 0.003 \ \mathrm{cm}^{-3}$ for the nucleus and the outflow region, respectively.

Apart from the derivation of temperatures and electron densities, some selected emission lines can be used as diagnostic lines. The Fe XVII lines at 15 Å and 17 Å can be used to derive the ionising mechanism in the plasma. In the Centre region of NGC 253, as well as in the regions NW and SE 2, the line strengths indicate a predominantly collisional ionised plasma. Region SE 1, however, shows an inverted line ratio. Here the lines at 17 Å are stronger than the lines at 15 Å, which points at a photoionised plasma.

In general the helium-like line triplet of O VII can provide the electron density, the electron temperature, as well as the ionisation process (Porquet et al. 2001). However, we refrained from using the O VII triplet for the following reasons. In the combined and fluxed spectra, the significance is below 3 σ for most of the spectral bins. Also the individual lines are not clearly distinguishable from each other. This is probably enhanced due to the use of the task `rgsfluxer` as described above. We also refrained from doing a simultaneous fit of the single uncombined spectra with XSPEC, as the statistics in one single spectrum are barely above 2 σ for the strongest bin.

5.2.2   RGS cross-dispersion profiles

In the cross-dispersion profiles (Fig. 5.4), line emission is strongest in the Centre bin at a distance of 0″ for Ne X and Fe XVII at 15 Å. In the O VIII and Fe XVII at 17 Å, profile this is not the case. Here the SE 1 region at a distance of +30″ is the brightest. However the northwest half of the central bin is already affected by absorption from the disc. When one bins the brightness profile into smaller spatial regions, the strength drops dramatically in the central bin and towards the northwest. Towards the southeast, on the other hand, it only drops slowly. Farther to the southeast with distances larger than 45″, the Ne X and the Fe XVII profiles show a large drop in brightness, whereas the O VIII profile declines with a flatter gradient. Therefore the Ne X and Fe XVII emissions are more concentrated within the disc, whereas the O VIII emission extends farther away from the disc. The general behaviour is for the emission from higher energy lines to be more concentrated and not as extended as in

M82 (Read & Stevens 2002).
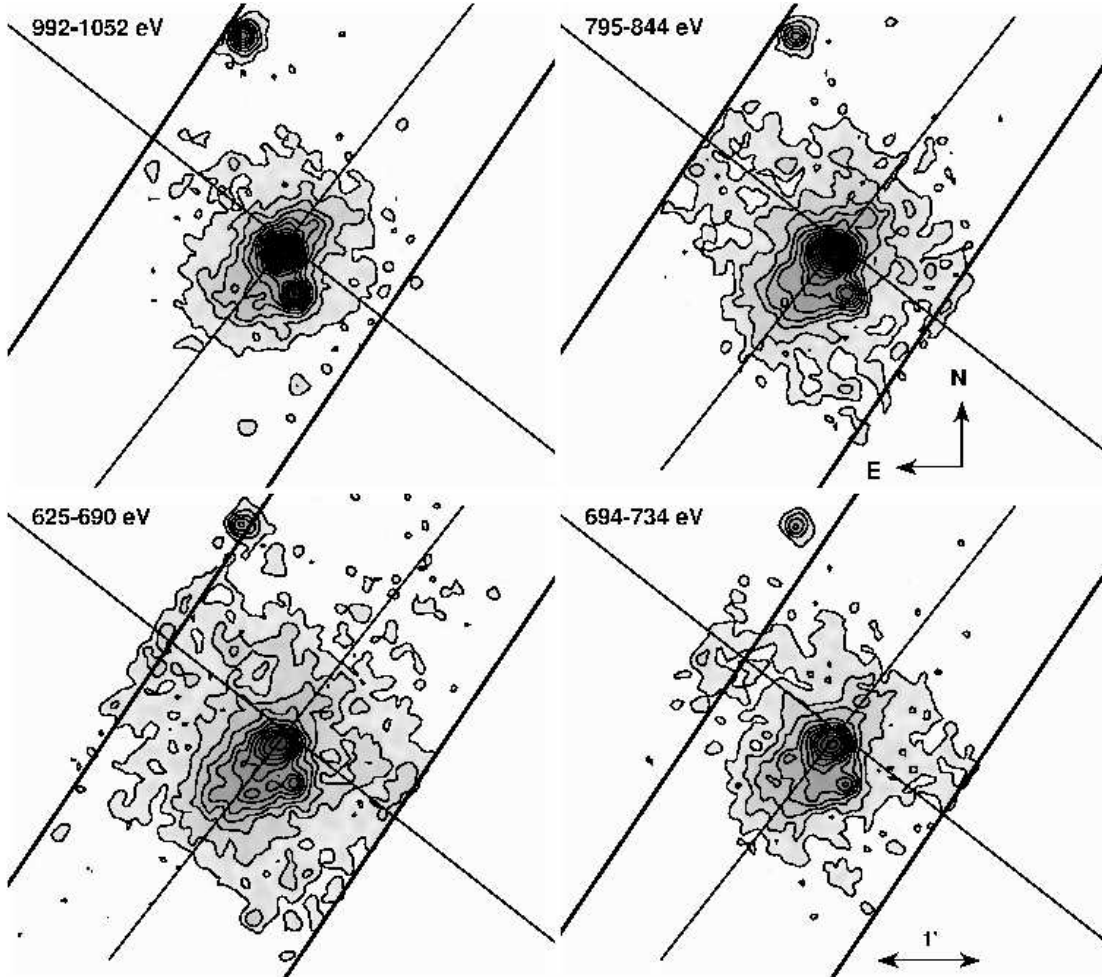
Figure 5.6: EPIC PN images of NGC 253 in the energy bands around the Ne X (922–1052 eV), Fe XVII (795–844 eV and 694–734 eV), and O VIII (625–690 eV) lines. The images show the region of NGC 253 that is covered by the RGS images (Fig. 5.5). The thin black lines mark the major (northeast to southwest) and minor axis (northwest to southeast) of NGC 253. The area within the thick black lines gives the extraction region in the corresponding RGS line image. Black contours indicate 2σ, 3σ, 4σ, ... above the background. The images were smoothed using a Gaussian with a FWHM of $6''$.

5.2.3   RGS images

The RGS images allow us to derive additional information about the spatial composition of the outflow. But before we describe the images in more detail, we need to point out that these images are dominated by low statistics. We therefore restrict our results and conclusions on

the regions with good statistics.

The strong O VIII emission clearly traces the outflow. It reaches out to a ∼750 pc projected distance along the southeast minor axis and has an extent perpendicular to that of ∼400 pc. Because of the high absorption, emission from the farther side of the disc is not detected. With the RGS spatial resolution, the outflow in O VIII does not show limb brightening. The emission is strongest close to its central axis and its intensity decreases towards the border. This suggests that the emitting ions are not concentrated on the borders of the outflow where the outflow gas interacts with the surrounding material, but that this emission comes directly from the outflowing gas. The extent to the southeast is less than the one in the EPIC images where the bright outflow emission can be followed to ∼1.3 kpc (Fig. 5.6), due both to the sensitivity and to the smaller energy band ($\Delta\lambda$ =1.87 Å vs. 0.37 Å) that was used to extract the images for the RGS. The emission from Ne X is clearly concentrated in the disc and nucleus, and it does not contribute to the outflow. Both images in the iron lines show the strongest emission southeast of the nucleus and the emission is slightly extended along the outflow direction. However, they do not trace the outflow morphology as seen in the O VIII line. This is not surprising, because the excitation cross sections for the iron and O VIII lines have a different temperature dependence. Due to the work that is performed when the outflow expands against the pressure of the ambient medium, as well as to the divergence of the flow in the cone perpendicular to the disc, the temperature or more precisely the kinetic energy of the electrons should decrease (e.g. Breitschwerdt & Schmutzler 1999) with height z above the disc, explaining the relative increase in emission of O VIII to iron.

5.2.4 EPIC-PN images

We find that the EPIC PN narrowband images (Fig. 5.6) are all affected by the redistribution effect of the detector; i.e. the image is contaminated by events with higher energies from outside the energy filter boundaries. Especially very bright sources, like the central source of the galaxy, contribute strongly to this effect and all images will therefore show these sources. The bright nuclear source is clearly visible in all of the EPIC PN images. Also, the bright source ∼0.5′ southwest of the nucleus is clearly visible in all EPIC PN images. For the RGS images the latter is only true for the Fe XVII at 15 Å image. This clearly shows the advantage, namely the far better energy resolution, of the RGS images compared to the EPIC PN narrowband images.

With respect to the limb brightening of the outflow emission, the image in the energy range 694–734 eV (including the Fe XVII at 17 Å line) indicates a morphology that could result from a limb-brightened outflow at a distance of ∼0.7' away from the galactic centre. Also in the energy range 625–690 eV (including the O VIII line), there is an indication of

this morphology at a distance of about 1.1'. The corresponding RGS image unfortunately has statistics too low to confirm this. The other images indicate no limb brightening.

5.2.5 EPIC-PN brightness profiles

In the EPIC-PN brightness profiles (Fig. 5.7), the peak in region SE 1 (1) that is caused by the outflow emission always coincides with the centre. A double peak with a central depression is visible in SE 1 (2) and SE 2 at 700–1000 eV (covering also the iron lines). This may point at a limb-brightened outflow in this region. An indication of this structure in region SE 2 at 550–850 eV could be a redistribution effect of the detector (see above). At other energies no indication of limb brightening can be seen. The profiles show either a flat plateau or a hump peaking around the centre of the outflow. This confirms the findings of the RGS images. Starting from 700 eV region NW comes out and it is stronger than the two SE 1 regions together in energies above 1150 eV. The strong peak in the region SE 1 (1) at $\sim+20''$ distance is the bright point source south-west of the nucleus and not part of the outflow region.

To rule out that our findings are affected by *XMM-Newton*'s spatial resolution, we compared brightness profiles, extracted with the same regions and energy bands from *Chandra* observation 3931, to the EPIC PN profiles. There the double peak is clearly detected in region SE 1 (2) between 700 and 1000 eV, possibly also up to 1150 eV. It is not visible in regions SE 1 (1) or SE 2. The profiles in region NW show the same behaviour as in the EPIC-PN data, so taking the differences in the instruments into account *XMM-Newton* and *Chandra* give a consistent picture.

5.3 Discussion

5.3.1 Line ratios and temperatures

The extracted RGS spectra of the outflow along the minor axis of the galaxy show emission lines from many ions in different ionisation states: the Ly_α lines from Si, Mg, Ne, O, and N and also their helium-like charge states. Additionally we see emission lines from Fe XVII and Fe XVIII.

With increasing distance from the nuclear region, the relative flux in the O VIII line intensifies compared to the flux in Fe XVII; i.e. the line flux at longer wavelengths increases. The same effect can also be seen in the line flux ratio of O VII to O VIII. For the oxygen line ratio, this implies that the temperature decreases; the gas is cooling as it flows away from the nucleus. This change in temperature would also affect the excitation of Fe XVII.
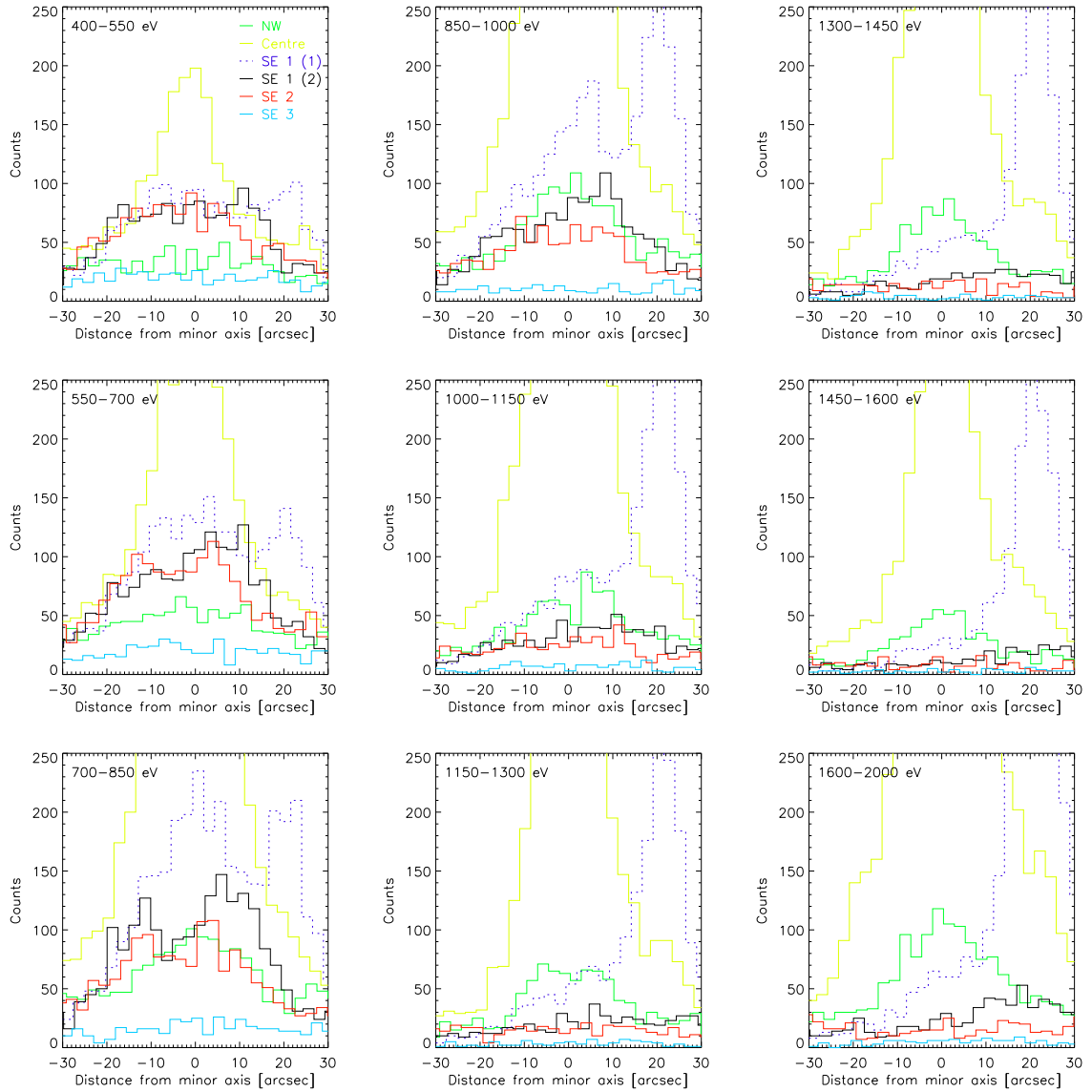
Figure 5.7: EPIC PN brightness profiles of the outflow region for the RGS extraction regions sorted by energy band. Note that region SE 1 was split into the two regions 'SE 1 (1)' and 'SE 1 (2)' with a width of 15″ in the cross-dispersion direction of the RGS. The abscissa gives the distance from the minor axis of the galaxy in arcsec. Positive values are to the southwest, negative to the northeast. The presented histograms consist of raw detector counts, i.e. the background and the detector characteristics, like quantum efficiency or effective area, were not taken into account.

Since both elements, oxygen and iron, are from the same kind of sources, i.e. type II SNe, it seems unlikely that the distribution is different, unless there is a very different clumpiness in O and Fe initially. Therefore a change in the oxygen to iron line flux is more likely due to the change in temperature than due to a different radial abundance profile.

The line strengths of the Fe XVII lines at 15 Å compared to the one at 17 Å indicates a predominantly collisional ionised plasma. Region SE 1, however, shows an inverted line ratio. There, the flux in the Fe XVII lines at 17 Å is enhanced compared to the lines at 15 Å. This points to a photoionised plasma, but no strong photoionising sources were detected in the vicinity. There are two additional alternatives to create this line ratio:

A) the plasma is highly underionised compared to the ionising electrons. The time since the heating of the plasma was too short to reach an equilibrium state. In these so-called underionised plasmas, inner-shell ionisation is highly operational (Kosenko 2006) and leads to an enhanced 17.10 Å flux from Fe XVII (Doron & Behar 2002). Examples that show underionised plasmas are supernova remnants like N132D (Behar et al. 2001) and Dem L71 (van der Heyden et al. 2003).

B) the plasma is overionised. It can be produced in fast adiabatic cooling of hot ($T \sim 10^8$ K) and almost completely ionised gas expanding out of a superbubble (Breitschwerdt & Schmutzler 1999). The ionisation cross sections, as well as the recombination cross sections, are different for all ions, so when a shock propagates through the outflow region, the ionisation of different elements and different ionisation stages occurs on different time scales for each. As the expansion of the wind occurs on much shorter time scales than radiative recombination, the highly ionised atomic states remain frozen-in. These states then recombine at a later time farther away from the nucleus. This is called delayed recombination. In both regions, Centre and SE 1, we see emission from Fe XVIII, which is produced in the hot starburst region of the galaxy. As the wind breaks out of the nuclear superbubble and expands into the lower density medium along the minor axis of the galaxy, it cools mostly adiabatically. However, the Fe XVIII in the wind recombines on a larger time scale than the wind fluid, so we have Fe XVIII in abundance, although the electron temperature would preferentially admit Fe XVII. When the Fe XVIII ions then recombine to Fe XVII, the states of Fe XVII that decay via the 17 Å lines are preferably populated compared to the ones that decay via the 15 Å lines. This enhances the flux at 17 Å and could lead to the misleading line ratio in this region.

Temperatures derived from line ratios of individual elements are in the range of 0.21 ± 0.01 to 0.79 ± 0.06 keV. This range is wider than the one found by Strickland et al. (2000) using *Chandra* ($0.46^{+0.11}_{-0.10} - 0.66^{+0.10}_{-0.08}$ keV). However Strickland et al. (2000) used only a single-temperature MEKAL hot plasma model for each extraction region. Given the complexity of the X-ray producing mechanisms, this approach is definitely too simple. Our de-

rived temperature range is closer to the one given by Pietsch et al. (2001) from *XMM-Newton* EPIC spectra, who used three MEKAL models (0.15, 0.53, and 0.94 keV). The approach in this work of deriving temperatures tries to account for the high complexity of the outflow, without the claim of completeness, by actually using one MEKAL model for each element, and by taking advantage of the superior energy resolution of the RGS. This approach already gives almost the whole measured energy range just for the Centre region, whereas Strickland et al. (2000) obtain this range of temperatures by using several different extraction regions along the outflow.

Looking at the temperatures of just one extraction region, we see that different elements give different temperatures. This could be due to sampling different regions along the line of sight, but also due to delayed recombination. The latter is a true non-equilibrium ionisation (NEI) situation and the result would be measuring different temperatures for different ions. All of the above temperatures were derived by the use of models that assume CIE for the emitting gas. This is not necessarily the case for an outflow. To avoid this assumption we would have to fit the spectra to NEI models (e.g. from Breitschwerdt & Schmutzler 1999). These models entail a higher level of complexity as they depend crucially on a detailed hydrodynamical model of the outflow. Therefore they are sensitive to the time evolution of the wind and, as such, are unique. In other words, NEI models would enable us to fully exploit the information buried in the X-ray spectra, since we could calculate a series of models with different boundary conditions and then derive suitably binned synthetic spectra for fitting the observational results. Thus a satisfactory fit would determine the physical parameters of the outflow within certain limits.

The Fe lines could be used as well to derive temperatures. However, the emission from Fe XVII at $\sim$15 Å (2p-3d) and at $\sim$17 Å (2p-3s) are affected by delayed recombination of Fe XVIII, which contradicts the CIE assumption. Therefore the results could be misleading and are not shown in Table 5.2. However from the fact that the Fe XVII at 15 Å lines are present and strong in the spectra, the temperature has to be above 0.22 keV in the regions where the Fe L shell originates; otherwise Fe XVII line formation is inefficient (Rugge & McKenzie 1985). Furthermore calculations show that, above 0.60 keV, Fe XVIII is strong while Fe XVII is weak. This is not the case in any of the regions from which we obtained spectra, therefore we expect that kT=$0.2\ldots0.6$ keV

The RGS images give another indication of the cause of the large temperature spread. The different distribution of the events for each emission line strongly points to the fact that plasmas in different regions of space are responsible for the line emission. It is not surprising that these plasmas then do not have the same temperature and that the temperatures for each element are different. The time scale for attaining pressure, hence temperature equilibrium in the starburst region, is of the order of the sound crossing time. If we compare this to

the average time interval between supernova explosions, we can assess the smoothness of the temperature distribution. A rate of $0.05\,\mathrm{yr}^{-1}$ has been quoted for NGC 253 (Colina & Perez-Olea 1992). A supernova blast wave expanding within a hot tenuous gas has a low Mach number, so that the sound crossing time, τ_{sc}, in the starburst region is roughly the time scale for the shock wave to reheat the hot gas. Adopting a value of $20''$ or $d = 250$ pc and a temperature of 0.6 keV or 6.6×10^6 K for the central region yields a value of $\tau_{sc} \sim d/c_s \simeq 8.2 \times 10^5$ yr, which is much larger than the interval of 20 years between successive explosions, even if we decrease the supernova rate by a factor of $10 - 100$ for the starburst region. Therefore temperature inhomogeneities in the starburst region and hence variations in the ionisation stages are to be expected. As the flow moves away from the disc sources, the temperature structure should, however, become smoother with time when the flow time becomes larger than the sound crossing time τ_{sc}.

Strickland et al. (2000) argue that the spectral variation in *Chandra* spectra 'along and between the northern and southern outflow cones is due to variations in the absorption column and not due to significant temperature variations along the outflow'. A higher absorption column is certainly the case for the NW region, resulting in temperature values that are too high. Although from the analysis of the *XMM-Newton* RGS spectra we cannot draw conclusions regarding the absorbing column, we find that there is a significant temperature variation along the outflow. The temperatures for Mg and Ne decrease with distance to the southeast from the centre. The temperature of oxygen seems to be constant, except for the value in region SE 2.

5.3.2 The morphology of the outflow

The only RGS image that clearly shows the outflow geometry is the one in the O VIII line. The shape of the southeastern outflow matches roughly the truncated cone with an opening angle of $\sim 26°$ that is seen in *Chandra* and H_α data (Strickland et al. 2000), though the angle in the O VIII image appears to be slightly smaller. Also, this emission is not limb-brightened. The image suggests that the outflow cone is filled with clumpy distributed O VIII. If this is correct, then we see the emission from the hot wind fluid itself for the first time. The clumpiness may be caused by mass-loading, i.e. the turbulent process of mixing in ambient ISM and infalling material. This detection of the wind fluid, however, contrast with the statement from Strickland & Stevens (2000) that the wind is too thin to emit efficiently enough to be detected.

In *XMM-Newton* EPIC observations by Pietsch et al. (2001) and in *Chandra* observations by Strickland et al. (2000), the outflow shows a limb-brightened morphology. In our analysis we find limb brightening in the Fe XVII at 17 Å RGS images. The comparison between

the different PN images and brightness profiles, though with lower spectral resolution, also shows an energy dependence of limb brightening and a clear detection of the emission from the outflowing gas at the energies below 700 eV.

Strickland & Stevens (2000) found from simulations that low opening angles for outflows are only possible when a thick galactic disc is present. This produces opening angles from a few degrees when the wind starts to blow out of its superbubble and then increases up to values of $\sim 60°$, depending on boundary conditions. Thin-disc models typically show opening angles of $\sim 90°$. However, these simulations assumed an ISM distribution in rotating hydrostatic equilibrium with the gravitational field. Simulations by de Avillez & Breitschwerdt (2004, 2005) show that the ISM in the disc has a highly complex structure. This affects the break-out dynamics of a superbubble via density and pressure gradients and also via "holes" from previous outflows that have not closed yet. Conclusions about the thickness of the disc and its collimating effect are hence difficult.

84

Chapter 6

Conclusions and Outlook

6.1 Conclusions

In this work, we presented the analysis of a selection of X-ray phenomena in the starburst galaxy NGC 253. This investigation was mostly based on four observations carried out with the X-ray observatory *XMM-Newton* between June 2000 and June 2003.

We have performed a detailed analysis of *ROSAT* and *XMM-Newton* observations of the recurrent ultraluminous X-ray source NGC 253 ULX1 (see Chapter 3). This transient is one of the few ULXs that was detected during several outbursts. The luminosity reached 1.4×10^{39} erg s^{-1} and 0.5×10^{39} erg s^{-1} in the detections by *ROSAT* and *XMM-Newton*, respectively. In the *ROSAT* detection NGC 253 ULX1 showed significant time variability, whereas the luminosity was constant in the detection from *XMM-Newton*. In all other available observations by *ROSAT*, *XMM-Newton*, and *Chandra*, the luminosity of the source was below the detection limit. The *XMM-Newton* EPIC spectra are well-fit by a bremsstrahlung model (kT= 2.24 keV, $N_H = 1.74 \times 10^{20}$ cm^{-2}), which can be used to describe a comptonized plasma. According to the highest observed luminosity of 1.4×10^{39} erg s^{-1} of NGC 253 ULX1, the lower limit for the mass of the compact object would follow as 11 M$_\odot$, if it was isotropically emitting. Therefore, the compact object in NGC 253 ULX1 may be a stellar mass black hole. No IMBH is required to explain the emission. From the lack of an optical counterpart we could exclude that NGC 253 ULX1 is a HMXB. Therefore NGC 253 ULX1 most likely is an anisotropically emitting LMXB.

In Chapter 4, we have characterised the diffuse emission in the disc and halo of NGC 253. The extent of the diffuse emission along the major axis of the disc is 13.6 kpc. Disc regions that cover star forming regions, like spiral arms, show harder spectra than regions with lower star forming activity. Models for spectral fits of the disc regions in the energy range between 0.2 and 10 keV need at least three absorbed components: two thermal plasmas with solar

abundances plus a power law. Temperatures are between 0.1 and 0.3 keV and between 0.3 and 0.8 keV for the soft and the hard component, respectively. The power law component may indicate an unresolved contribution from X-ray binaries in the disc. The total luminosity of the diffuse emission in the disc is 2.4×10^{39} erg s^{-1} (0.2-10.0 keV). From a comparison between X-ray and K-band observations, we concluded that the diffuse emission is not just unresolved emission of an old stellar population, but has a strong component from a hot plasma.

The halo resembles a double horn structure which reaches out into both hemispheres to a projected height of $\sim$9 kpc perpendicular to the disc. Most of the emission from the halo is at energies below 1 keV. The southeastern halo is softer than the northwestern halo. The halo emission is not uniform, neither spatially nor spectrally. To model the X-ray spectra in the halo, we needed two thermal plasmas with solar abundances plus galactic foreground absorption. Temperatures are around 0.1 and 0.3 keV. The total luminosity of the diffuse emission is 8.4×10^{38} erg s^{-1} and 2.1×10^{38} erg s^{-1} (0.2-1.5 keV) in the northwestern and southeastern halo, respectively. Electron densities computed to $3.2 \, \eta^{-0.5} \times 10^{-3}$ cm^{-3} and $4.7 \, \eta^{-0.5} \times 10^{-3}$ cm^{-3}, with the volume filling factor η. With solar abundances this implies total masses of $3.3 \, \eta^{-0.5} \times 10^{7}$ M$_\odot$ and $1.8 \, \eta^{-0.5} \times 10^{7}$ M$_\odot$ for the northwestern and southeastern halo, respectively.

A comparison between X-ray and UV emission showed that both originate from the same regions. The UV emission is more extended in the southeastern halo, where it seems to form a shell around the X-ray emission.

In Chapter 5, we have studied the nuclear outflow of the nearby starburst galaxy NGC 253 in X-rays with respect to its morphology and to spectral variations along the outflow. We analysed *XMM-Newton* RGS spectra, RGS brightness profiles in cross-dispersion direction, narrow-band RGS and EPIC images, and EPIC PN brightness profiles of the nuclear region and of the outflow from NGC 253. We detected a diversity of emission lines along the outflow. This includes lines from the He-like ions of Si, Mg, Ne, and O and their corresponding ions in the next higher ionisation state. Additionally transitions from Fe XVII and Fe XVIII are prominent. The derived temperatures from line ratios along the outflow range from 0.21 ± 0.01 to 0.79 ± 0.06 keV, and the ratio of Fe XVII lines indicates a predominantly collisionally ionised plasma. Additionally, we see indications of either a recombining or an underionised plasma in the Fe XVII line ratio. Derived electron densities are 0.106 ± 0.018 cm^{-3} for the nuclear region and 0.025 ± 0.003 cm^{-3} for the outflow region closest to the centre. The RGS image in the O VIII line energy clearly shows the morphology of an outflow extending out to $\sim$750 pc along the southeast minor axis, while the northwest part of the outflow is not seen in O VIII due to the heavy absorption by the galactic disc. This is the first time that the hot wind fluid has been detected directly. The limb brightening in

Chandra and *XMM-Newton* EPIC observations is only seen in the energy range that contains the Fe XVII lines (550–750 eV). In all other energy ranges between 400 and 2000 eV, no clear evidence of limb brightening could be detected.

6.2 Outlook

In this work, we investigated only one point source in NGC 253. The number of detected point sources in the disc of NGC 253 is approximately 200, as detected in the available *XMM-Newton* and *Chandra* data sets. Their luminosities range from $L_{\rm X} \lesssim 10^{36}$ erg s^{-1} to $L_{\rm X} \gtrsim 10^{39}$ erg s^{-1}. Most of these sources show some kind of variability, ranging from eclipsing over erratic to transient as in Galactic sources. A detailed analysis of this sample, which will also try to determine the nature of these sources, is ongoing (Trinchieri et al. in preparation).

In the analysis of the diffuse emission we found indication of non-equilibrium ionisation conditions, i.e. recombining or underionised plasmas. A currently ongoing analysis with a non-equilibrium model from Breitschwerdt & Schmutzler (1999), which also considers the ionisation history of the plasma, will hopefully provide us with a more comprehensive understanding of the composition, temperature and dynamical structure of the gas in the outflow and in the halo.

Up to now, it is still unclear how much mass, metals and energy is transported in superwinds, and how much of it is able to escape the potential wells of the galaxies to enrich the intergalactic medium. Also the metallicity of the gas in the disc and in the halo is not yet well constrained. To be able to resolve these questions, improved X-ray observatories are needed:

Large fields of view are required to cover a significant portion of the galaxy and at the same time provide a big enough region where the background can be extracted. A low background is essential to study low surface brightness emission in nearby galaxies, when the signal can easily be dominated by the particle background.

To constrain the metallicity of the gas in nearby galaxies, most important is a high sensitivity and a good energy resolution below 2 keV, which is needed to obtain data with good statistics. Especially in crowded fields like in galactic discs, also a small point spread function is required to separate diffuse emission from point sources.

To learn more about the mass, metal and energy content of superwinds, we need a high spectral resolution comparable to the RGS, combined with a drastically increased sensitivity. This will enable us to analyse the kinematics of the outflow, which is essential to derive the mass and energy transport properties.

Appendix A

The soft diffuse X-ray background - An analysis of two Suzaku observations

A.1 Introduction

Already in the first X-ray observations (Giacconi et al. 1962), there was evidence for the existence of a cosmic diffuse X-ray background. With better instruments, it became clear, that the X-ray background at energies above ∼1 keV is not diffuse, but a superposition of distant X-ray sources (e.g. Fabian & Barcons 1992; Barber et al. 1996; Hasinger et al. 2001). This isotropic component is called the cosmic X-ray background (CXB). However, at energies below ∼1 keV, the extragalactic X-ray background cannot explain the observed X-ray emission solely.

Later it was discovered that the sun is embedded in a cavity (Paresce 1984), which is filled with hot ($T \sim 10^6$ K) X-ray emitting gas (Snowden et al. 1990). This so called Local Hot Bubble (LHB) was supposedly formed when a supernova in the vicinity of the sun exploded several million years ago. Additionally to the emission from the LHB, we see X-rays from beyond it, which originate in the Galactic halo (Burrows & Mendenhall 1991; Snowden et al. 1991). Unlike the CXB, the soft X-ray background with photon energies below ∼1 keV varies substantially with direction (see Fig. 1.4).

The superposition of the above mentioned components plus contributions from solar wind charge exchange, additional foreground sources and other background components has made interpretation difficult. Good observations in many directions and at different times are needed to start sorting out the components. A major step to separate the different components was achieved by Kuntz & Snowden (2000), who used the *ROSAT* all-sky survey and H I data to divide the observed 1/4 keV flux into a LHB and a Galactic halo component. We here report on a preliminary analysis of two high-latitude Suzaku observations pointing

towards 'empty' regions on the X-ray sky (see Fig. A.1), where in one field presumably 70% of the emission originates in the Galactic halo (observation High Latitude A) and in the other field almost 80% is caused by the LHB (observation High Latitude B).

Suzaku, the latest Japanese X-ray observatory with its four CCD X-ray imaging spectrometers (XIS, three frontside and one backside illuminated detectors), is characterised by a low detector background and a good energy resolution in particular at low energies, which allows to isolate most major spectral lines in the energy range between 0.2 and 10 keV. It is therefore well suited to study the soft diffuse X-ray emission in the observed fields.

A.2   Observations

The two observations were processed using the Suzaku pipeline (version 0.7). We filtered for times where the cut-off-ridigity (COR) was greater than 4 GV, the Earth elevation angle (ELV) greater than 10 degree and the Day-earth elevation angle (DYE_ELV) greater than
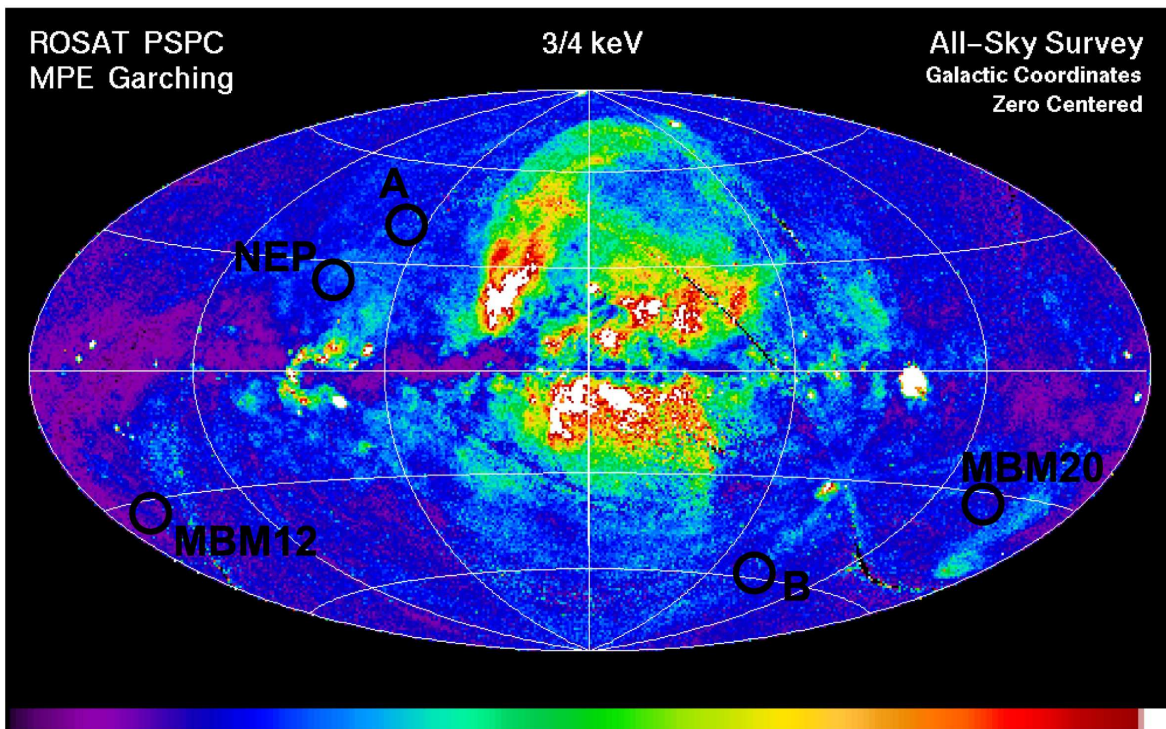
Figure A.1: The *ROSAT* 3/4 keV band data in Aitoff-Hammer projection, overplotted with the positions on the sky of different observations of the soft X-ray background. 'A' stands for High Latitude A, 'B' for High Latitude B, 'NEP' for the North Ecliptic Pole, and 'MBM12' and 'MBM20' for two high latitude molecular cloud observation pointings. Image from http://www.mpe.mpg.de/xray/wave/rosat/index.php.

Table A.1: Pointing positions and exposure times (T_{exp}) of the observations.

	High Latitude A	High Latitude B
RA/DEC(J2000)	$\alpha = 16^{\text{h}}24^{\text{m}}39\overset{\text{s}}{.}4, \delta = +43°28'19\overset{''}{.}2$	$\alpha = 02^{\text{h}}34^{\text{m}}57\overset{\text{s}}{.}8, \delta = -52°17'13\overset{''}{.}2$
Galactic coordinates	$l = 228.8, b = +63.5$	$l = 4.4, b = -61.4$
T_{exp}	74.9 ks	104 ks

20 degree, to remove times with very high non-X-ray particle background and to avoid any contamination from Earth's atmosphere, respectively. Response matrices and auxiliary response files were calculated using the XISSIM tools (ver. Oct 26th, 2006) with the newest calibration data (ver. Nov 2nd, 2006). Throughout the whole analysis we only used data from the backside illuminated XIS-1 detector because of its superior sensitivity at low energies. To remove the non-X-ray background from the spectra, we used the tools for the Suzaku Night Earth Database (ver. 0.0 20060530). The tool had some problems removing fluorescence lines from the detector between 1.3 and 2.3 keV. Therefore, we excluded this energy range from the spectral analysis. Both observations suffered gravely from Solar Wind Charge Exchange (SWCX) emission, which enhanced the X-ray flux especially in the oxygen and carbon lines. Therefore a careful selection of times where SWCX emission is at a minimum was necessary to derive proper values for the soft X-ray background. To screen for times with SWCX emission, we inspected light curves of the solar proton and ion flux. The solar wind data taken by several satellites is available from NASA's CDAWeb homepage (cdaweb.gsfc.nasa.gov/cdaweb/sp_phys/). Especially the ion flux from C^{+6} and O^{+7} can help to select good times, however SWCX emission is not only dependent on these values.

A.3 Oxygen line intensities

We derived oxygen line intensities for both observations during times with low and high SWCX contamination. Times for low or high SWCX contamination were chosen to match low or high proton and heavy ion flux in the solar wind, respectively. The time selection can probably be improved, since SWCX emission seems not only to be dependent on the flux level of the solar wind, but also on Earth's magnetic field configuration with respect to the line of sight of the observation (e.g. Quémerais et al. 2006). Also the position of earth against the Local Interstellar Medium flow pattern could play a role (e.g. Lallement et al. 1985). Further investigation of this issue is necessary, however the selection presented here is a good first order approximation. The spectra with low SWCX emission were fitted with a model for the cosmic X-ray background (absorbed power law) plus a vmekal model to represent the emission from the LHB and/or the Galactic disc and halo (Fig. A.3, *top*
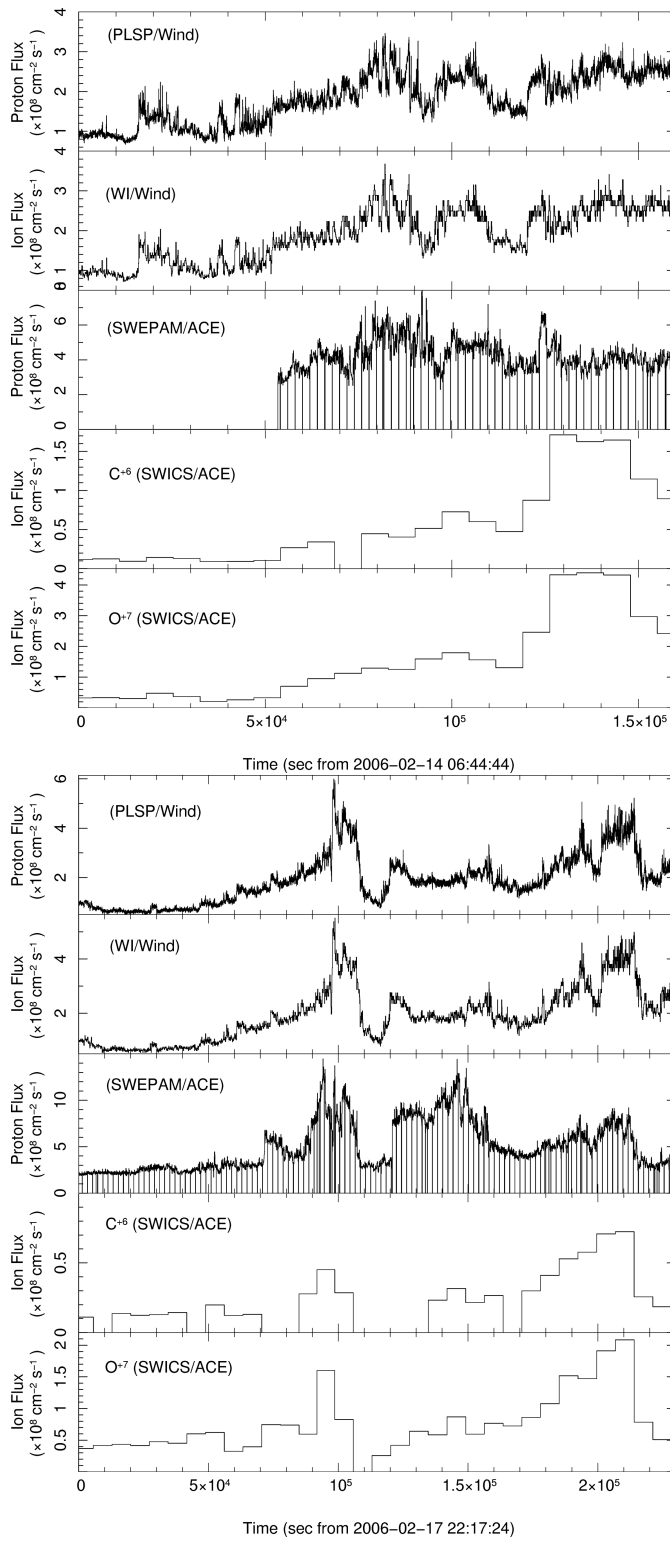
Figure A.2: Proton, Ion, C^{+6} and O^{+7} flux in the solar wind during observations High Lat. A *(top)* and High Lat. B *(bottom)*. Notice the rise in C^{+6} and O^{+7} at the end of the observations. This is expected to cause strong SWCX emission.

and Fig. A.4, *top*). The model parameters are shown in Tables A.2 and A.3. The LHB is thought to be near-equilibrium thermal emission at close to 10^6 K, so we only expect a small contribution to the oxygen lines from this component. As soon as the calibration below 0.3 keV is better established, we will also take a closer look at the 1/4 keV emission from the LHB. Oxygen line intensities were derived by setting the oxygen abundance to zero and fitting two gaussians at the oxygen line energies. The derived values are shown in Table A.4. The comparison of the O VII line intensity between observation High Lat. B and MBM12 (off-cloud) shows that the latter observation was probably affected by SWCX emission. The high column density in the direction of MBM12 should absorb most of the halo emission coming from that direction, so a minimum of oxygen emission is expected (as it is the case for the O VIII line). In general the O VIII line intensities might be correlated with the column density, with the exception of the North Ecliptic Pole (NEP) observation. This observation shows the largest line intensities compared to any other observation in the sample even though the column density in that direction is not the lowest. Since the NEP observation showed a clear increase in SWCX emission (Fujimoto et al. 2007), it cannot be excluded that the 'quiet' part of the observation is free from SWCX. As for the O VII line intensities in this sample the results are inconclusive. The values range between 2.49 and 7.37 LU (excluding the NEP observation; one light unit: 1 LU=1 ct cm^{-2} s^{-1} str^{-1}), but no correlation has been found yet. A further investigation including the 1/4 keV emission from the LHB hopefully will give further insight to solve this puzzle.

Table A.2: Best fit model for observation High Latitude A

Parameter	Value	
CXB (wabs $\times$ po):		
N_{H}	1.04×10^{20}	cm^{-2} (fixed)
Γ	1.4	(fixed)
Norm	$12.9^{+0.9}_{-0.9}$	ph cm^{-2} s^{-1} str^{-1}
vmekal:		
kT	$0.20^{+0.02}_{-0.02}$	keV
C Abundance	$4.94^{+3.57}_{-2.39}$	
N Abundance	$0.647^{+1.457}_{-0.647}$	
O Abundance	1.0	(fixed)
Ne Abundance	$0.694^{+1.266}_{-0.694}$	
Fe Abundance	$0.305^{+0.957}_{-0.305}$	
Norm	$13.1^{+2.2}_{-2.1}$	ph cm^{-2} s^{-1} str^{-1}
χ^2/dof	37.9/39	
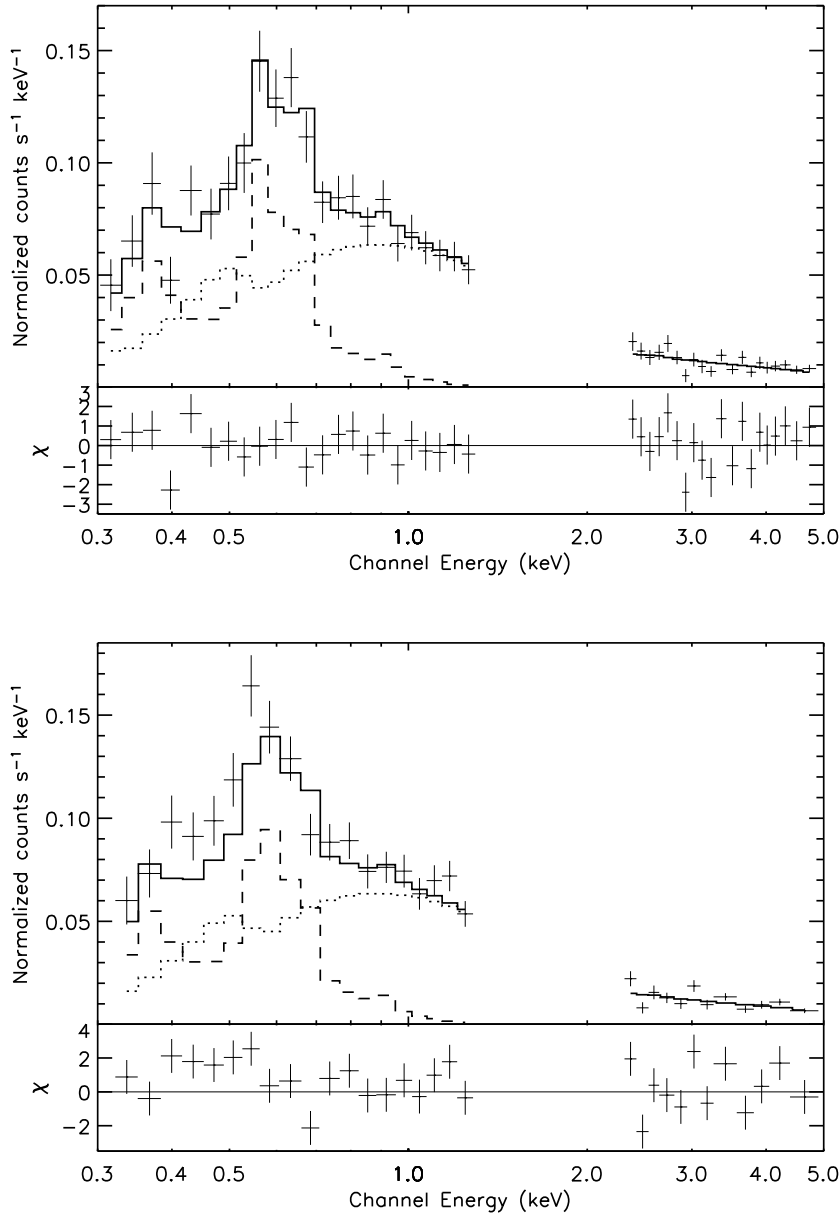
Figure A.3: (top): Spectrum of High Lat. A during the SWCX quiet period (first 50 ks) fitted with the CXB model plus a vmekal model. (bottom): Spectrum during a period with strong SWCX contamination (last 41 ks of the observation). To make it easier to compare this spectrum to the one during the SWCX quiet period we show the same model as in the top panel.
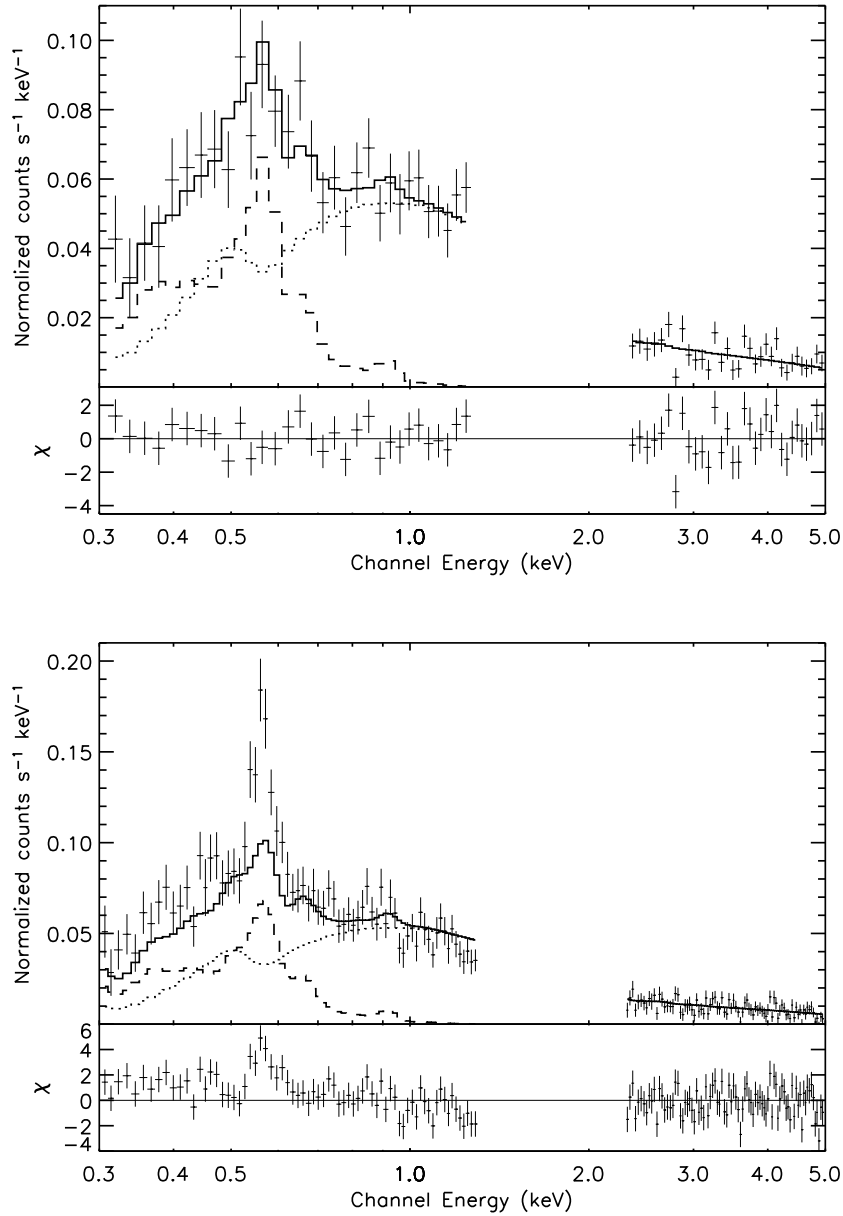
Figure A.4: (top): Spectrum of High Lat. B during the SWCX quiet period (first 70 ks) fitted with the CXB model plus a vmekal model. (bottom): Spectrum during a period with strong SWCX contamination (last 70 ks of the observation). To make it easier to compare this spectrum to the one during the SWCX quiet period we show the same model as in the top panel.

Table A.3: Best fit model for observation High Latitude B

Parameter	Value	
CXB (wabs $\times$ po):		
N_H	2.985×10^{20}	cm^{-2} (fixed)
Γ	1.4	(fixed)
Norm	$11.4^{+0.8}_{-0.9}$	ph cm^{-2} s^{-1} str^{-1}
vmekal:		
kT	$0.161^{+0.047}_{-0.024}$	keV
C Abundance	$2.72^{+5.82}_{-2.17}$	
N Abundance	$3.28^{+3.12}_{-1.69}$	
O Abundance	1.0	(fixed)
Ne Abundance	$1.66^{+3.94}_{-1.66}$	
Fe Abundance	$1.03^{+17.17}_{-1.03}$	
Norm	$8.31^{+3.65}_{-2.74}$	ph cm^{-2} s^{-1} str^{-1}
χ^2/dof	48.1/52	

Table A.4: Foreground absorption and line intensities (in units of ct cm^{-2} s^{-1} str^{-1}, or line units (LU), of O VII and O VIII in different observations of the soft X-ray background.

	NEP	MBM12[a]		MBM20[b]		High Lat. A	High Lat. B
		on-cloud	off-cloud	on-cloud	off-cloud		
N_H [10^{20} cm^{-2}]	4.4	40	8.7	16	0.86	1.0	3.0
O VII	$10.41^{+0.67}_{-0.62}$	3.34±0.26	5.68±0.42	3.59±0.56	7.37±0.34	$4.61^{+0.86}_{-0.93}$	$2.49^{+0.71}_{-0.66}$
O VIII	$3.69^{+0.54}_{-0.34}$	0.24±0.10	1.01±0.19	0.72±0.24	1.73±0.17	$2.15^{+0.65}_{-0.46}$	$1.09^{+0.39}_{-0.46}$

[a]Smith et al. (2007)
[b]Galeazzi et al. (2007)

A.4   Solar Wind Charge Exchange

Both observations were heavily contaminated by SWCX. Even after applying the criteria to remove times with SWCX emission, which we presented in Fujimoto et al. (2007), we cannot guarantee that our choice of times has removed all SWCX emission. A thorough investigation on the correlation of SWCX to solar activity, the orientation of the line of sight in the solar environment and other effects is currently ongoing.

In the following we want to further quantify the effects that SWCX emission had on the observations High Lat. A and B. The difference between times with high SWCX emission compared to times with low contamination are shown in Fig. A.3, (bottom) and Fig. A.4, (bottom). The SWCX component in High Lat. A could be fit with two lines at 0.421 keV

(N VI, $1.79^{+1.68}_{-1.11}$ LU), and 0.524 keV (O K from atmosphere, $1.61^{+0.49}_{-0.97}$ LU). O VIII even seems to be lower by about 0.14 LU in this spectrum compared to the SWCX quiet time. Observation High Lat. B was enhanced by emission lines at 0.304 keV (C V, $16.3^{+30.8}_{-16.3}$ LU), 0.368 keV (C VI, $3.99^{+2.16}_{-2.26}$ LU), 0.460 keV (C VI Ly-g, $1.97^{+0.80}_{-0.92}$ LU), 0.569 keV (O VII, $3.01^{+0.85}_{-0.89}$ LU) and 0.654 keV (O VIII, $0.35^{+0.48}_{-0.35}$ LU) during high ion flux times. The C VI Ly-g emission has been observed before with Suzaku in the NEP observation (Fujimoto et al. 2007) but also with XMM-Newton and Chandra (e.g. Snowden et al. 2004; Edgar et al. 2006). The spectrum of observation High Lat. B showed no especially strong oxygen lines in the quiet SWCX times, while in times with strong SWCX emission this changed significantly.

A.5 Conclusions

We presented the results of the analysis of two observations of the soft diffuse X-ray background. Both observations were heavily affected by SWCX, making the interpretation of the results difficult and ambiguous. Therefore, we are only able to give upper limit values for the oxygen line intensities in both regions. We compared oxygen line intensities to observations of other regions on the sky. In general the O VIII line intensities might be correlated with the foreground column density. As for the O VII line intensities in this sample the results are inconclusive. To quantify the contamination by SWCX, we derived emission line intensities of C V, C VI, C VI Ly-g, N VI, O K, O VII, and O VIII.

Appendix A. The soft diffuse X-ray background - An analysis of two Suzaku observations

Appendix B

Combined EPIC PN and MOS images

The *XMM-Newton* payload carries three X-ray imaging instruments. In order to add images from the different instruments, we developed a script that accounts for differences in exposure time and the sensitivity of the instruments. By combining images from all three instruments, we increase the statistics, are able to fill the detector gaps, so the resulting image has no holes. A version of this software is publicly available from the ESA webpages[1].

In the following we will describe the script, starting from the event files, that are produced by the standard data reduction software. First the event files are cleaned for bad pixels and hot columns that were not detected in the standard data reduction. A set of X/Y coordinates can be given to remove hot of flickering pixels. This can be done for the two MOS and the PN detector individually. Additionally for the EPIC PN, the user can provide the column coordinate on a specific CCD, and the energy threshold, below which all events are removed from the event files. This is used to suppress noise from columns that suffer from a high noise level at low energies. Also whole columns can be removed in the same manner as hot pixels. For the EPIC PN all of the above steps also have to be done for the out-of-time event file.

After the cleaning, good time interval filter is applied to reduce high background. The energy range between 7.2 and 9.2 keV is excluded in the EPIC PN event and out-of-time event files. In this band, the PN detector shows strong background fluorescent lines with varying strength over the field of view (Freyberg et al. 2004) that would be visible as structure in the image.

From the cleaned event files (MOS, PN, and the PN out-of-time event file), images are extracted in different energy bands. The standard setting produces images in the energy bands 0.2–0.5 keV, 0.5–1.0 keV, 1.0–2.0 keV, 2.0–4.5 keV, and 4.5–12.0 keV. For the lowest EPIC PN energy band only single events are used, i.e. events that are only detected in

---

[1]http://xmm.vilspa.esa.es/external/xmm_science/gallery/utils/images.shtml

one pixel. For the other EPIC PN energy bands we use single and double events. For the EPIC MOS single, double and triples are used (PATTERN $<$ 12, see *XMM-Newton* User Handbook).

These images are binned to a user-set pixel size. Also exposure maps are produced, which are used to correct for different exposures in the images and to create masks that only include regions with a user-defined minimum exposure time. The images, out-of-time images, and exposure maps are smoothed with a gaussian with a kernel width set by the user. The out-of-time images are scaled with the fraction of expected out-of-time events. For example in full frame mode, 6.3% of all events are out-of-time events, that are generated by X-ray sources during read-out of the CCDs along the corresponding column. The rescaled out-of-time images are subtracted from the images.

To create a combined image from EPIC PN and MOS where the detector gaps are unnoticable, the background level needs to be similar in the single images. Therefore before merging the PN and MOS images, the PN images are rescaled by a factor that is different in each energy band, adjusting the different background levels. This step however, makes the final images not usable to extract correct surface brightnesses. The resulting image is masked to a region with a user-set minimum exposure time.

An example image is shown in Fig. B.1, where we processed the longest exposure of NGC 253 (ObsID 0152020101).
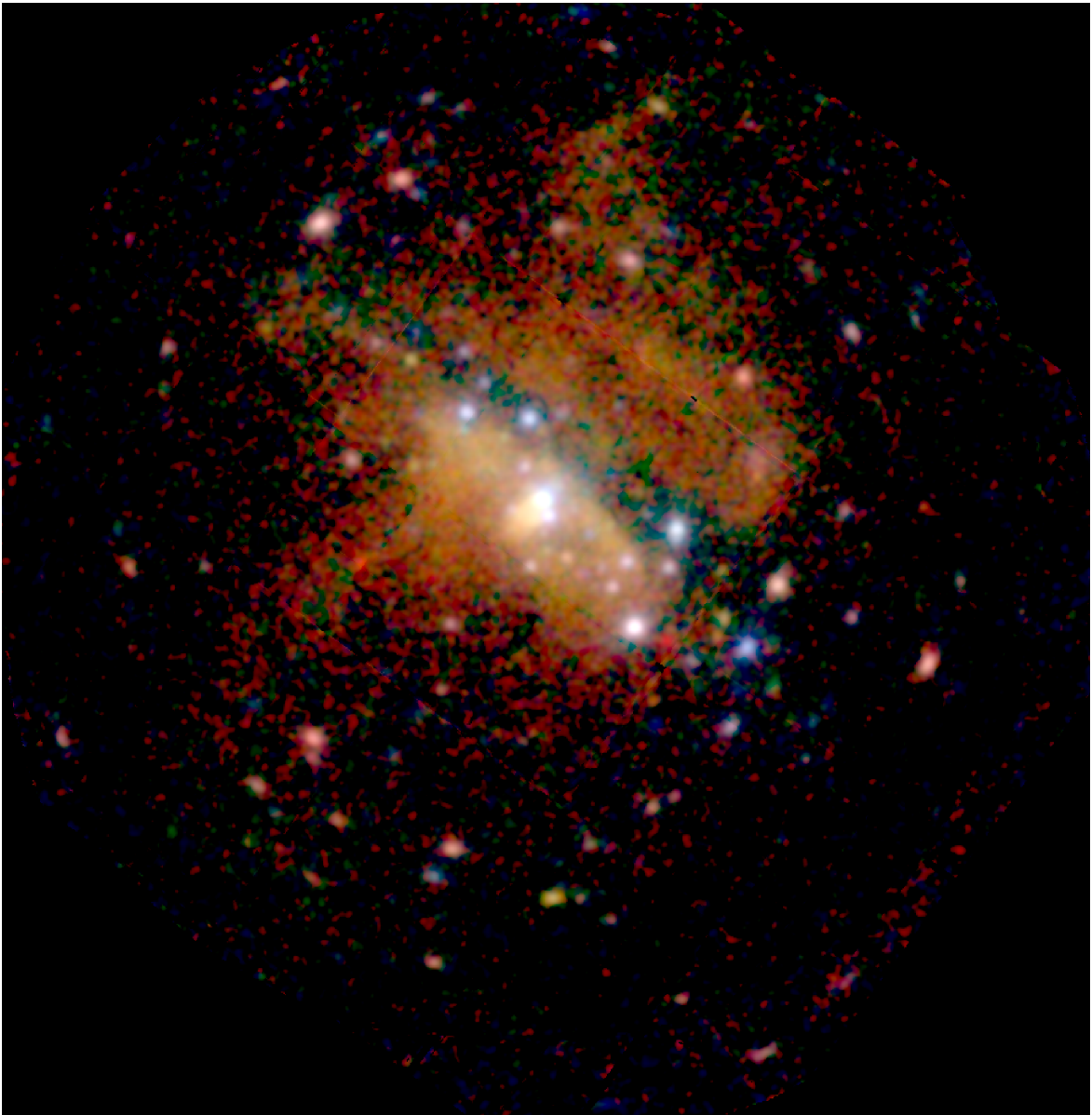
Figure B.1: An image of NGC 253 that was produced, using the script described in App.B. In this example the three lowest energy bands were combined into a false-colour X-ray image (red: 0.2–0.5 keV, green: 0.5–1.0 keV, blue: 1.0–2.0 keV) using `ds9`.

Appendix B. Combined EPIC PN and MOS images

Appendix C

Vignetting corrected and background subtracted EPIC PN images

We developed an algorithm to create vignetting corrected and adaptively smoothed EPIC PN images. In the following we will describe the algorithm step-by-step.

The basis for this procedure is a cleaned event file and an out-of-time event file. This cleaning included screening for high background and also removing bad pixels and bad columns (see Appendix B).

We here describe the creation of three images, which can be combined to a RGB colour image at the end of the procedure. In the following all steps have to be done for all three energy bands, unless stated otherwise.

An image is extracted from the event file in desired energy band, which is corrected for out-of-time events (see Appendix B). To allow vignetting correction, the detector background surface brightness (electronic noise, high energy particles) is subtracted from the image. This value is determined from the corners of the detector which are outside of the field of view of the telescope. It is assumed that the detector background is uniform across the whole detector (for energies between 7.2 and 9.2 keV this is not a good approximation, see Appendix B and Freyberg et al. 2004).

Before smoothing the image, a template with smoothing kernels has to be created. This template guarantees that images in different energy bands are smoothed with the same kernel size. For this purpose, the images in the different energy bands are added up, smoothed, and masked with the task `asmooth`, which creates the template with the smoothing kernel sizes.

This template is used to smooth the images in the different energy bands. This step includes the vignetting correction via the exposure map, and a masking of the image to a region with an acceptable minimum exposure time.

The resulting images of NGC 253 and a combined RGB colour image of the lowest three

energy bands (created with `ds9` is shown in Fig. 4.1, 4.2, and 4.3. The tool is publicly available and can be obtained from the MPE homepage[1].

---

[1]http://www.mpe.mpg.de/xray/wave/xmm/cookbook/EPIC_PN/

Appendix D

Background correction for faint extended emission

The conventional way to create a background spectrum is to select a region from the same observation where there is no emission from the source. Additionally, the region should be close to the source. This way, the spectral background should have the same characteristics as the background at the source region. In NGC 253, a region which suffices the first criterion can be found at the border of the field of view in the southwestern part of the detector. The second criterion, however, is not satisfied. The background region may show a different detector background, and additionally the vignetting is different.

Since we were interested in determining the characteristics of emission with low surface brightness, that extends over a large region, where the background is (probably) the dominant component, we needed a very accurate estimate of the background. Given the very soft nature of the emission, we cannot use blank sky observations that were taken in regions of the sky where the foreground N_{H} is different (not to mention other uncertainties due to different detector settings, particle radiation levels, etc.). Here we describe a method to use a local estimate of the sky background that takes properly into account vignetting and detector background issues.

Table D.1: Rejected CCD rows due to MIPs per time unit in the used observations.

Obs ID	Filter	rejected line counter value
0122320707	Closed	181.7
0125960101	Medium	190.2
0152020101	Thin	141.4
0160362801	Closed	120.4

Appendix D. Background correction for faint extended emission

$$
B(E) = \underbrace{S_{\mathrm{obs}}^{\mathrm{OOT}}(E)f}_{\mathrm{Out-of-Time\ events}} + \underbrace{S_{\mathrm{det}}(E)\frac{R_{\mathrm{obs}}}{R_{\mathrm{det}}}\frac{t_{\mathrm{obs}}}{t_{\mathrm{det}}}}_{\mathrm{detector\ background}} - \underbrace{S_{\mathrm{det}}^{\mathrm{OOT}}(E)\frac{R_{\mathrm{obs}}}{R_{\mathrm{det}}}\frac{t_{\mathrm{obs}}}{t_{\mathrm{det}}}f}_{\mathrm{detector\ Out-of-Time\ events}} +
$$

$$
+ \frac{V(E,\theta_S)}{V(E,\theta_B)}\frac{A_S}{A_B}\underbrace{\left(B_{\mathrm{obs}}(E) - \underbrace{B_{\mathrm{obs}}^{\mathrm{OOT}}(E)f}_{\mathrm{Out-of-Time\ events}} - \underbrace{B_{\mathrm{det}}(E)\frac{R_{\mathrm{obs}}}{R_{\mathrm{det}}}\frac{t_{\mathrm{obs}}}{t_{\mathrm{det}}}}_{\mathrm{detector\ background}} + \underbrace{B_{\mathrm{det}}^{\mathrm{OOT}}(E)\frac{R_{\mathrm{obs}}}{R_{\mathrm{det}}}\frac{t_{\mathrm{obs}}}{t_{\mathrm{det}}}f}_{\mathrm{detector\ Out-of-time\ events}} \right)}_{\mathrm{sky\ background}}
$$

$$\tag{D.1}$$

To remove the detector background, we used archival observations which were taken in the same mode as the NGC 253 observations, but where the filter wheel was closed. To avoid effects due to changes in the detector settings, or changes of the detector performance due to other reasons, we chose the closed observations to be as close as possible in time to the NGC 253 observations. The closed observations we used for observation 1 and 4 are: revolution 59, obs. id. 0122320701, exposure S003 (50.5 ks) and revolution 732, obs. id. 0160362801, exposure S005 (38.6 ks), respectively. To ensure, that there are as little as possible differences between the source observation and the closed observation, we removed bad columns and bad pixels both in the NGC 253 and closed observation. Additionally, the closed observations may have been taken when the spacecraft was exposed to a different particle radiation level than the one present during observations 1 or 4. The *XMM-Newton* house keeping file contains information on how many CCD rows per time unit were rejected due to a possible minimum ionising particle (MIP) event, which is a direct estimator of the average radiation level. We used these values (see Table D.1), to rescale the count rate of the closed observations.

We used Out-of-Time spectra from the source and background region to correct for contribution from Out-of-Time events. When one subtracts a closed observation spectrum from a Out-of-Time corrected spectrum, one actually removes the Out-of-Time spectrum of the detector background twice. This is corrected in our method by adding again the Out-of-Time spectra of the detector background.

We corrected the background region spectrum for Out-of-Time events and the detector background and applied the vignetting correction in each energy bin as a function of off-axis angle of the source and background spectrum. This gave us the sky background spectrum.

In all of the above steps, different exposure times and areas in the extraction regions have been accounted for. Since some of the components in the final background spectrum do have low number statistics, we used the conservative approximation to Poissonian errors $\sigma_N \approx 1 + \sqrt{0.75 + N}$ (Gehrels 1986). To avoid unjustified large errors, we roughly binned

the spectrum before calculating errors. The resulting background subtracted spectrum then has a significance in each bin of a least 3 σ. The errors were propagated properly and were included in the file with the final background spectrum. This spectrum can be used with XSPEC as a background spectrum.

The whole method can be summarised by Eq. D.1 with the following symbols:

- $B(E)$ is the counts at energy E in the background spectrum

- $B_{\mathrm{obs}}(E)$ is the counts in the NGC 253 observation

- $S_{\mathrm{det}}(E)$ is the counts from the detector background spectrum in the source region

- $B_{\mathrm{det}}(E)$ is the counts in the detector background spectrum in the background region

- $S_{\mathrm{obs}}^{\mathrm{OOT}}(E)$ are the counts in the Out-of-Time spectra in the source region

- $B_{\mathrm{obs}}^{\mathrm{OOT}}(E)$ are the counts in the Out-of-Time spectra in the background region

- $S_{\mathrm{det}}^{\mathrm{OOT}}(E)$ are the counts in the Out-of-Time detector background spectra in the source region

- $B_{\mathrm{det}}^{\mathrm{OOT}}(E)$ are the counts in the Out-of-Time detector background spectra in the background region

- t_{obs} is the exposure time in the NGC 253 observation

- t_{det} is the exposure time in the closed observation

- R_{obs} is the rejected line counter values (see Table D.1) in the NGC 253 observation

- R_{det} is the rejected line counter values (see Table D.1) in the closed observation

- A_S is the area in the source region

- A_B is the area in the background region

- $V(E, \theta_S)$ is the vignetting value in the source region, depending on the offset angle θ and the energy E

- $V(E, \theta_B)$ is the vignetting value in the background region, depending on the offset angle θ and the energy E

- f is the fraction of Out-of-Time events in the corresponding mode of the observation

A comparison between this new method and the conventional method, that does not use the vignetting correction nor the closed observations, is shown in Fig. D.1 for two example spectra, both in observations 1 and 4. The single background components in the source and background region in observation 4 are shown in Fig. D.2. All figures show counts integrated over the extraction region. The counts in the background region were rescaled to the source region area to be able to compare them to the source spectrum. Also, the counts in the closed observation were rescaled to the exposure time and radiation level in the source observation.

The differences between the new and the conventional method in terms of the resulting best fits are the following: In the majority of the tested cases, an additional power law component with $\Gamma \sim 0$ is required for the fit in the spectrum, obtained with the conventional method. The temperatures are consistent between both methods, but the resulting flux levels in the conventional method are higher. Differences in total flux values range between 2% and 22%. The effect between the two methods is highest in regions with low surface brightness. Here the background dominates and a correct treatment is crucial. As an example, the
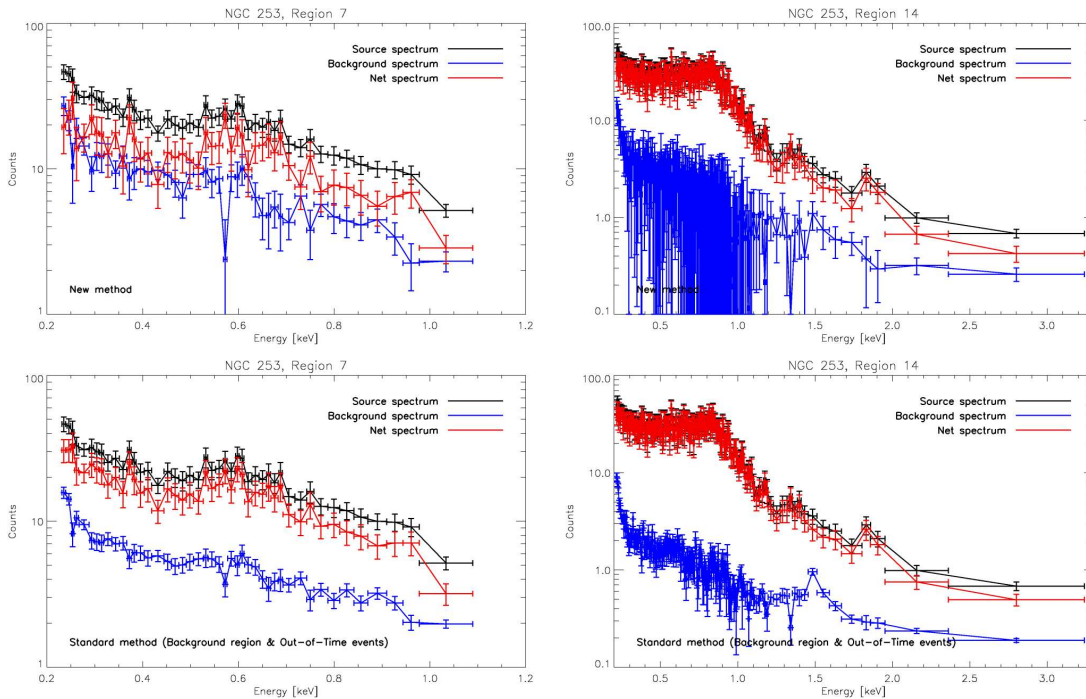
Figure D.1: Comparison between the background substraction on two examples (same source regions as in Fig 4.6). *(left):* the spectrum of region 7, *(right):* the spectrum of region 14. The top panel shows the new method, as described in this work, the bottom panel shows the conventional method, where the raw background spectrum is used, and a correction for Out-of-Time events has been applied. We only show the spectra of observation 4 here, since these have the better statistics.

difference in flux in region 7 (low surface brightness) is 15% and 22%, for observations 1 and 4, respectively. Whereas in region 14 (high surface brightness), the differences are 2% and 3%.

The tool is publicly available and can be obtained from the MPE homepage[1].

---

[1]http://www.mpe.mpg.de/xray/wave/xmm/cookbook/EPIC_PN/
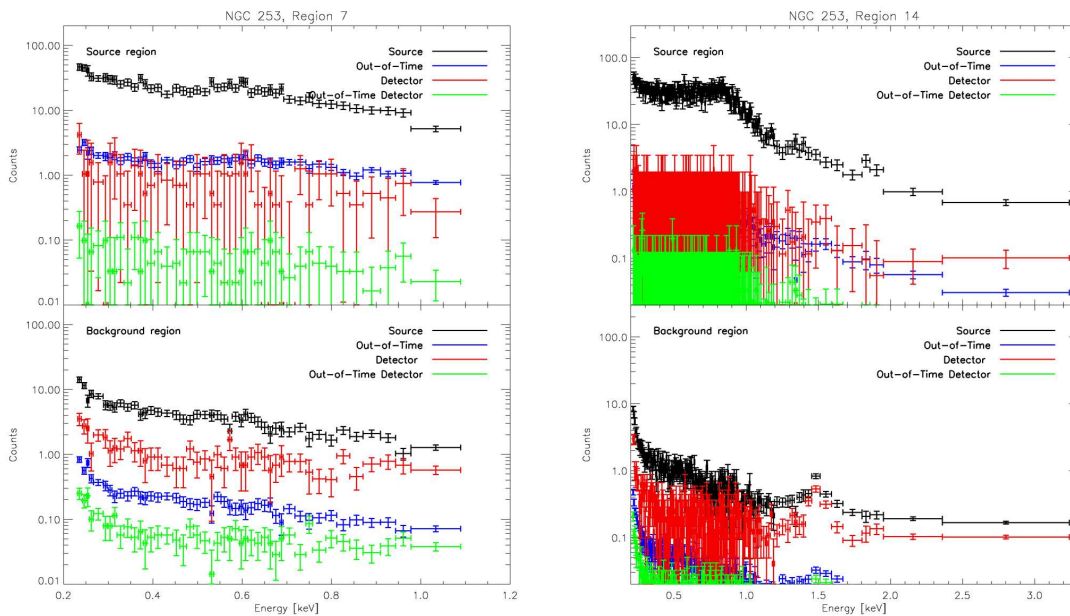
Figure D.2: The single components that are part of the total background spectrum compared to the source spectrum. *(left):* Region 7, *(right):* Region 14, *(top):* components from the source region, *(bottom):* components from the background region. The single components were corrected for areas, exposure time, and radiation level, with respect to the source spectrum in the source region, but no vignetting correction was applied yet.

Appendix D. Background correction for faint extended emission

Appendix E

RGS images of emission line regions

Images of an object in individual emission lines can be produced from XMM-Newton RGS data since the RGS is a slitless spectrometer and the entire field of view is imaged onto the detector CCDs. We here present a procedure to extract an image in a specific emission line.

Requirements for this procedure are:

- A sufficient number of counts ($\gtrsim 10^3$) in the emission line.

- An extent of the source of $\lesssim 2'$. For larger sources, neighbouring emission lines are likely to overlap, which leads to a contamination of the image by the neighbouring line.

  For emission lines that are close to each other, a combined image can be extracted. However, this reduces the possible spatial resolution. For example, an image in the Fe XVII lines (17.055 Å and 17.100 Å) has a maximum resolution of $\sim 20''$ (compared to $12''$ for one line). The separation of the lines is 0.045 Å, which corresponds to a shift on the detector in the dispersion direction of $19.9''$.

The basis for this procedure are the observation data files (ODF). Calling the SAS meta-task `rgsproc` with a RA-Dec reference coordinate on the sky, produces the event files, the exposure maps, and the spectra for both RGS detectors. The event files contain the positions of each detected photon in the dispersion versus cross-dispersion angle coordinate system and additionally the energy of the photon, which is measured with the intrinsic energy resolution of the CCD. The event files are filtered for the wavelength (dispersion angle) range of the desired line and for the "banana region" in wavelength-energy-space to exclude second-order spectra and noise (alternatively, a user-specified energy range can be used).

In order to reconstruct an image in a specific wavelength range from the RGS data, the mapping of the sky onto the detector has to be reversed. This transformation is described by
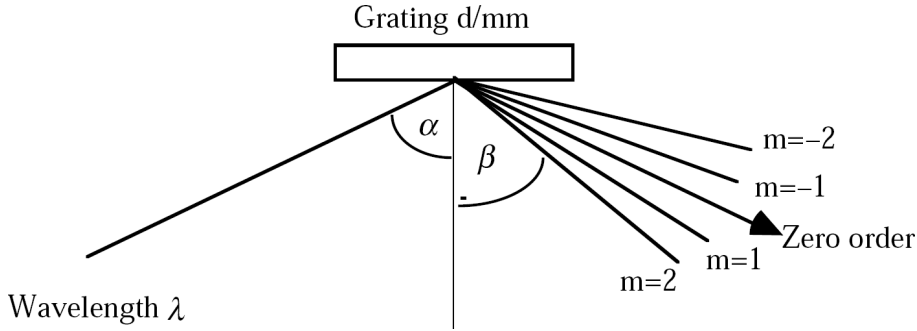
Figure E.1: Schematic drawing of the grating geometry.

the dispersion relation

$$\cos \beta = \frac{m\lambda}{d} + \cos \alpha. \tag{E.1}$$

α is the incident angle, β the exit angle, λ the wavelength, m the interference order, and d the grating line density (also see Fig. E.1). Deviations from the incident angle $\Delta\beta$ due to an offset $\Delta\phi$ of the source on the sky parallel to the dispersion direction can be written as

$$\Delta\beta = \frac{\sin \alpha}{\sin \beta} \Delta\phi \frac{F}{L}. \tag{E.2}$$

(also see the description of the SAS task rgsangles[1]). $F = 7500$ mm is the focal length of the telescope, and $L = 6700$ mm is the distance between the Reflection Grating Array and the prime focus.

By inverting equation E.2 for $\Delta\phi$, the relative coordinate of a detected photon in dispersion direction on the sky is reconstructed. An additional Doppler shift due to the object's systemic velocity needs to be accounted for separately. The effects of the velocities of the earth with respect to the sun and *XMM-Newton*'s orbital velocity can be neglected since they translate only to shifts of the order of $0.7''$ and $4'' \times 10^{-4}$ at ~ 19 Å, respectively, and therefore are much smaller than the width of the point spread function. Together with the cross-dispersion angle, the RA-Dec position of each event is derived. From the sky positions of the events, images are constructed, which are corrected for exposure, binned and smoothed with a Gaussian filter.

Images in the Ne X, Fe XVII and O VIII lines are shown in Fig. 5.5. The number of photons that were extracted from all three NGC 253 observations are 806, 1077, 816, and 1231 for the images in the Ne X (11.98–12.35 Å), Fe XVII at 15 Å (14.86–15.13 Å), Fe XVII at 17 Å (16.90–17.21 Å), and O VIII (18.80–19.17 Å) lines, respectively. The FWHM of the Gaussian filter was $12''$ for Ne X, Fe XVII at 15 Å, O VIII, and $20''$ for Fe XVII at 17 Å.

---

[1]http://xmm.vilspa.esa.es/sas/current/doc/rgsangles/node3.html

The tool is publicly available and can be obtained from the MPE homepage[2].

---

[2]http://www.mpe.mpg.de/xray/wave/xmm/cookbook/general/rgs.php

List of Figures

List of Tables

List of Tables

List of Abbreviations

AGN	Active Galactic Nucleus
CCD	Charge Coupled Device
CTI	Charge Transfer Inefficiency
CXB	Cosmic X-ray Background
CV	Cataclysmic Variable
EPIC	European Photon Imaging Camera
ESA	European Space Agency
FOV	Field Of View
FWHM	Full Width Half Maximum
HMXB	High Mass X-ray binary
HRI	High Resolution Imager
HST	Hubble Space Telescope
LHB	Local Hot Bubble
LMXB	Low Mass X-ray Binary
MOS	Metal Oxide Semi-conductor
NEP	North Ecliptic Pole
NGC	New General Catalogue
ODF	Observation Data Files
PSF	Point Spread Function
PSPC	Position Sensitive Proportional Counter
RGS	Reflection Grating Spectrometer
ROSAT	Roentgen Satellit
S/N	Signal-to-Noise ratio
SAS	Science Analysis System
SNR	Supernova Remnant
SWCX	Solar Wind Charge Exchange
ULX	Ultra Luminous X-ray source
USNO	United States Naval Observatory
WFPC2	Wide Field Planetary Camera 2

124

WIYN Telescope	Wisconsin Indiana Yale and NAOA Telescope
XIS	X-ray Imaging Spectrometer
XMM	X-ray Multi-Mirror

Bibliography

Antonucci, R. 1993, ARA&A, 31, 473

Barber, C. R., Roberts, T. P., & Warwick, R. S. 1996, MNRAS, 282, 157

Bauer, M. & Pietsch, W. 2005, A&A, 442, 925

Bauer, M., Pietsch, W., Trinchieri, G., et al. 2007a, astro-ph/0711.3182

Bauer, M., Pietsch, W., Trinchieri, G., et al. 2007b, A&A, 467, 979

Begelman, M. C. 2002, ApJ, 568, L97

Behar, E., Rasmussen, A. P., Griffiths, R. G., et al. 2001, A&A, 365, L242

Bell, E. F. & de Jong, R. S. 2001, ApJ, 550, 212

Bell, E. F., McIntosh, D. H., Katz, N., & Weinberg, M. D. 2003, ApJS, 149, 289

Blackburn, J. K. 1995, in Astronomical Society of the Pacific Conference Series, Vol. 77, Astronomical Data Analysis Software and Systems IV, ed. R. A. Shaw, H. E. Payne, & J. J. E. Hayes, 367

Bodewits, D., Christian, D. J., Torney, M., et al. 2007, A&A, 469, 1183

Brandt, W. N. & Hasinger, G. 2005, ARA&A, 43, 827

Bregman, J. N. 1980, ApJ, 236, 577

Breitschwerdt, D. & Schmutzler, T. 1999, A&A, 347, 650

Burrows, D. N. & Mendenhall, J. A. 1991, Nature, 351, 629

Cappi, M., Persic, M., Bassani, L., et al. 1999, A&A, 350, 777

Carilli, C. L., Holdaway, M. A., Ho, P. T. P., & de Pree, C. G. 1992, ApJ, 399, L59

Bibliography

Chevalier, R. A. & Clegg, A. W. 1985, Nature, 317, 44

Colina, L. & Perez-Olea, D. 1992, MNRAS, 259, 709

Comerón, F., Gómez, A. E., & Torra, J. 2003, A&A, 400, 137

Cox, D. P. 1998, in Lecture Notes in Physics, Berlin Springer Verlag, Vol. 506, IAU Colloq. 166: The Local Bubble and Beyond, ed. D. Breitschwerdt, M. J. Freyberg, & J. Truemper, 121–131

Cravens, T. E. 1997, Geophys. Res. Lett., 24, 105

Cravens, T. E. 2000, ApJ, 532, L153

Cravens, T. E. 2002, Science, 296, 1042

Dahlem, M., Parmar, A., Oosterbroek, T., et al. 2000, ApJ, 538, 555

Dahlem, M., Weaver, K. A., & Heckman, T. M. 1998, ApJS, 118, 401

de Avillez, M. A. & Breitschwerdt, D. 2004, A&A, 425, 899

de Avillez, M. A. & Breitschwerdt, D. 2005, A&A, 436, 585

de Vaucouleurs, G., de Vaucouleurs, A., Corwin, Jr., H. G., et al. 1991, Third Reference Catalogue of Bright Galaxies (Volume 1-3, XII, 2069 pp. 7 figs. Springer-Verlag Berlin Heidelberg New York)

Demoulin, M. H. & Burbidge, E. M. 1970, ApJ, 159, 799

den Herder, J. W., Brinkman, A. C., Kahn, S. M., et al. 2001, A&A, 365, L7

Dennerl, K., Englhauser, J., & Trümper, J. 1997, Science, 277, 1625

Dickey, J. M. & Lockman, F. J. 1990, ARA&A, 28, 215

Doron, R. & Behar, E. 2002, ApJ, 574, 518

Draine, B. T. & Salpeter, E. E. 1979, ApJ, 231, 77

Dursi, L. J. & Timmes, F. X. 2006, ApJ, 641, 1071

Edgar, R. J., Wargelin, B. J., Raymond, J. C., et al. 2006, in Bulletin of the American Astronomical Society, Vol. 38, Bulletin of the American Astronomical Society, 330

Ehle, M., Breitfellner, M., Díaz Trigo, M., et al. 2007, XMM-Newton Users' Handbook, Issue 2.5

Engelbracht, C. W., Rieke, M. J., Rieke, G. H., Kelly, D. M., & Achtermann, J. M. 1998, ApJ, 505, 639

Fabbiano, G. 1988, ApJ, 330, 672

Fabbiano, G. 2006, ARA&A, 44, 323

Fabbiano, G. & Trinchieri, G. 1984, ApJ, 286, 491

Fabbiano, G., Zezas, A., & Murray, S. S. 2001, ApJ, 554, 1035

Fabian, A. C. & Barcons, X. 1992, ARA&A, 30, 429

Feldmeier, A., Puls, J., & Pauldrach, A. W. A. 1997, A&A, 322, 878

Fleming, T. A., Gioia, I. M., & Maccacaro, T. 1989, ApJ, 340, 1011

Forbes, D. A., Polehampton, E., Stevens, I. R., Brodie, J. P., & Ward, M. J. 2000, MNRAS, 312, 689

Freeman, P. E., Kashyap, V., Rosner, R., & Lamb, D. Q. 2002, ApJS, 138, 185

Freyberg, M. J., Briel, U. G., Dennerl, K., et al. 2004, in X-Ray and Gamma-Ray Instrumentation for Astronomy XIII. Edited by Flanagan, Kathryn A.; Siegmund,Oswald H. W. Proceedings of the SPIE, Volume 5165., ed. K. A. Flanagan & O. H. W. Siegmund, 112–122

Fujimoto, R., Mitsuda, K., Mccammon, D., et al. 2007, PASJ, 59, 133

Galeazzi, M., Gupta, A., Covey, K., & Ursino, E. 2007, ApJ, 658, 1081

Gao, Y., Wang, Q. D., Appleton, P. N., & Lucas, R. A. 2003, ApJ, 596, L171

Gehrels, N. 1986, ApJ, 303, 336

Giacconi, R., Gursky, H., Paolini, F. R., & Rossi, B. B. 1962, Physical Review Letters, 9, 439

Greiner, J. 2000, New Astronomy, 5, 137

Grimm, H.-J., Gilfanov, M., & Sunyaev, R. 2003, MNRAS, 339, 793

Haisch, B., Strong, K. T., & Rodono, M. 1991, ARA&A, 29, 275

Harnden, Jr., F. R., Golub, L., Rosner, R., et al. 1979, in Bulletin of the American Astronomical Society, Vol. 11, Bulletin of the American Astronomical Society, 775

Hasinger, G., Altieri, B., Arnaud, M., et al. 2001, A&A, 365, L45

Heckman, T. M., Armus, L., & Miley, G. K. 1990, ApJS, 74, 833

Heckman, T. M., Lehnert, M. D., Strickland, D. K., & Armus, L. 2000, ApJS, 129, 493

Hoopes, C. G., Heckman, T. M., Strickland, D. K., et al. 2005, ApJ, 619, L99

Immler, S. & Lewin, W. H. G. 2003, in Lecture Notes in Physics, Berlin Springer Verlag, Vol. 598, Supernovae and Gamma-Ray Bursters, ed. K. Weiler, 91–111

Itoh, H., Hayakawa, S., Masai, K., & Nomoto, K. 1987a, PASJ, 39, 529

Itoh, M., Kumagai, S., Shigeyama, T., Nomoto, K., & Nishimura, J. 1987b, Nature, 330, 233

Jansen, F., Lumb, D., Altieri, B., et al. 2001, A&A, 365, L1

Jarrett, T. H., Chester, T., Cutri, R., Schneider, S. E., & Huchra, J. P. 2003, AJ, 125, 525

Joye, W. A. & Mandel, E. 2003, in Astronomical Society of the Pacific Conference Series, Vol. 295, Astronomical Data Analysis Software and Systems XII, ed. H. E. Payne, R. I. Jedrzejewski, & R. N. Hook, 489

King, A. J. & Rowan-Robinson, M. 2004, MNRAS, 349, 1353

King, A. R. 2004, MNRAS, 347, L18

King, A. R., Davies, M. B., Ward, M. J., Fabbiano, G., & Elvis, M. 2001, ApJ, 552, L109

Kitaura, F. S., Janka, H.-T., & Hillebrandt, W. 2006, A&A, 450, 345

Kong, A. K. H., Rupen, M. P., Sjouwerman, L. O., & Di Stefano, R. 2005, astro-ph/0503465

Koribalski, B., Whiteoak, J. B., & Houghton, S. 1995, Publications of the Astronomical Society of Australia, 12, 20

Koribalski, B. S., Staveley-Smith, L., Kilborn, V. A., et al. 2004, AJ, 128, 16

Kosenko, D. I. 2006, MNRAS, 369, 1407

Kuntz, K. D., Gruendl, R. A., Chu, Y.-H., et al. 2005, ApJ, 620, L31

Kuntz, K. D. & Snowden, S. L. 2000, ApJ, 543, 195

Lallement, R., Bertaux, J. L., & Dalaudier, F. 1985, A&A, 150, 21

Lisse, C. M., Dennerl, K., Englhauser, J., et al. 1996, Science, 274, 205

Liu, J. & Bregman, J. N. 2005, ApJS, 157, 59

Liu, J.-F., Bregman, J. N., & Seitzer, P. 2004, ApJ, 602, 249

Liu, Q. Z., van Paradijs, J., & van den Heuvel, E. P. J. 2000, A&AS, 147, 25

Maccacaro, T., Gioia, I. M., Wolter, A., Zamorani, G., & Stocke, J. T. 1988, ApJ, 326, 680

Makishima, K., Kubota, A., Mizuno, T., et al. 2000, ApJ, 535, 632

Mauersberger, R., Henkel, C., & Chin, Y.-N. 1995, A&A, 294, 23

Mewe, R., Gronenschild, E. H. B. M., & van den Oord, G. H. J. 1985, A&AS, 62, 197

Miller, J. M., Fabian, A. C., & Miller, M. C. 2004a, ApJ, 614, L117

Miller, J. M., Zezas, A., Fabbiano, G., & Schweizer, F. 2004b, ApJ, 609, 728

Mohan, N. R., Anantharamaiah, K. R., & Goss, W. M. 2002, ApJ, 574, 701

Monet, D. G., Levine, S. E., Canzian, B., et al. 2003, AJ, 125, 984

Mushotzky, R. F. 1984, Advances in Space Research, 3, 157

Mushotzky, R. F., Cowie, L. L., Barger, A. J., & Arnaud, K. A. 2000, Nature, 404, 459

Osterbrock, D. E. 1998, in Revista Mexicana de Astronomia y Astrofisica, vol. 27, Vol. 7, Revista Mexicana de Astronomia y Astrofisica Conference Series, ed. R. J. Dufour & S. Torres-Peimbert, 180

Paresce, F. 1984, AJ, 89, 1022

Pence, W. D. 1980, ApJ, 239, 54

Pence, W. D. 1981, ApJ, 247, 473

Phillips, K. J. H., Mewe, R., Harra-Murnion, L. K., et al. 1999, A&AS, 138, 381

Pietsch, W. 1992, in Physics of Nearby Galaxies: Nature or Nurture?, ed. T. X. Thuan, C. Balkowski, & J. Tran Thanh van, 67

Pietsch, W., Fliri, J., Freyberg, M. J., et al. 2005, A&A, 442, 879

Pietsch, W., Fliri, J., Freyberg, M. J., et al. 2006, A&A, 454, 773

Pietsch, W., Roberts, T. P., Sako, M., et al. 2001, A&A, 365, L174

Pietsch, W., Vogler, A., Klein, U., & Zinnecker, H. 2000, A&A, 360, 24

Porquet, D., Mewe, R., Dubau, J., Raassen, A. J. J., & Kaastra, J. S. 2001, A&A, 376, 1113

Ptak, A., Serlemitsos, P., Yaqoob, T., Mushotzky, R., & Tsuru, T. 1997, AJ, 113, 1286

Puche, D., Carignan, C., & van Gorkom, J. H. 1991, AJ, 101, 456

Quémerais, E., Lallement, R., Ferron, S., et al. 2006, Journal of Geophysical Research (Space Physics), 111, 9114

Read, A. M., Ponman, T. J., & Strickland, D. K. 1997, MNRAS, 286, 626

Read, A. M. & Stevens, I. R. 2002, MNRAS, 335, L36

Revnivtsev, M., Churazov, E., Sazonov, S., Forman, W., & Jones, C. 2007, A&A, 473, 783

Revnivtsev, M., Sazonov, S., Gilfanov, M., Churazov, E., & Sunyaev, R. 2006, A&A, 452, 169

Reynolds, C. S., Loan, A. J., Fabian, A. C., et al. 1997, MNRAS, 286, 349

Rieke, G. H., Lebofsky, M. J., & Walker, C. E. 1988, ApJ, 325, 679

Roberts, T. P., Goad, M. R., Ward, M. J., et al. 2001, MNRAS, 325, L7

Roberts, T. P., Warwick, R. S., Ward, M. J., & Murray, S. S. 2002, MNRAS, 337, 677

Rosen, A. & Bregman, J. N. 1995, ApJ, 440, 634

Rugge, H. R. & McKenzie, D. L. 1985, ApJ, 297, 338

Sazonov, S., Revnivtsev, M., Gilfanov, M., Churazov, E., & Sunyaev, R. 2006, A&A, 450, 117

Schlegel, D. J., Finkbeiner, D. P., & Davis, M. 1998, ApJ, 500, 525

Schmitt, J. H. M. M. 2000, in Reviews in Modern Astronomy, Vol. 13, Reviews in Modern Astronomy, ed. R. E. Schielicke, 115

Schmitt, J. H. M. M., Snowden, S. L., Aschenbach, B., et al. 1991, Nature, 349, 583

Shapiro, P. R. & Field, G. B. 1976, ApJ, 205, 762

Shtykovskiy, P. & Gilfanov, M. 2005, MNRAS, 362, 879

Smith, R. K., Bautz, M. W., Edgar, R. J., et al. 2007, PASJ, 59, 141

Smith, R. K., Brickhouse, N. S., Liedahl, D. A., & Raymond, J. C. 2001, ApJ, 556, L91

Snowden, S. L., Collier, M. R., & Kuntz, K. D. 2004, ApJ, 610, 1182

Snowden, S. L., Cox, D. P., McCammon, D., & Sanders, W. T. 1990, ApJ, 354, 211

Snowden, S. L., Egger, R., Freyberg, M. J., et al. 1997, ApJ, 485, 125

Snowden, S. L., McCammon, D., Burrows, D. N., & Mendenhall, J. A. 1994, ApJ, 424, 714

Snowden, S. L., Mebold, U., Hirth, W., Herbstmeier, U., & Schmitt, J. H. M. 1991, Science, 252, 1529

Sofue, Y., Wakamatsu, K.-I., & Malin, D. F. 1994, AJ, 108, 2102

Stelzer, B. & Burwitz, V. 2003, A&A, 402, 719

Stevens, I. R., Read, A. M., & Bravo-Guerrero, J. 2003, MNRAS, 343, L47

Strickland, D. K., Heckman, T. M., Colbert, E. J. M., Hoopes, C. G., & Weaver, K. A. 2004a, ApJS, 151, 193

Strickland, D. K., Heckman, T. M., Colbert, E. J. M., Hoopes, C. G., & Weaver, K. A. 2004b, ApJ, 606, 829

Strickland, D. K., Heckman, T. M., Weaver, K. A., & Dahlem, M. 2000, AJ, 120, 2965

Strickland, D. K., Heckman, T. M., Weaver, K. A., Hoopes, C. G., & Dahlem, M. 2002, ApJ, 568, 689

Strickland, D. K. & Stevens, I. R. 2000, MNRAS, 314, 511

Strüder, L., Briel, U., Dennerl, K., et al. 2001, A&A, 365, L18

Sunyaev, R., Kaniovsky, A., Efremov, V., et al. 1987, Nature, 330, 227

Sunyaev, R. A. & Truemper, J. 1979, Nature, 279, 506

Tanaka, T., Sugiho, M., Kubota, A., Makishima, K., & Takahashi, T. 2005, PASJ, 57, 507

Trinchieri, G., Pietsch, W., & Bauer, M. in preparation

Tully, R. B. 1988, Nearby galaxies catalog (Cambridge and New York, Cambridge University Press, 1988, 221 p.)

Turner, J. L. & Ho, P. T. P. 1985, ApJ, 299, L77

Turner, M. J. L., Abbey, A., Arnaud, M., et al. 2001, A&A, 365, L27

Ulrich, M.-H. 1978, ApJ, 219, 424

van den Heuvel, E. P. J., Bhattacharya, D., Nomoto, K., & Rappaport, S. A. 1992, A&A, 262, 97

van der Heyden, K. J., Bleeker, J. A. M., Kaastra, J. S., & Vink, J. 2003, A&A, 406, 141

Veilleux, S., Cecil, G., Bland-Hawthorn, J., et al. 1994, ApJ, 433, 48

Vogler, A. & Pietsch, W. 1999, A&A, 342, 101

Wargelin, B. J., Markevitch, M., Juda, M., et al. 2004, ApJ, 607, 596

Weaver, K. A., Heckman, T. M., & Dahlem, M. 2000, ApJ, 534, 684

Weaver, K. A., Heckman, T. M., Strickland, D. K., & Dahlem, M. 2002, ApJ, 576, L19

Weaver, R., McCray, R., Castor, J., Shapiro, P., & Moore, R. 1977, ApJ, 218, 377

White, N. E., Stella, L., & Parmar, A. N. 1988, ApJ, 324, 363

Wilms, J., Allen, A., & McCray, R. 2000, ApJ, 542, 914

Zacharias, N., Urban, S. E., Zacharias, M. I., et al. 2004, AJ, 127, 3043

Zimmermann, H.-U. & Aschenbach, B. 2003, A&A, 406, 969

Acknowledgements

Acknowledgements